X-ray Study on Supernova Remnants Interacting with Dense Clouds

Hiromichi Okon

Department of Physics, Graduate School of Science, Kyoto University
Kitashirakawa Oiwake-cho, Sakyo, Kyoto, Kyoto, 606-8502, Japan
okon@cr.scphys.kyoto-u.ac.jp

January 2021

Abstract

A supernova remnant (SNR) is the astrophysical object resulting from an explosion of a star, and acts as the major energy source in the Universe. We study X-rays from SNRs interacting with dense clouds, which are unrivaled targets to investigate injection process of energy released in the explosions into the interstellar space. We perform spatial resolved spectroscopy of thermal X-rays from SNRs, W44 and IC 443, with *XMM-Newton*, and construct a model to predict X-ray line emission from dense clouds bombarded by sub-relativistic particles accelerated in SNRs.

Previous observations of SNRs interacting with clouds, including W44 and IC 443, unveiled the presence of peculiar plasmas in "recombination dominant phase", so-called over-ionized recombining plasmas (RPs). Such plasma is not anticipated in the standard picture of SNR evolution. Although the physical process of the over-ionization has not yet been fully understood, a key seems to be an efficient dissipation of internal energy of SNR plasma into interacting clouds. We compare spatial variations of plasma parameters of RPs in W44 and IC 443 with distributions of clouds hit by their blast wave. We find that combination of lower electron temperature and shorter recombination timescale is achieved in the region interacting with dense clouds. Moreover, a clear anticorrelation between the electron temperature and the recombination timescale is found. The results are well explained if the plasma was overionized by rapid cooling of electrons through thermal conduction with the dense clouds hit by the blast waves of the SNRs. Given that a few other overionized SNRs show evidence for adiabatic expansion as the major driver of the rapid cooling, our new result indicates that both processes can contribute to overionization in SNRs, with the dominant channel depending on the evolutionary stage.

Our recent X-ray studies revealed the presence of the neutral Fe Kα line emission from dense gas in the vicinity of some SNRs, which can be best interpreted as K-shell ionization of Fe atoms in the gas by sub-relativistic particles accelerated in the SNRs. The results indicate that the Fe Kα line is a new diagnostic tool to probe sub-relativistic particles at acceleration sites, which were almost unexplored until recently. Information on such particles is key to estimating total energy transferred into accelerated particles in SNRs and to considering the injection mechanism of thermal particles into the acceleration process. We construct a model for the Fe Kα line structures by various projectile ions utilizing atomic-collision data. When energetic heavy ions collide with target atoms, their strong Coulomb field can easily cause simultaneous ejection of multiple electrons of the target. This results in shifts in characteristic X-ray line energies, forming distinctive spectral structures. Detection of such structures in the neutral Fe Kα line strongly supports the particle ionization scenario, and furthermore provides direct evidence of heavy ions in the accelerated particles. An $\sim$ eV energy resolution by X-ray micro-calorimeters onboard future X-ray satellites will be able to resolve the structures.

Contents

List of Figures

List of Tables

Chapter 1

Introduction

A supernova remnant (SNR) is the astrophysical object resulting from an explosion of a star, i.e., supernova. SNRs inject a large amount of kinetic energy released in supernovae into the interstellar space via shock waves formed by collision between ejected materials (ejecta) and the interstellar medium (ISM). The major forms of the released energy are fluxes of thermal particles that constitute shock heated plasma ($\sim 10^7$ K) emitting thermal X-rays and of nonthermal particles accelerated at shocks in SNRs which are indeed believed to constitute a significant fraction of galactic cosmic rays. These particles supply energy required to trigger star formation, and furthermore spread throughout the galaxy cluster by a galactic superwind, resulting in the galaxy formation. Therefore, SNRs play an important role as the major energy sources in the Universe.

SNRs interacting dense clouds have been attracting attention in terms of energy conversion and dissipation processes in both aforementioned thermal and nonthernal aspects because recent multi-band observations enabled us to investigate detailed properties of both the energized particles in SNRs and their ambient gas. One of the topics that we cover is SNR plasmas in "recombination dominant phase", so-called over-ionized recombining plasmas (RPs). The presence of such plasma, revealed by recent X-rays studies (Yamaguchi et al., 2009; Ozawa et al., 2009), is not anticipated in the standard picture of SNR evolution. The physical process of the over-ionization has not yet been fully understood, but, as pointed out by some authors such as Itoh & Masai (1989) and Zhang et al. (2019), a key seems to be a process where thermal energy of a SNR plasma is somehow efficiently dissipated into interacting clouds.

In this thesis, we perform spatial resolved spectroscopy of thermal X-rays from RP-SNRs aiming to comprehensively understand the physical origin of the RPs in SNRs. We select W44 and IC 443 as the best targets to carry out this study. Radio and infrared observations revealed the detailed distribution of interacting clouds with these SNRs. W44 and IC 443 have large apparent sizes, which help us perform spatially resolved spectroscopy. We discuss implications of the obtained results by comparing them with those of previous works on other RP-SNRs.

The other topic concerning studies of SNRs interacting dense clouds is neutral Fe Kα line emission from dense gas in the vicinity of some SNRs, which can be best interpreted as K-shell ionization of Fe atoms in the gas by sub-relativistic particles accelerated in the SNRs (e.g., Okon et al., 2018; Nobukawa et al., 2018). The results, if the authors' claims are correct, indicate that the Fe Kα line can serve as a diagnostic tool to probe sub-relativistic particles at acceleration sites, which were almost unexplored until recently. Information on such particles is important to estimate total energy transferred into accelerated particles in each SNR and to consider the injection mechanism of thermal particles into the acceleration process.

In this thesis, we construct a model to predict structures of lines from multiple-ionized Fe ions in dense clouds bombarded by sub-relativistic particles accelerated in SNRs using the knowledge from beam experiments. Based on this model, we propose a novel method of providing clear evidence for sub-relativistic particles and furthermore of constraining their composition, with high resolution spectroscopy enabled by future X-ray satellites such as *XRISM*.

In Chapter 2, we summarize the overviews of supernovae and SNRs. In Chapters 3, we review the current understandings of SNR plasma, and galactic cosmic rays and particle acceleration in SNRs. Chapter 4 gives brief descriptions of *XMM-Newton* and *XRISM*. Chapter 5 describes the analyses and results on W44 and IC 443, and discussion on the physical origin of RPs. In Chapter 6, we explain the detailed calculation of the line structures as evidence of sub-relativistic particles, and show a model curve expected with *XRISM*. The final conclusions of this thesis are given in Chapter 7.

Chapter 2

Supernova and Supernova Remnants

2.1 Supernova

A Supernova (SN) is an explosion of a star at the end of its lifetime. The luminosity of an SN is comparable to that of the host galaxy, and its explosion energy is typically $\sim 10^{51}$ erg. Modern estimates predict that in every few decades one SN event should occur in a galaxy (e.g., van den Bergh & Tammann, 1991). Once the SNe occur, they brightly shine in multi-bands from optical to gamma-rays. The observed light curves and spectra are well known to shows very diversity and they are considered to reflect the properties of the pre-explosion star and a gas environment, and so on. In this chapter, we explain the classification of the SNe and nucleosynthesis in stars.

2.1.1 Classification of Supernovae

Classically, SNe have been typed based on their optical spectra around their peak luminosity. Figure 2.1 shows the scheme of the classification. The SNe are first divided into two types, Types I and II (e.g., Minkowski, 1941). The former exhibit no hydrogen lines, whereas the latter do show the hydrogen lines. Type I SNe are further divided into Type Ia, Type Ib, and Type Ic, according to the presences of Si and He lines (e.g., Elias et al., 1985). The difference of the line features is considered to be attributed to whether or not the pre-explosion stars have the hydrogen, He, and Si outer layers. On the other hand, Types II-P and II-L, which are subclasses of Type II SNe, are characterized by the shapes of their light curves as shown in Figure 2.2. Light curves of Type II-L SNe decline linearly in magnitude after their peaks, whereas that of Type II-P SNe have a plateau with almost constant brightness for a period of nearly 100 days (e.g., Barbon et al., 1973). The plateau phase can be seen if the star loses a hydrogen envelope before its explosion as discussed by some authors (e.g., Filippenko, 1997). Based on the underlying explosion mechanisms, above SNe classes are meaningfully classified into two broad categories, Type Ia and core-collapse SNe. We describe the characteristics of the two types in the following paragraphs.

Type Ia Supernovae

Type Ia SNe are considered to be caused by thermonuclear disruption of carbon-oxygen white dwarfs in binary systems. The nuclear disruption advances violently so that the progenitor star is totally disrupted by the nuclear reaction energy, leaving no compact objects such as a

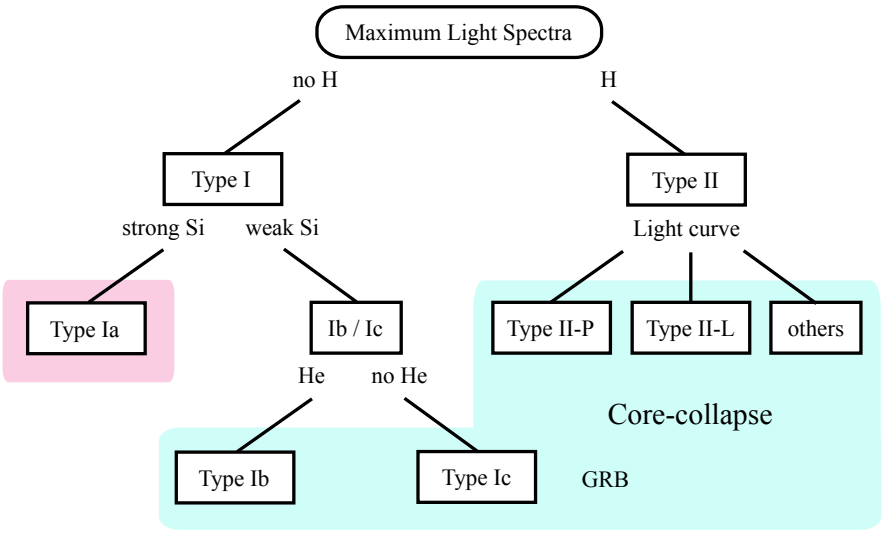

Figure 2.1: Classification scheme of SNe based on their light curves and line features in them.

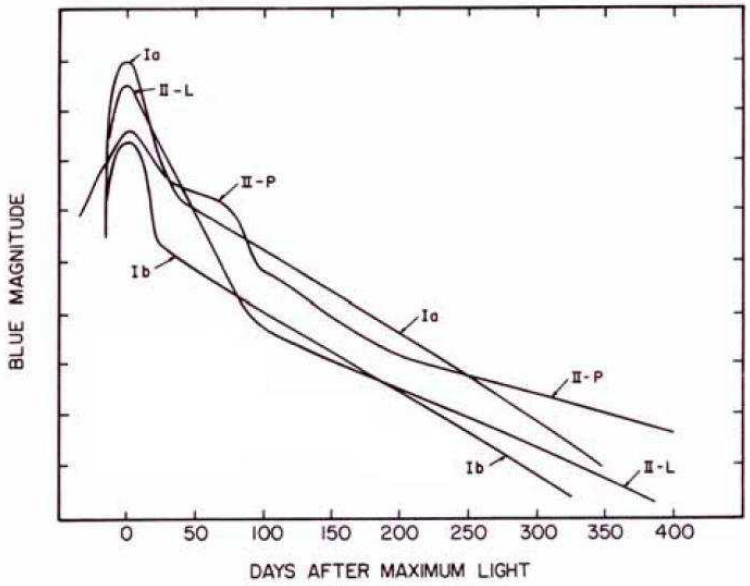

Figure 2.2: Comparison of light curves for Type I, II-P and II-L supernovae (Wheeler et al., 1990).

neutron star nor a black hole behind. The thermonuclear-disruption mechanism was originally proposed by Hoyle & Fowler (1960). Arnett (1969) and Nomoto et al. (1976, 1984) developed this idea into a carbon supersonic burning (detonation) and a subsonic carbon burning (deflagration) models, respectively. The two are widely regarded as the standard models for Type Ia SNe.

Two plausible channels for Type Ia SNe have been mainly proposed. One is the single-degenerate (SD) scenario (Whelan & Iben, 1973), where a white dwarf accretes matter from a non-degenerate companion star, typically main sequence or red giant stars, subsequently leading to the SNe. Under the mass accretion, the white dwarf builds up its mass until it approaches the Chandrasekhar limit of $\sim 1.4\ M_\odot$ ($M_{\rm ch}$), and eventually ignites. The other is the double-degenerate (DD) scenario (Webbink, 1984). In this scenario, an SNe occurs by a dynamical merger of two white dwarfs forming a binary system. Recent multi-wavelength observations provided indirect evidence for both scenarios. For instance, Li et al. (2011) reported no presence of the companion star in the images of SN 2011fe, which agrees with the DD scenario. On the other hand, Yamaguchi et al. (2015), based on the X-ray spectral analyses of SNR 3C 397, constrained an abundance pattern of iron group elements, which is naturally expected in the SD scenario. These results, along with the data of Perseus cluster with *Hitomi* (Hitomi Collaboration et al., 2017), imply that both channels make a significant contribution to the SN Ia rate in the galaxies.

Core-collapse Supernovae

Core-collapse SNe are considered to be the results of implosions of cores of massive stars with typically $\gtrsim 10\ M_\odot$. While the detailed explosion mechanism is still under debate, several promising scenarios are proposed based on theoretical and observational works. The best studied one is the neutrino heating mechanism, whose basic idea was first proposed by Colgate & White (1966) and later reinforced by Bethe & Wilson (1985). We focus on the mechanism and briefly explain it. A massive star evolves through the change of its composition via stellar nucleosynthesis as discussed in Section 2.1.2. As shown in Figure 2.3, massive stars have a Fe core at the final stage of its stellar evolution. Fe is the most stable element so that the heavier elements than Fe are not synthesized, resulting in continuing to increase the internal temperature of the core. In the very hot core, Fe absorbs gamma-rays emitted from it, and decays via a photo-dissociation process. Once the photo-dissociation of Fe and subsequently reactions occur in the hot core as follows,

$$
\begin{aligned}
^{56}\mathrm{Fe} + \gamma &\rightarrow 13\,^{4}\mathrm{He} + 4\mathrm{n} - 124.4\ \mathrm{MeV} && (2.1)\\
^{4}\mathrm{He} &\rightarrow 2\mathrm{p} + 2\mathrm{n} - 28.3\ \mathrm{MeV} && (2.2)\\
\mathrm{p} + \mathrm{e}^{-} &\rightarrow n + \nu_e, && (2.3)
\end{aligned}
$$

the core cannot be supported by any further nuclear fusion reactions or electron degeneracy pressure, leading to the core collapsing to a neutron star or black hole. The core collapse is halted by neutron degeneracy so that the falling materials are bounced and form a bounce shock. Although the bounce shock decays once inside the star, the shock is reenergized by neutrino energy deposition, resulting in the explosion.

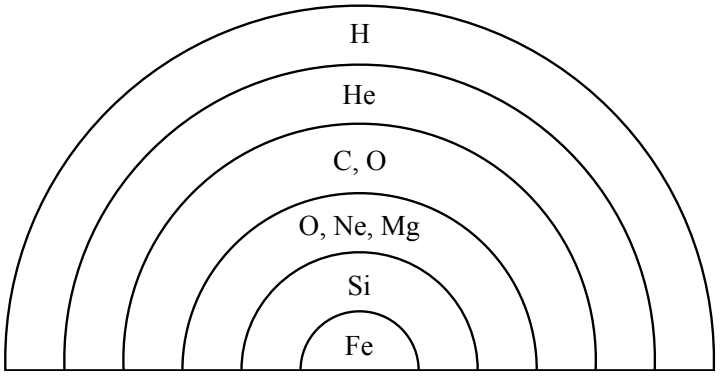

Figure 2.3: Scheme of the profiles of synthesized elements in a massive star. The scale is not exact.

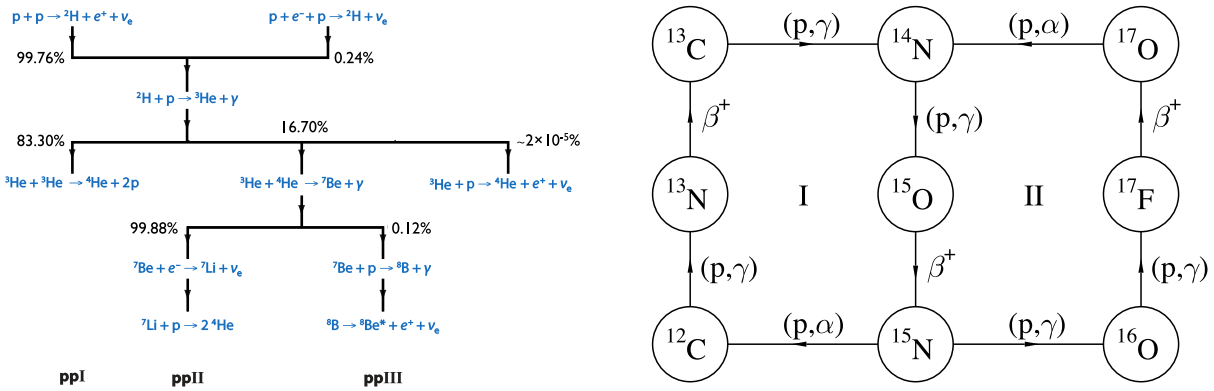

Figure 2.4: Reaction networks of (left) pp-chain and (right) CNO cycle (Adelberger et al., 2011).

2.1.2 Nucleosynthesis

Stellar Nucleosynthesis

Stellar nucleosynthesis is a process where heavy elements are synthesized within stars. As the stars evolve first by burning hydrogen (main sequence star), then He (red giant star), and progressively burning higher elements, their abundance composition changes over their life. Figure 2.4 and Equations 2.4–2.6 show the p-p chain and CNO (carbon-nitrogen-oxygen) cycle, and triple α reaction, respectively,

$$^4\mathrm{He} + ^4\mathrm{He} \rightarrow ^8\mathrm{Be} - 92\ \mathrm{keV}, \tag{2.4}$$

$$^4\mathrm{He} + ^8\mathrm{Be} \rightarrow ^{12}\mathrm{C}^* - 287\ \mathrm{keV}, \tag{2.5}$$

$$^{12}\mathrm{C}^* \rightarrow ^{12}\mathrm{C} + 7.65\ \mathrm{MeV}. \tag{2.6}$$

Abundant hydrogen and He are synthesized into elements such as C and O through these processes. If the stellar mass is $\lesssim 10\ M_\odot$, subsequently C and O burnings do not progress. Therefore, the stars have a core composed of C and O. Near the end of the nuclear burning stage, low mass stars are considered to expel most of their outer hydrogen and He layers. Only the hot core remains and becomes a white dwarf.

Massive stars ($\gtrsim 10\ M_\odot$) have higher core-temperatures than low mass stars ($\lesssim 10\ M_\odot$). Therefore, the synthesized C and O burnings occur, and heavy elements up to Fe are synthesized through continues reactions as follows,

$$\begin{aligned} {}^{12}\mathrm{C} + {}^{12}\mathrm{C} &\rightarrow \mathrm{Mg}^* \\ &\rightarrow {}^{23}\mathrm{Na} + {}^{1}\mathrm{H} + 2.238\ \mathrm{MeV}, \\ &\rightarrow {}^{20}\mathrm{Ne} + {}^{4}\mathrm{He} + 4.616\ \mathrm{MeV}, \\ &\rightarrow {}^{23}\mathrm{Mg} + \mathrm{n} - 2.605\ \mathrm{MeV}, \\ &\rightarrow {}^{24}\mathrm{Mg} + 13.931\ \mathrm{MeV}, \\ &\rightarrow {}^{16}\mathrm{O} + 2\alpha - 0.114\ \mathrm{MeV}. \end{aligned} \tag{2.7}$$

$$\begin{aligned} {}^{16}\mathrm{O} + {}^{16}\mathrm{O} &\rightarrow {}^{32}\mathrm{S} + 16.541\ \mathrm{MeV}, \\ &\rightarrow {}^{31}\mathrm{P} + 7.677\ \mathrm{MeV}, \\ &\rightarrow {}^{31}\mathrm{P} + \mathrm{n} + 1.453\ \mathrm{MeV}, \\ &\rightarrow {}^{28}\mathrm{Si} + \alpha + 9.593\ \mathrm{MeV}, \\ &\rightarrow {}^{24}\mathrm{Mg} + 2\alpha - 0.393\ \mathrm{MeV}. \end{aligned} \tag{2.8}$$

$$^{28}\mathrm{Si} + \alpha \rightarrow {}^{32}\mathrm{S} + \alpha \rightarrow {}^{36}\mathrm{Ar}... \rightarrow {}^{56}\mathrm{Fe}, \tag{2.9}$$

$$^{28}\mathrm{Si} + {}^{28}\mathrm{Si} \rightarrow {}^{56}\mathrm{Fe}. \tag{2.10}$$

As the nuclear reactions progress one after another inside the star, newly synthesized elements accumulate inside the star. Abundance profiles in the massive star is an onion-like at the final stage of its evolution (Figure 2.3).

Explosive nucleosynthesis

Table 2.1: Explosive nucleosynthesis.

Burning Process	Main Products	Ignition temperature (10^9 K)
C/Ne burning	Ne, O, Mg, Si	~ 2
O burning	O, Si, S, Ar, Ca	$\sim$ 3–4
Incomplete Si burning	Si, S, Ar, Ca	~ 4
Complete Si burning	Fe, Co, Ni, Zn	$>\sim 5$

Detail parameters from Thielemann et al. (1996).

Explosive nucleosynthesis is a nuclear fusion process in SNe. In both Type Ia and core-collapse SNe, a shock wave propagating inside a star rapidly elevate its internal temperature so that nuclear reactions drastically progress, resulting in changing of the composition in the star in a very short time. Table 2.1 summarizes dominant nucleosynthesis processes and their ignition temperatures. The abundances of synthesized elements strongly depend on the type of a SN and the mass of a star before a SN. Figure 2.5 shows one example of abundance profiles of elements synthesized in a core-collapse SN of a massive star, calculated by Thielemann et al.

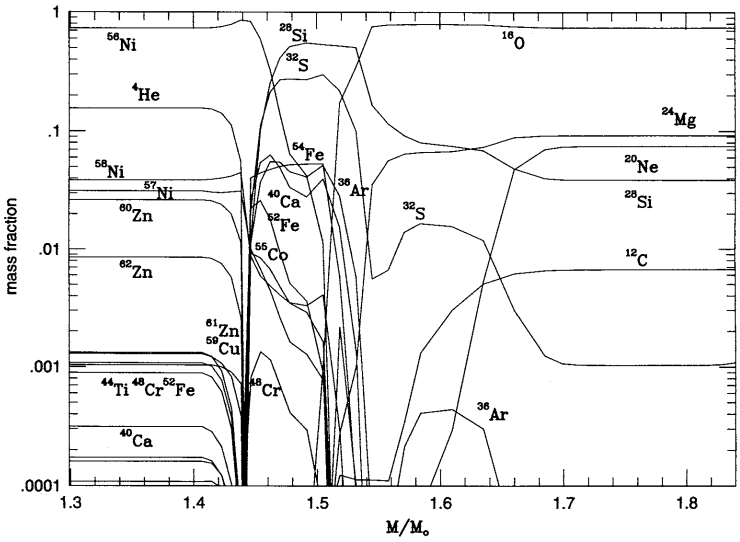

Figure 2.5: Abundance profiles of elements synthesized in core collapse SNe with stellar mass of 15 $M_\odot$ (Thielemann et al., 1996). The horizontal axis indicates a mass occupied by a sphere with a radius, inside a star. The vertical axis represent a mass fraction of each element in the sphere.

(1996). Our target SNRs in Chapter 5 are indeed considered to be the remnants of core-collapse SNe (e.g., Wolszczan et al., 1991; Olbert et al., 2001). It is notable that large amounts of heavy elements such as Ca, Fe, and Ni in addition to light elements of Ne, Mg, Si, S, and so on, are synthesized through the process. The produced ^{56}Ni decays to ^{56}Fe as follows,

$$^{56}\mathrm{Ni} \xrightarrow{t_{1/2}=6.1\ \mathrm{days}} {}^{56}\mathrm{Co} \xrightarrow{t_{1/2}=77\ \mathrm{days}} {}^{56}\mathrm{Fe}, \tag{2.11}$$

where $t_{1/2}$ is a half-life.

2.2 Supernova Remnant

A SNR is the remains of an SN. SNRs have expanding shock waves formed by interaction between ejecta in the SN and the swept-up ISM, and hot plasma consisting of them. The section gives brief descriptions for the formation of the shock wave in SNRs, the dynamical evolution of the SNRs, and the classification of SNRs.

2.2.1 Shock Wave

We summarize useful relations for strong (plane) shock waves formed by expanding materials into a stationary surrounding gas. Across the shock front, the conservations of mass, momentum, and energy are given by below equations,

$$\rho_\mathrm{u} v_\mathrm{u} = \rho_\mathrm{d} v_\mathrm{d}, \tag{2.12}$$

$$\rho_\mathrm{u} v_\mathrm{u}^2 + p_\mathrm{u} = \rho_\mathrm{d} v_\mathrm{d}^2 + p_\mathrm{d}, \tag{2.13}$$

$$\frac{1}{2} v_\mathrm{u}^2 + \omega_\mathrm{u} = \frac{1}{2} v_\mathrm{d}^2 + \omega_\mathrm{d}, \tag{2.14}$$

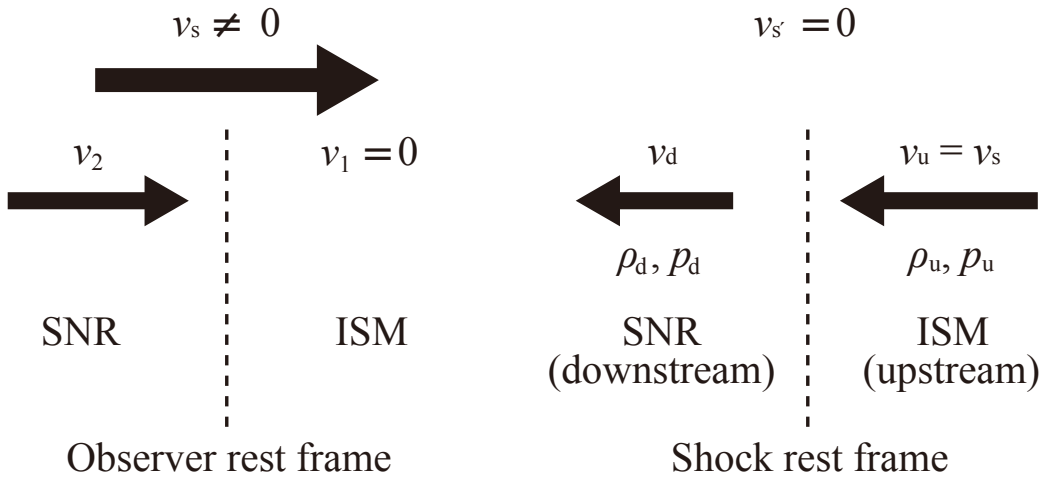

Figure 2.6: Schematic view around the shock front in (left) observer rest frame and (right) shock rest frame.

where ρ, v, p, and ω are the density, velocity, pressure, and specific enthalpy, respectively. The notations u and d correspond to the upstream and downstream as shown in Figure 2.6. The specific enthalpy in ideal gas is described as,

$$\omega = C_p T = \frac{\gamma p}{(\gamma-1)\rho}, \tag{2.15}$$

where γ is the specific heat ratio (= C_p/C_V). Under the assumption of the shock conditions ($p_d/p_u \gg 1$), above equations can be translated into the ratio of pressure p, velocity v, density ρ, and temperature T,

$$\frac{p_d}{p_u} = \frac{2\gamma {M_u}^2}{\gamma+1}, \tag{2.16}$$

$$\frac{v_d}{v_u} = \frac{\rho_u}{\rho_d} = \frac{\gamma-1}{\gamma+1}, \tag{2.17}$$

$$\frac{T_d}{T_u} = \frac{2\gamma(\gamma-1){M_u}^2}{(\gamma+1)^2}, \tag{2.18}$$

where M is the Mach number (= $v/\sqrt{\gamma p/\rho}$). For monoatomic gas (γ = 5/3), the ratio of the density, velocity, temperature are 4 (= ρ_d/ρ_u), 1/4 (= v_d/v_u), and $5/16{M_u}^2$ (= T_d/T_u), respectively.

Assuming that the upstream velocity v_u equals to the shock speed v_s, we can derive the mean post-shock temperature kT_s ($= kT_d$) as,

$$kT_s = \frac{2(\gamma-1)\,\mu m_H {v_s}^2}{(\gamma+1)^2} = \frac{3}{16}\mu m_H v_s^2, \tag{2.19}$$

where k, μ, and m_H are the Boltzmann constant, the mean atomic weight, and the hydrogen mass, respectively. Equation 2.19 can be interpreted as the conversion equation from the kinetic energy of ejecta into internal energy of SNR plasma. We can see that the shock ($v_s \sim 10^3$ km/s) in young SNRs (typically $\lesssim 10^3$ yr) can heat the plasma up to $\sim$1 keV.

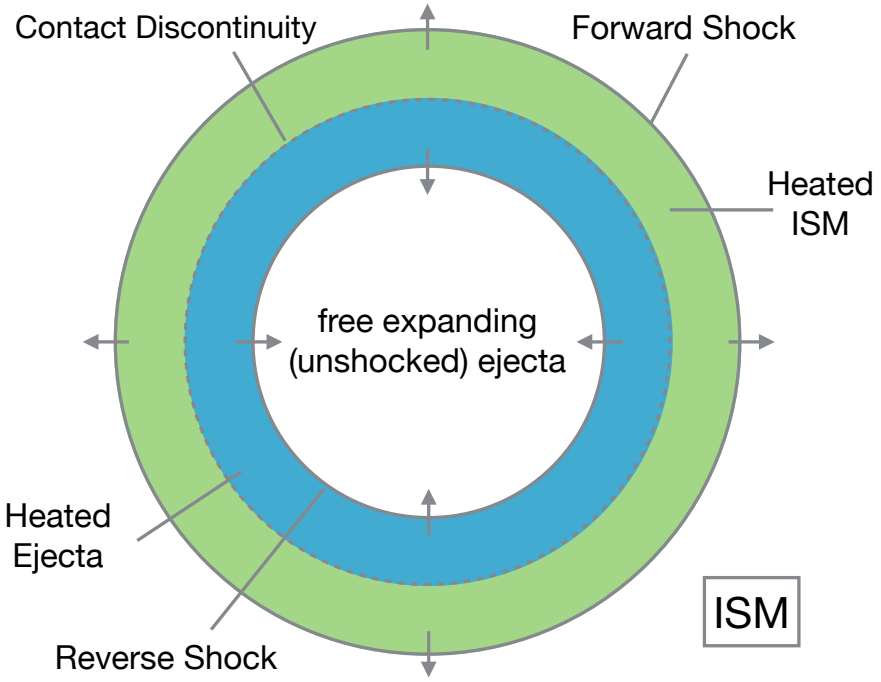

Figure 2.7: Sectional drawing of an SNR in the free expansion and adiabatic phases.

2.2.2 Evolution of SNRs

SNRs typically last several 10^5 years before they disperse into the ISM. In an initial phase, the so-called free expansion phase, the mass of the swept-up ISM ($M_{\rm ISM}$) is smaller than that of ejecta ($M_{\rm ej}$) so that the ejecta is hardly decelerated and keeps most of the kinetic energy released in the SNe. Therefore, the expansion velocity $v_{\rm s}$ can be expressed as,

$$v_{\rm s} = \sqrt{\frac{2E}{M_{\rm ej}}} \sim 1.0 \times 10^4 \left(\frac{E}{10^{51}\ {\rm erg}}\right)^{1/2} \left(\frac{M_{\rm ej}}{M_\odot}\right)^{-1/2} {\rm km\,s^{-1}}, \tag{2.20}$$

where E is the explosion energy. The formed shock wave precedes the expanding ejecta so that the shock is called the forward shock as shown in Figure 2.7. The free expansion phase lasts for 100–200 years.

As the mass of the swept-up ISM increases, the ISM starts to impede the free expansion of the ejecta. Until the energy loss by a radiation cooling is still negligible compared to the initial energy, the SNR evolves adiabatically. The phase is called the adiabatic or Sedov phase. Sedov (1959) proposed a self-similar solution that describes the dynamical evolution of an SNR under the assumption of a point explosion in a uniform medium. The shock radius $R_{\rm s}$, the shock

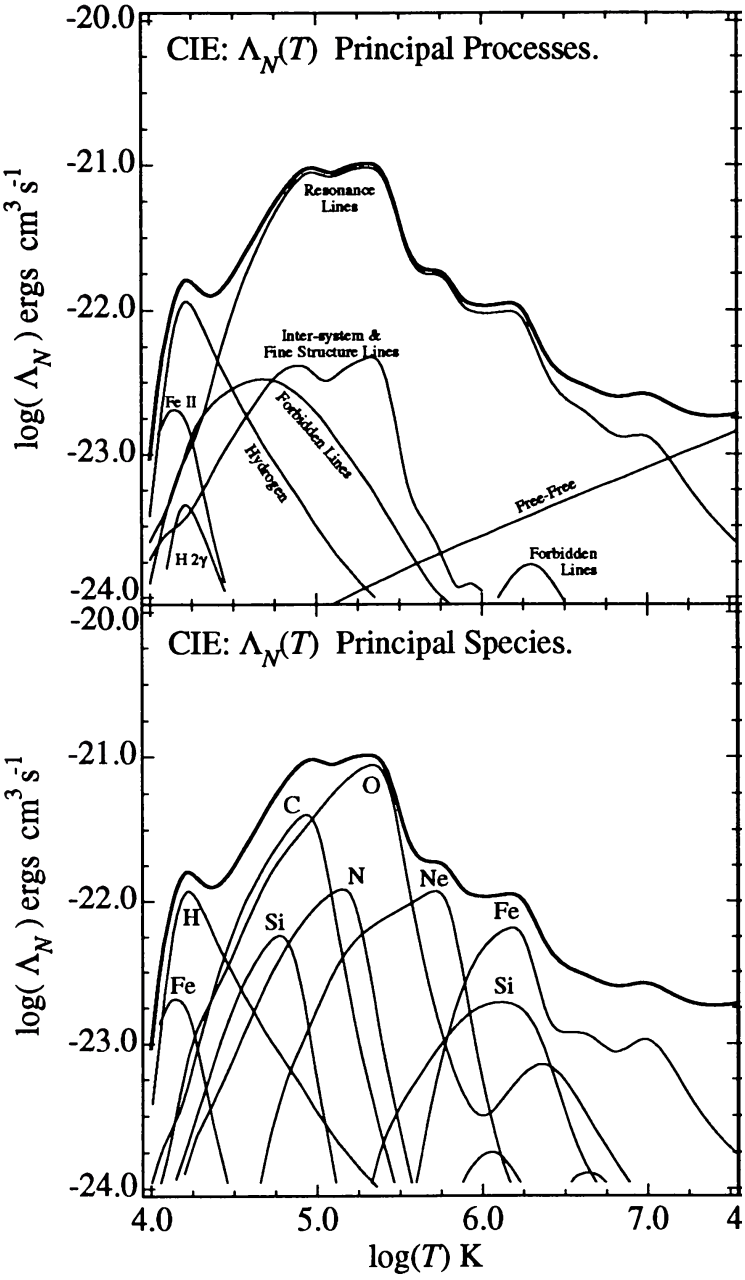

Figure 2.8: Cooling coefficient for an optically-thin thermal plasma as a function of the plasma temperature (Sutherland & Dopita, 1993).

velocity v_s, and the mean temperature T_s just behind the shock front can be written as,

$$R_s = 4\times10^{14}\left(\frac{t}{10^4\ \mathrm{yr}}\right)^{2/5}\left(\frac{E}{10\ \mathrm{erg}}\right)^{1/5}\left(\frac{n_0}{1\ \mathrm{cm}^{-3}}\right)^{-1/5}\mathrm{km}, \quad (2.21)$$

$$v_s = \frac{dR_s}{dt} = 5\times10^{2}\left(\frac{t}{10^4\ \mathrm{yr}}\right)^{-3/5}\left(\frac{E}{10\ \mathrm{erg}}\right)^{1/5}\left(\frac{n_0}{1\ \mathrm{cm}^{-3}}\right)^{-1/5}\mathrm{km\,s}^{-1}, \quad (2.22)$$

$$T_s = 3\times10^{6}\left(\frac{t}{10^4\ \mathrm{yr}}\right)^{-3/5}\left(\frac{E}{10\ \mathrm{erg}}\right)^{1/5}\left(\frac{n_0}{1\ \mathrm{cm}^{-3}}\right)^{-1/5}\mathrm{K}. \quad (2.23)$$

The adiabatic phase lasts for 10,000–20,000 years. Until the end of this phase, $\sim 70\%$ of the initial explosion energy is converted to thermal energy of the swept-up ISM (Chevalier, 1974).

In the transition from the free expansion to adiabatic phases, the outer ejecta is decelerated by the swept-up ISM (see Equation 2.22) whereas the inner ejecta keeps freely expanding (see Equation 2.20). The inner ejecta is pushed back on the outer ejecta, and generates a reverse shock that propagates inward as discussed in McKee (1974). The forward shock heats surrounding the ISM, whereas the reverse shock does the ejecta component as shown in Figure 2.7.

When the SNR age exceeds $\sim 10^4$ yr, the radiative energy loss cannot be negligible. The SNR loses its internal energy by the radiative cooling so that the plasma temperature and density decreases and increases, respectively. Figure 2.8 shows the cooling coefficient for an optically-thin thermal plasma. The plot means that, as the plasma becomes cooler, the cooling speed increases. Eventually, when the shock slows down and its velocity is comparable to the sound speed in the ISM, the shock wave stands no longer. The SNRs merge into the ISM and cannot be identified.

2.2.3 Morphology of SNRs

SNRs are identified by radio emissions from GeV electrons accelerated at shocks formed by interaction between the ejecta and ISM. Currently, Green (2019) cataloged 265 SNRs and SNR candidates in our Galaxy. Most of the SNRs are well known to brightly shine in multi-bands in addition to radio. Some authors (e.g., Rho & Petre, 1998) pointed out morphological similarities among some SNRs in radio and X-ray bands. They are considered to reflect similar properties among the SNRs such as their environment and evolution history. Here, we explain the classification based on the radio and X-ray morphologies of the SNRs, and the properties.

Figure 2.9 shows the four representative types of SNRs, shell-like, plerionic, composite, and mixed-morphology (MM). Shell-like SNRs have limb-brightened radio and X-ray morphologies. Most of young SNRs are categorized into this type. Radio emission is mainly synchrotron radiation emitted from electrons accelerated in the blast wave. X-rays are thermal emission from shock heated plasma and/or X-ray synchrotron from electrons in a TeV order. The shell type is currently considered to be the most basic type. The plerionic SNRs have center-filled X-rays and radio emission which are from a pulsar (PSR) and pulsar wind nebulae (PWNe). The Crab Nebula is the most famous remnant of this type, and, therefore, the plerionic type is often called Crab-like. Green (1986) claimed that the type can be seen if the SN occurs in very tenuous ISM or the SN energy is small. Composite SNRs have shell-like and center-filled morphologies in X-ray and radio bands. In this type, both emissions from the PSR/PWN and from the plasma and/or accelerated particles are observed. MM-SNRs are characterized by the center-filled X-rays and the limb-brightened radio emission. Although ~ 25 % of the X-ray-detected SNRs in our Galaxy are categorized into this class (Rho & Petre, 1998), the formation

(a) Tycho's SNR (Shell type)

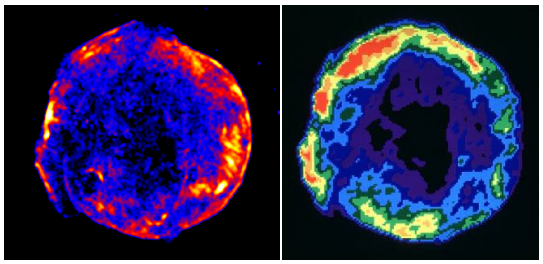

(b) Crab (Plerion type)

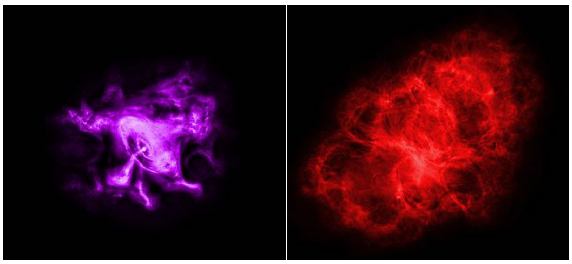

(c) G11.2–0.3 (Composite type)

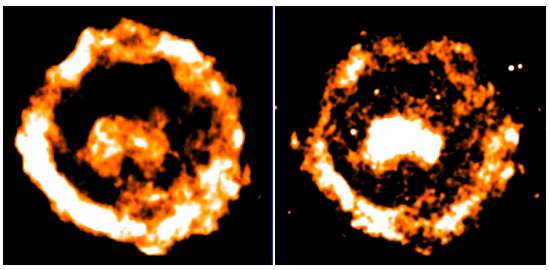

(d) W44 (MM type)

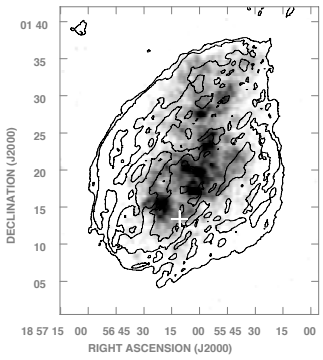

Figure 2.9: X-ray and radio images of four type SNRs, (a) Tyhco's SNR (Credit Radio; Credit Radio: NSF/NRAO/VLA), (b) Crab (X-ray: NASA/CXC/SAO; Radio: NSF/NRAO/VLA), (c) G11.2−0.3 (Borkowski et al., 2016), (d) W44 (Castelletti et al., 2007). For all panels, the left and right correspond to X-ray and radio band images.

mechanism has not been understood. Most MM-SNRs are actually known to be interacting with molecular clouds (e.g., Lazendic & Slane, 2006), suggesting the association of the formation mechanism and the interaction.

Chapter 3

Thermal Plasma and Particle Acceleration in SNRs

3.1 Thermal Plasma in SNRs

Studies of SNR plasma provide us with important information on the SNR's environment and evolution history. SNR plasma often emits thermal X-rays reflecting its electron temperature, ionization degree, and abundances of elements. Therefore, X-ray plasma diagnosis has been a powerful tool to investigate the properties of SNR plasma. Here, we summarize the radiation mechanisms of the X-ray emission form the SNR plasma and the previous works concerning the SNR plasma.

3.1.1 X-rays from Thermal Plasma

Figure 3.1 shows models of X-ray emission from optically thin plasma found in SNRs. The typical X-ray spectra of SNRs have continuum components and many line emissions whose information such as intensity and center energy is a key to constraining plasma parameters. In the subsection, we focus on bremsstrahlung, radiative recombination continua (RRCs), and emission lines.

Bremsstrahlung

When charged particles are slowing down or deflected by other particles, the charged particles emit electromagnetic radiation, called bremsstrahlung. Generally, bremsstrahlung from electrons is more intense than that from ions in the astrophysical plasma since electrons are scattered more easily than protons because of its smaller mass. The emissivity $\epsilon_{\rm ff}$ of the bremsstrahlung emitted by electrons obeying the Maxwell-Boltzmann distribution is given by,

$$\epsilon_{\rm ff} = \frac{32\pi e^6}{3 m_e c^3}\left(\frac{2\pi}{3km_e}\right)^{1/2} {T_e}^{-1/2} {Z_i}^2 n_e n_i \exp\left(-E/kT_e\right)\overline{g_{ff}}, \tag{3.1}$$

where e, c, k, m_e, Z_i, n_e, n_i, E, and $\overline{g_{ff}}$ are the electron charge, light speed, Boltzmann constant, electron mass, atomic number of ions, number densities of electrons and ions, photon energy, and velocity averaged Gaunt factor, respectively (Rybicki & Lightman, 1979). For thermal

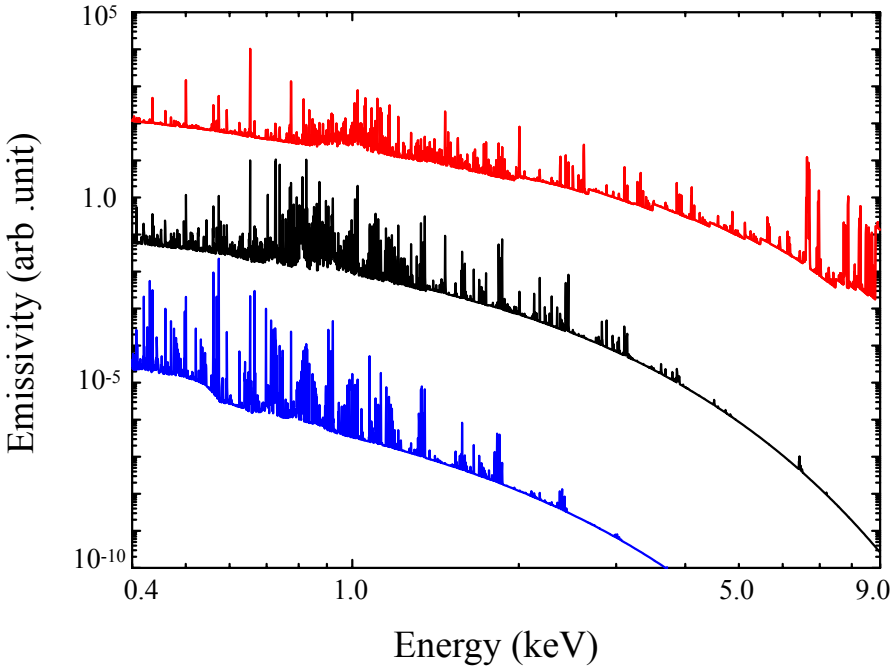

Figure 3.1: Thermal emission from X-ray emitting plasma. Black, red, and blue curves represent the models of CIE plasma, and IP, and RP, respectively.

plasma emitting X-rays, the Gaunt factor $\overline{g_{ff}}$ is simply approximated as,

$$\overline{g_{ff}} = \left(\frac{3kT_e}{\pi E}\right)^{1/2}. \tag{3.2}$$

The asymptotic behavior of the emissivity is written as,

$$\epsilon_{\rm ff} \propto \begin{cases} E^{-0.4} & (E \leq kT_e) \\ \exp(-E/kT_e) & (E > kT_e). \end{cases} \tag{3.3}$$

Therefore, electron temperature can be constrained based on the spectral shape of the bremsstrahlung continuum. The luminosity L is calculated by the emissivity integrated over the volume and frequency, and summed of contributions of ions in plasma as follows,

$$L = \sum_i \int \epsilon_{\rm ff}\, dV\, d\nu \sim 1.7\times10^{-27}\, T_e^{-1/2} \sum_i Z_i^2\, n_e\, n_i\, V \quad [{\rm erg\,s^{-1}}] \tag{3.4}$$

$$\sim 2.9\times10^{-27}\, T_e^{-1/2}\, n_{\rm H}\, n_e\, V \quad [{\rm erg\,s^{-1}}], \tag{3.5}$$

where $n_{\rm H}$ is the number density of hydorogen nucleus. Here, we used a helpful relation $\sum_i Z_i^2\, n_i \sim 1.7\, n_{\rm H}$ in typical SNR plasma with solar abundance.

Radiative Recombination Continuum

RRCs are continua emitted by free electrons when they are captured in free orbits of ionized ions. Figures 3.2 and 3.3 show schematics of the radiation process and energy spectra of RRCs, respectively. The energy of the emitted photon is the sum of the kinetic energy of electron before

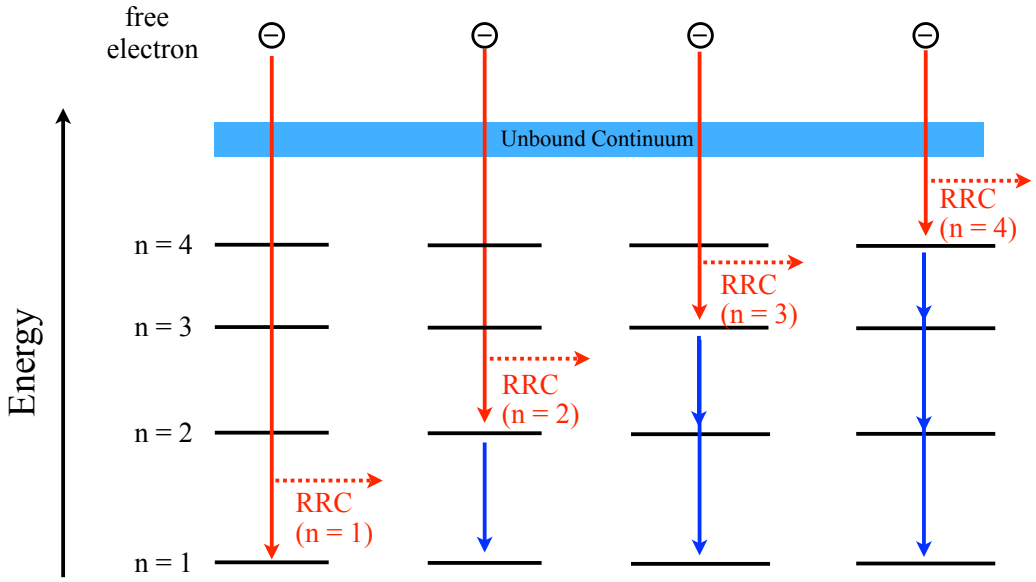

Figure 3.2: Schematics of an emission mechanism for RRCs and transition lines after free electrons are captured by ions.

the recombination and the binding energy of the captured electron after the recombination. The spectrum has an edge reflecting the binding energy, and the continuum shape depends on the kinetic energy. Therefore, the behavior of the emissivity of RRCs from thermal plasma is approximately written as

$$\epsilon_{\rm bf} \propto \begin{cases} 0 & (E < I) \\ \exp\left(-E/kT_e\right) & (E \geq I), \end{cases} \tag{3.6}$$

where I is the binding energy.

Line Emission

Emission lines are caused by bound-bound transitions of electrons between two discrete quantum levels due to inner-shell ionization, excitation, and cascade decay after the recombination. Energy of the emission line corresponds to the difference between the two levels. In the cases of a hydrogen atom or other H-like ions, the Bohr model gives remarkably good approximations of the energies of the line emissions. The line energy due to the transitions between the levels with principal quantum numbers n and n' can be described as,

$$E_{\rm bb} \sim Z^2 R_y \left(\frac{1}{n^2} - \frac{1}{n'^2}\right), \tag{3.7}$$

where Z and R_y is the atomic number and Rydberg constant (= 13.6 eV), respectively. Figure 3.4 shows the energies of the Fe-Kα and Fe-Kβ emission lines as a function of the charge number of Fe ions. In general, as the ion is more ionized and the Coulomb screening between electrons in orbits become weaker, the line energy increases.

Figure 3.5 presents an example of Grotrian diagrams showing allowed electronic transitions between energy levels of atoms. Here, we show the diagram for one He-like ion. Energy

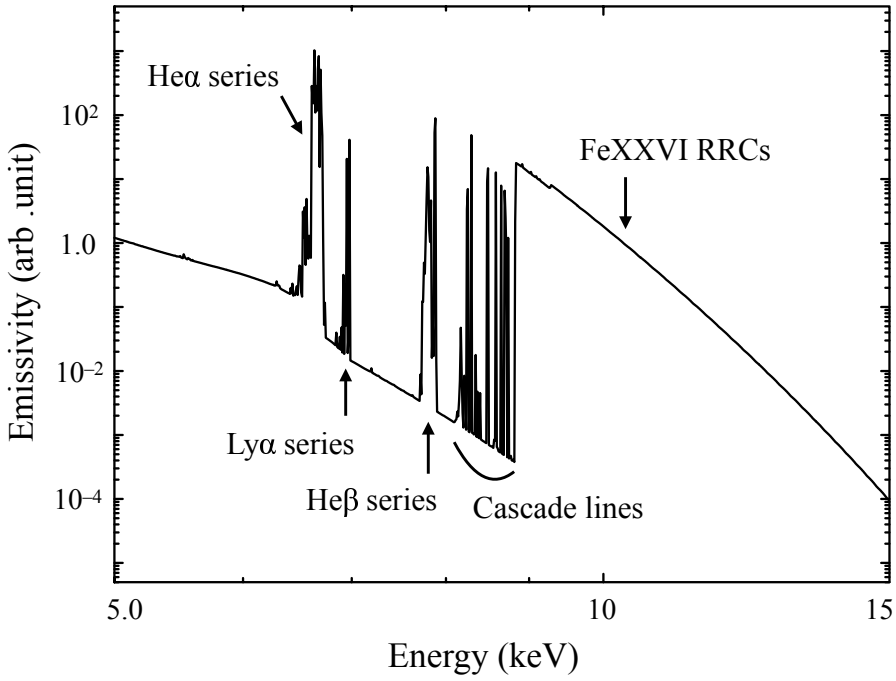

Figure 3.3: Emitted RRCs and emission lines after the recombination between electrons and Fe ions.

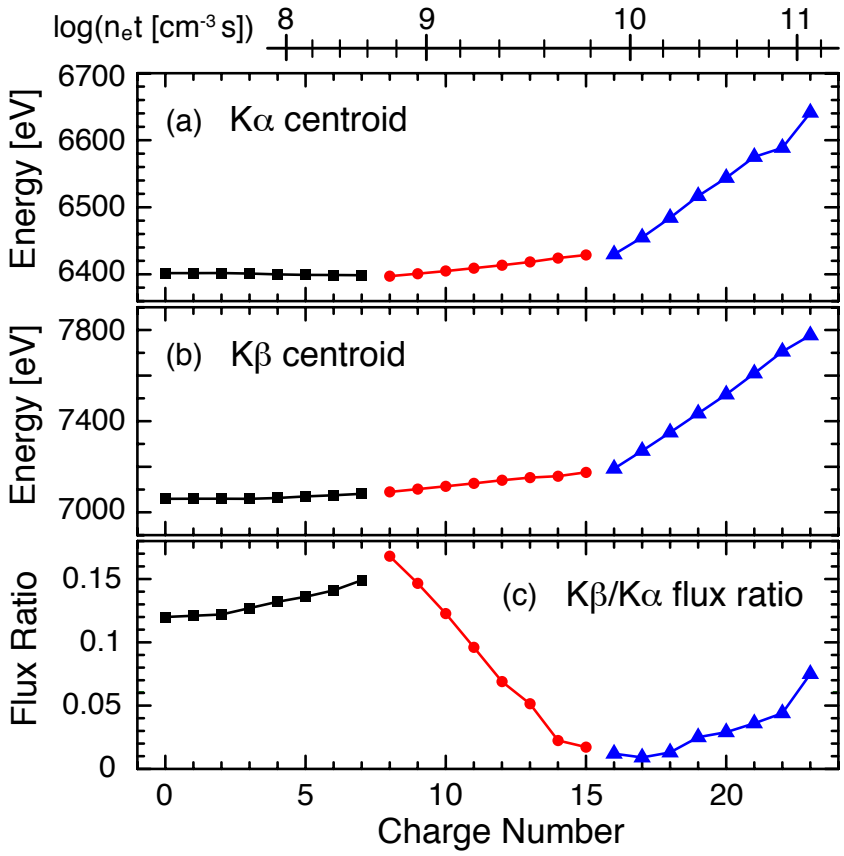

Figure 3.4: Center energies of the (a) Fe Kα and (b) Fe Kβ emission, and (c) the Kβ/Kα flux ratio as a function of the charge number of Fe ions (Yamaguchi et al., 2014).

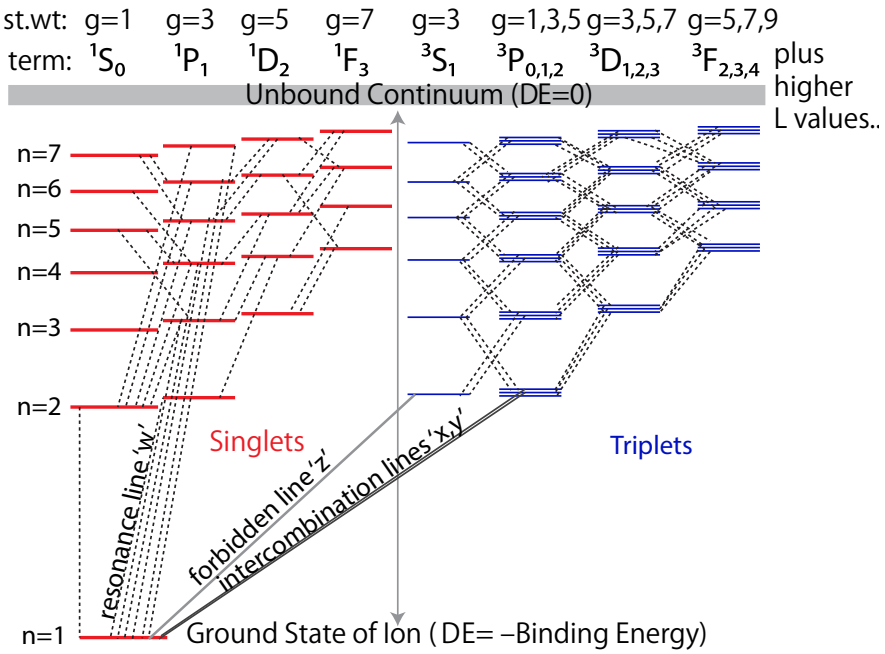

Figure 3.5: Grotrian diagram for a He-like ion with selected radiative transitions marked as dashed lines (Smith et al., 2014).

levels of atoms with multi electrons are more complicated because of the interactions of the electrons with each other. In Figure 3.4, each energy level reflects the differences of total spin angular momentum S or total orbital angular momentum L of the two electrons in addition to the principal quantum number n. Transition paths are restricted by selection rules based on quantum mechanics (e.g., conservation of spin angular momentum of electrons; conservation of orbital angular momentum between one electron and the emitted photon).

The line intensity has important information to constrain abundances and ionization degrees of ions in plasma. The line intensity (and the intensity of RRC) is proportional to $n_e n_i$ whereas the flux of bremsstrahlung is almost proportional to $n_e n_{\rm H}$ (see Equation 3.5). Therefore, we can determine the relative abundance ion (n_i/n_e) with the flux ratio of the components. Figure 3.4 shows the intensity ratio of Fe Kα to Fe Kβ emission lines. It is well known that the intensity ratio strongly depends on the number of or the arrangement of electrons in the atom. Note that we also must consider the rate of ionization and excitation, and recombination processes in a plasma in spectral analysis.

3.1.2 Standard Evolution of SNR Plasma

Thermalization of Particles in Plasmas

Particles in SNR plasma are thermalized through shock heating so that their temperatures are considered to follow Equation 2.19. The temperature of each particle species is proportional to its mass so that protons and ions have much higher temperature than that of electron. The particles, immediately after the shock heating, are considered to be kinematically in a non-equilibrium state. Miceli et al. (2019) succeed in measuring ion temperatures of the youngest nearby SNR, SN 1987A, with the *Chandra* X-ray telescope. The *Chandra* data indeed revealed that the temperature ratios of ions to protons are significantly large and increase linearly in

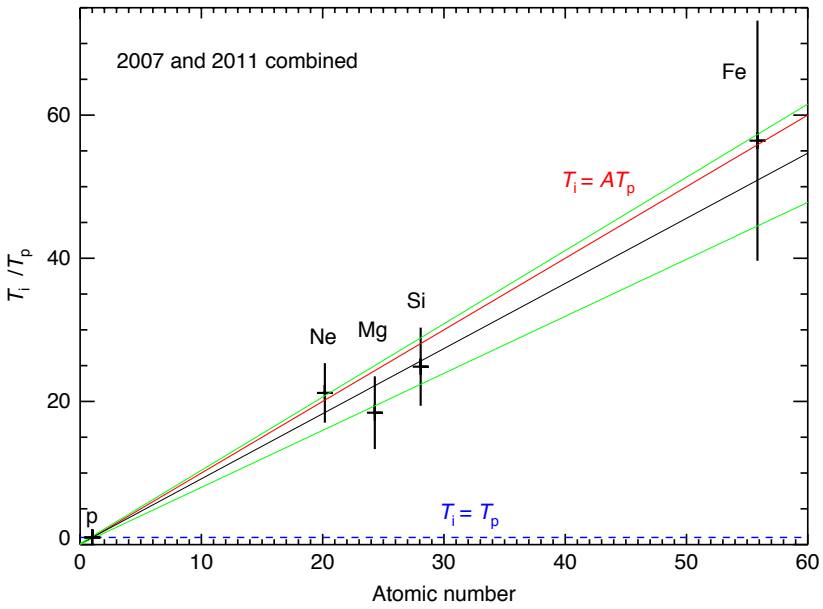

Figure 3.6: Temperature ratios of ions (Ne, Mg, Si, and Fe) to protons in SN 1987A. The red line marks the mass-proportional trend predicted by Equation 2.19, while the black line shows the best-fit curve with the 90 % confidence ranges indicated by the green lines (Miceli et al., 2019).

proportion to their mass ratio as shown in Figure 3.6.

After the heating of particles at the shock, electrons in the plasma are gradually heated through proton-electron and electron-ion collisions. The energy exchange continues until each particle has the same temperature, and the particles finally reach in a thermal equilibrium state. Masai (1984) gave the thermalization timescales of electron-electron t_{e-e} and electron-proton (ion) t_{e-i} due to Coulomb collision as,

$$t_{e-e} = 5.1 \times 10^8 \left(\frac{kT_e}{1\ \mathrm{keV}}\right)^{3/2} \left(\frac{n_e}{1\ \mathrm{cm}^{-3}}\right)^{-1} \left(\frac{\ln\Lambda}{30}\right)^{-1}\ \mathrm{s}, \tag{3.8}$$

$$\text{and}\quad t_{e-\mathrm{i}} = 3.2 \times 10^{11} < A_i >^{-2} < Z_i >^{-2} \left(\frac{kT_e}{1\ \mathrm{keV}}\right)^{3/2} \left(\frac{n_e}{1\ \mathrm{cm}^{-3}}\right)^{-1} \left(\frac{\ln\Lambda}{30}\right)^{-1}\ \mathrm{s}, \tag{3.9}$$

respectively, where kT_e, n_e, $< A_i >$, $< Z_i >$, and the $\ln\Lambda$ are the electron temperature, density, the averaged ion mass in atomic unit, the average ion charge, and the Coulomb logarithm ($\sim 25 - 30$). The timescales t_{e-e} and t_{e-p} are few 100 years and few 10 thousand years at $< A_i >=< Z_i >= 1$, $n_e = 1$ cm^{-3}, and $kT_e = 1$ keV, respectively. Generally, the electron-electron thermalization timescale t_{e-e} is considered to be much smaller than the proton-electron thermalization t_{e-p}, suggesting that the equilibrium between electrons precedes that between electrons and protons (and ions).

Evolution of Ionization State in Plasma

Besides the thermalization, heated electrons also ionize ions, which are nearly neutral immediately after the SNe. As ions are more ionized, the electron-ion recombination rate increases.

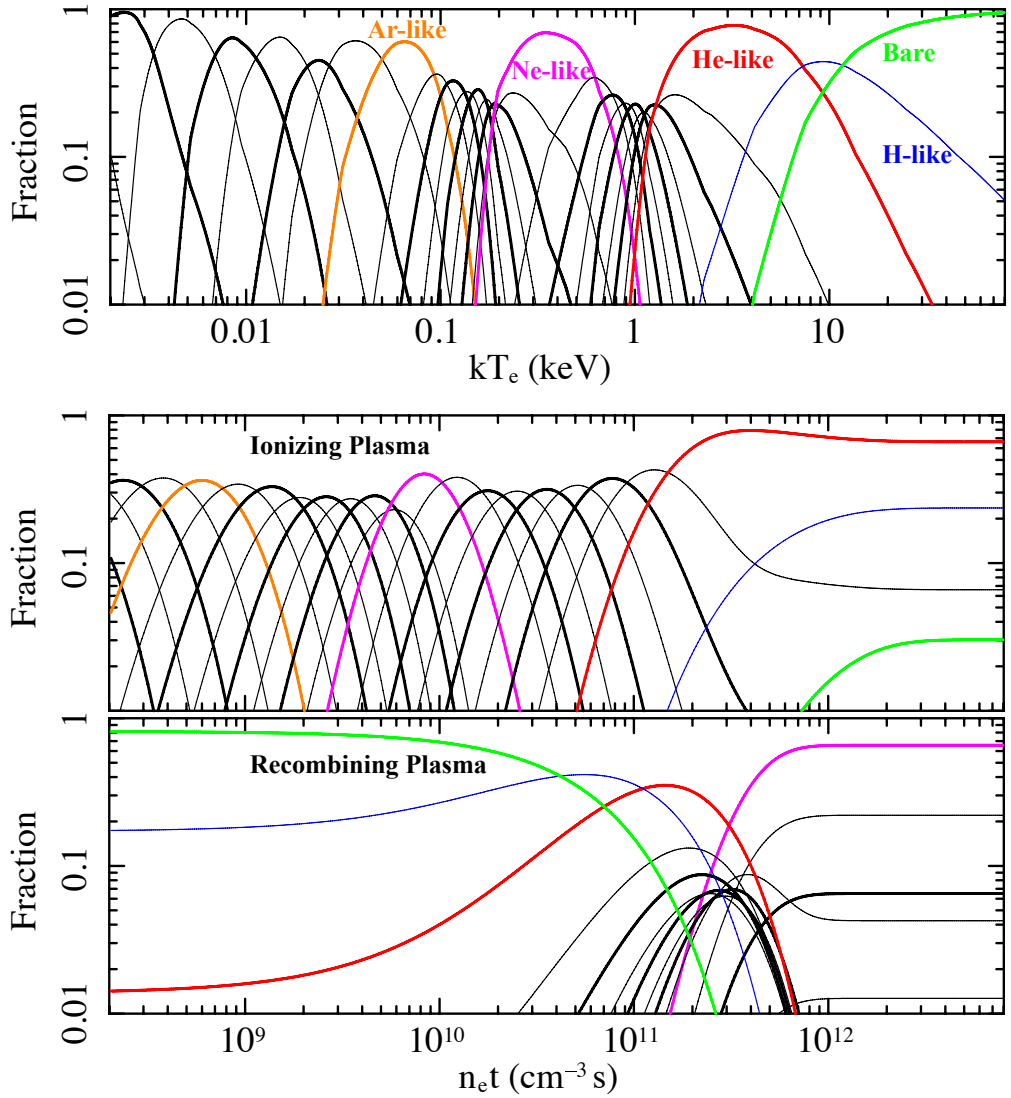

Figure 3.7: Charge fraction of Fe ions in (upper) CIE plasma and (middle) non equilibrium plasmas in ionization dominant phase and (bottom) in recombination dominant phase (Smith et al., 2014).

When the ionization and recombination rates are eventually equal, the plasma reaches collisional ionization equilibrium (CIE). The time evolution of ion fraction of each ion species is calculated by following:

$$\begin{aligned} \frac{dn_i}{dt} &= -n_e I_i n_i + n_e I_{i-1} n_{i-1} - n_e R_i n_i + n_e R_{i+1} n_{i+1}, \\ \text{or} \quad \frac{1}{n_e}\frac{dn_i}{dt} &= I_{i-1} n_{i-1} - (R_i + I_i) n_i + R_{i+1} n_{i+1}, \end{aligned} \tag{3.10}$$

where n_i, I_i, R_i, and n_e are the ion fraction of the i-times ionized ion, the ionization rate from the $(i-1)$-times ionized ion to i-times ionized ion, the recombination rate from $(i+1)$-times ionized ion to i-times ionized ion, and the electron density, respectively. Masai (1994) computed the characteristic timescale $t_{\rm ion}$ to reach the CIE state as,

$$\int n_e \, dt \sim 3 \times 10^{12} \ {\rm cm^{-3}\,s}. \tag{3.11}$$

In Figure 3.7, we present ion fraction of Fe ions in CIE and non-equilibrium plasmas in "ionization dominant phase" and "recombination dominant phase". SNR plasma is often in the non equilibrium ionization (NEI) state because the timescale is comparable to or longer than SNR ages.

The standard scenario of SNR plasma evolution has been established based on the above theoretical works and following observational data taken with many rocket experiments and satellite missions. After the opening of the X-ray window into the universe by Giacconi et al. (1962), surveys with the payload rockets revealed that the locations of some X-ray sources are consistent with those of SNRs such as Cassiopeia A, Tycho's SNR, and the Crab. Gorenstein et al. (1970) and Burginyon et al. (1975) discovered thermal bremsstrahlung and emission lines in the X-ray spectra of Cas A, Tycho's SNR, the Cygnus Loop, Vela X, and Puppies A, directly indicating the presence of hot plasmas at $\sim 10^7$ K. Tsunemi et al. (1986) measured the mean energies of lines from Si, S, Ar, Ca, and Fe ions with *Tenma*, and revealed that the energies are smaller than those expected in a CIE model. Figure 3.8 shows the spectra and the difference of center energies of line emissions. Tsunemi et al. (1986) found that the spectra can be naturally explained by an ionizing-dominate NEI model. The similar results were confirmed in many SNRs so that the observed plasma in SNRs had been considered to be in the transition from ionizing plasma (IP) to CIE plasma as illustrated in Figure 3.9.

3.1.3 Over-ionized Recombining Plasma

Discovery of RPs

The standard scenario from IP to CIE plasma was questioned by Kawasaki et al. (2002, 2005). Analyzing *ASCA* data of IC 443 and W49B, they claimed that the measured Lyα-to-Heα line intensity ratios of S, Ca, and Ar are higher than those expected from CIE models with the electron temperatures determined by the bremsstrahlung continua (Figure 3.10). However, based on subsequent observations of these SNRs with *XMM-Newton*, Miceli et al. (2006) and Troja et al. (2008) showed that the line intensity ratios can be reproduced by multi CIE components, and claimed that the over-ionization is only marginal. In principle, arbitrary Lyα-to-Heα ratio can be reproduced by a superposition of multiple-temperature CIE plasmas. Therefore, other evidence were needed to conclude whether the over-ionization is real or not.

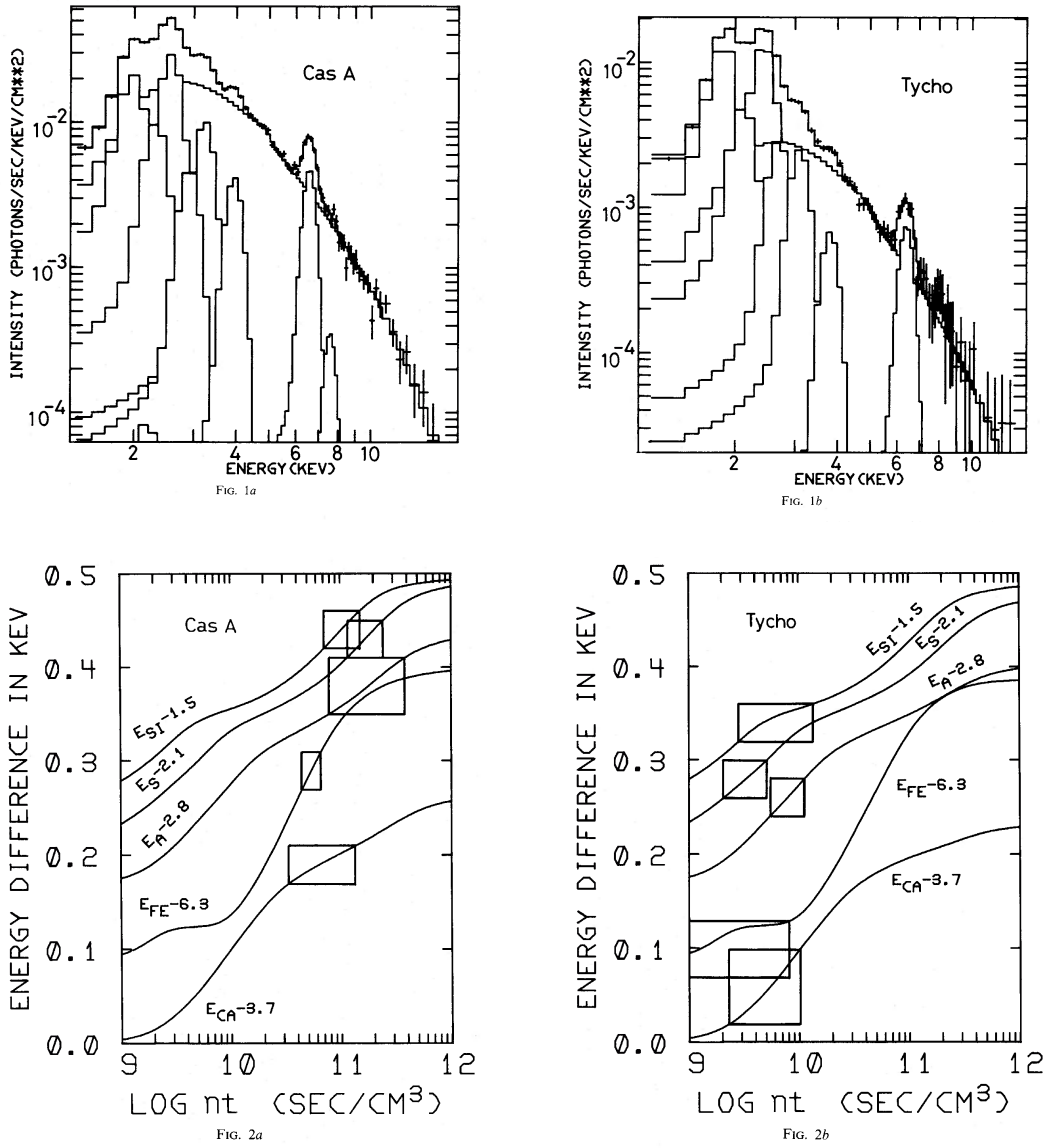

Figure 3.8: X-ray spectra for (upper left) Cas A and (upper right) Tycho's SNR obtained with *Tenma*. The black curves show the best-fit models. Deviations of the mean energies of Si, S, Ar, Ca, Fe Kα lines are constrained in the spectral fitting from that expected in a CIE model for (bottom left) Cas A and (bottom right) Tycho's SNR. The horizontal axis represents the ionization time scale $n_e t$ in Equation 3.10. The black boxes and curves show the constrained ranges with the 90 % confidence levels and IP models, respectively. (taken from Tsunemi et al., 1986)

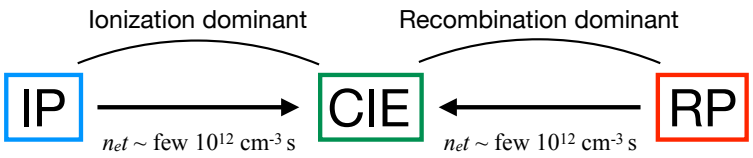

Figure 3.9: Ionization states of plasma in SNR.

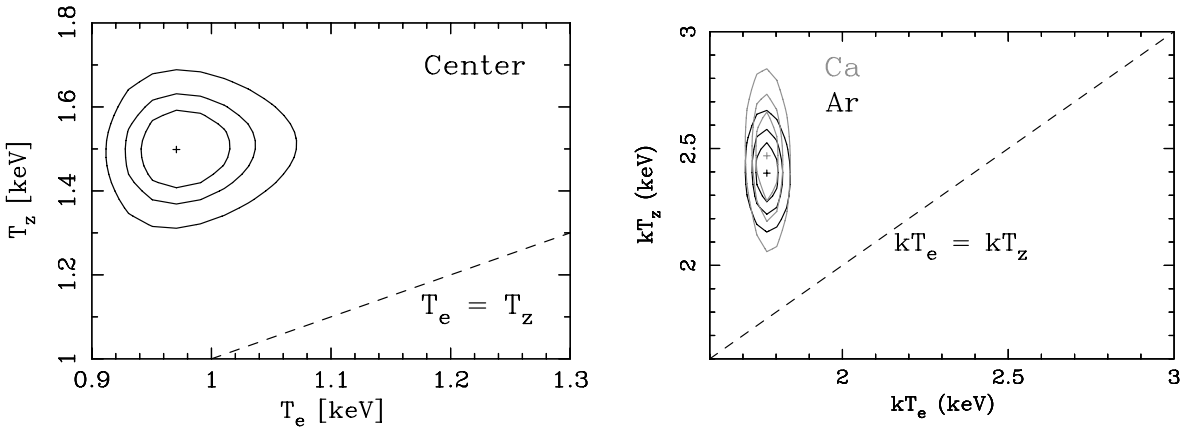

Figure 3.10: Confidence contours in kT_e-kT_z space for (left) IC 443 and (right) W49B (Kawasaki et al., 2002, 2005). The black curves show the 1 σ, 90 %, and 99 % confidence levels. The ionization temperature kT_z is equal to the electron temperature kT_e if the Lyα-to-Heα line intensity ratio described in plasmas with the kT_z is equal to that in CIE plasmas. For instance, IPs have a smaller value of kT_z than kT_e, and the CIE plasmas have the same value of kT_z than kT_e. The dashed line corresponds to the relation between kT_e and kT_z in CIE plasmas.

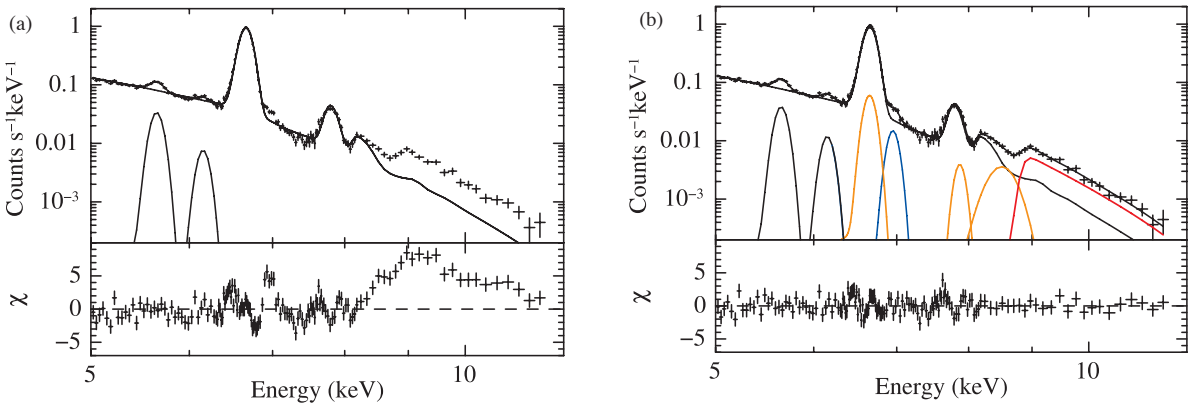

Figure 3.11: (a) W49B spectra obtained with *Suzaku*. Black line represents the best-fit CIE model with additional Cr and Mn Kα lines. (b) Same as the left figure but plotted with the RRC (red), recombination lines (orange), and Fe Lyα line (blue) line. (taken from Ozawa et al., 2009).

A breakthroughs concerning studies of the over-ionization was brought by detections of strong RRCs with Suzaku observations of W49B (Ozawa et al., 2009) and IC 443 (Yamaguchi et al., 2009). Figure 3.11 shows the *Suzaku* spectra of W49B overlaid with (left) a CIE model, and (right) the CIE model and additional He-like Fe RRC and line components. We can see that a CIE plasma is not able to reproduce the spectra, leaving the characteristic residuals around the energies of the Fe RRC. Even with multiple-temperature CIE plasmas, the overall spectrum cannot be reproduced well. Currently, this plasma is called over-ionized recombining plasmas (RPs).

Recent Works concerning Formation Process of RPs

Recent X-ray studies have revealed RPs in a dozen of SNRs. All of them are classified as MM SNRs (e.g., Uchida et al., 2015) as discussed in Section 2.2.3. Most of the MM-SNRs are known to be interacting with molecular clouds. These facts imply that the presence of RPs is somewhat common among MM SNRs, and that shock-cloud interactions seem to be related to the origin of RPs. Although some scenarios (e.g., Itoh & Masai, 1989; Kawasaki et al., 2002, 2005) are proposed to explain the RPs, the formation process of the RP has been not fully understood yet.

The physical origin of RPs have been studied based on spatial variations of plasma parameters (e.g., kT_e and $n_e t$), and their comparison with distribution of ambient gas. Some authors such as Matsumura et al. (2017b) and Okon et al. (2018) reported spatial correlations between the electron temperature kT_e of SNR plasmas in IC 443 and W28 and surrounding dense molecular clouds, respectively. Matsumura et al. (2017a) and Katsuragawa et al. (2018) also reported the same kT_e tendency in G166+4.3 and CTB 1, respectively. In Figures 3.12 and 3.13, we show the overview of W28 and the kT_e obtained with *Suzaku* data, respectively. The electron temperature kT_e decreases in the region where the shocks in W28 interact with clouds. The results can be explained by a rapidly cooling due to thermal conduction with the clouds, suggesting the formation of the RPs as the thermal conduction scenario originally proposed by Kawasaki et al. (2002) and Kawasaki et al. (2005).

Itoh & Masai (1989) and Shimizu et al. (2012) predicted another scenario concerning the formation of RPs, the so-called rarefaction scenario, by using numerical simulations. In this scenario, rapid adiabatic expansion in the SNRs is responsible for the overionization. Some authors, e.g., Miceli et al. (2010), Lopez et al. (2013), Greco et al. (2018), and Sezer et al. (2019), indeed claimed that their X-ray spectroscopy results support the scenario. The clearest evidence was presented by Yamaguchi et al. (2018), who analyzed *NuSTAR* data of W49B and performed spatially resolved spectroscopy, focusing on the Fe RRC. They found a clear correlation between the values of kT_e and $n_e t$ derived for each region (Figure 3.14). The result suggests lower electron temperatures are achieved in the lower density regions, qualitatively consistent with a rapid adiabatic expansion scenario as an origin of the overionization.

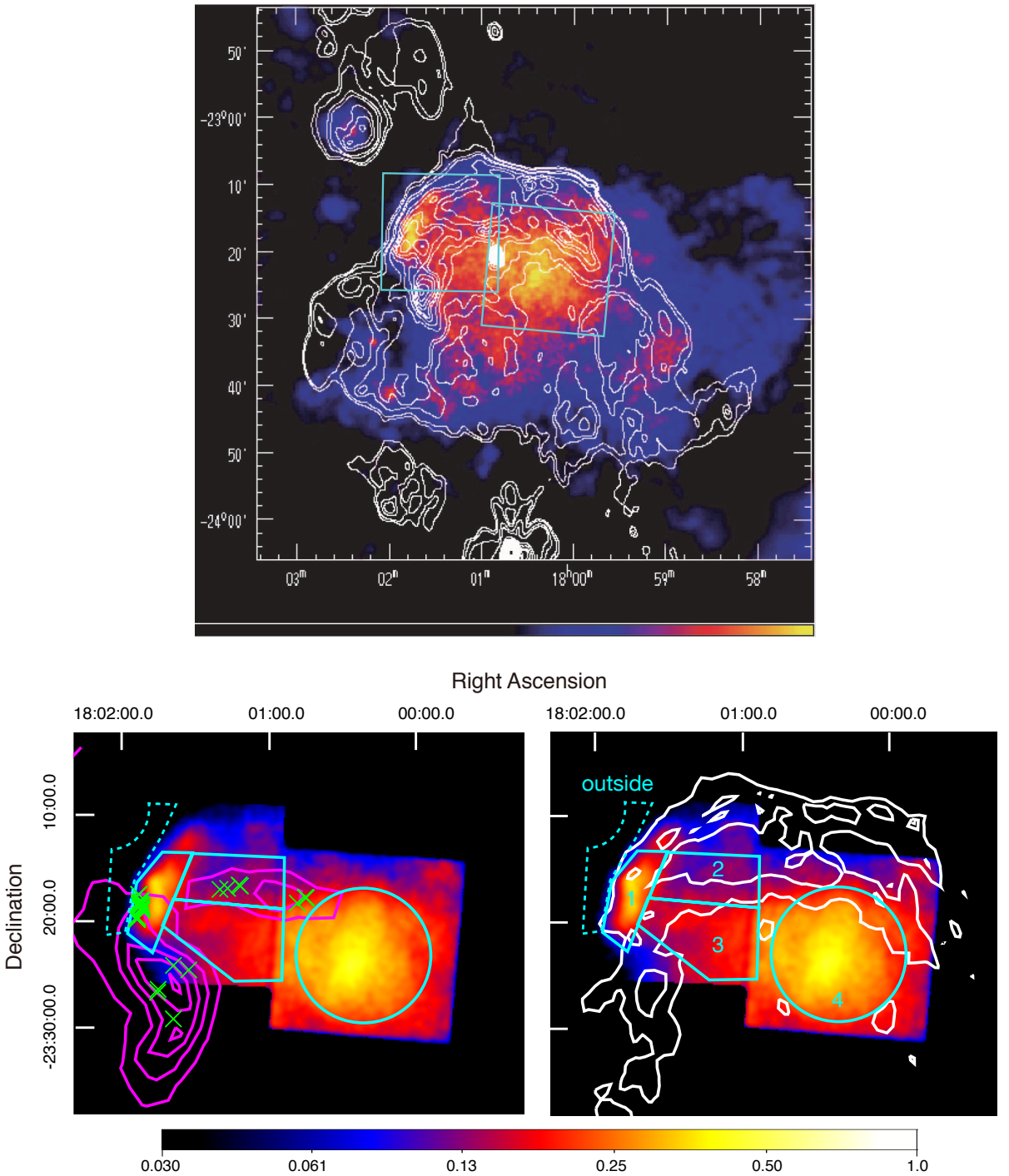

Figure 3.12: (upper) 0.5–2.4 keV X-ray image of the entire W28 taken with *ROSAT* overlaid the 328 MHz radio contours (Rho & Borkowski, 2002). The cyan boxes correspond to two *Suzaku* fields. (bottom left) Images of W28 in the energy band of 0.65–4.0 keV obtained by *Suzaku*. The cyan solid and dash lines denote the source and background regions, respectively. The white contours indicate the radio 325 MHz emission. The magenta contours and green crosses show the spatial distribution of the ^{12}CO $(J = 2 - 1)$ line emission and the locations of 1720 MHz OH maser emission, respectively. These emissions are interpreted as evidence for shock-cloud interactions. (bottom right) Same as the bottom right panel but overlaid the white contours indicating the radio 325 MHz emission (Okon et al., 2018).

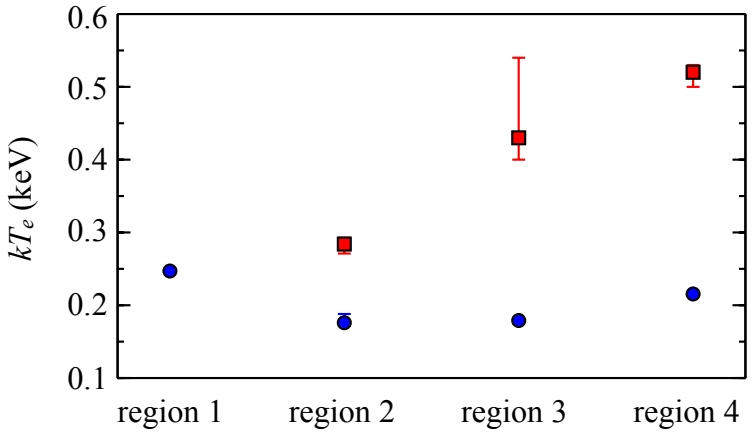

Figure 3.13: Electron temperature kT_e of two RP components obtained for the four source regions of W28 in Figure 3.12. The red and blue points represent kT_e for the higher-kT_e RPs and those for the lower-kT_e RPs, respectively (Okon et al., 2018). In the region 1, the hot component is not observed.

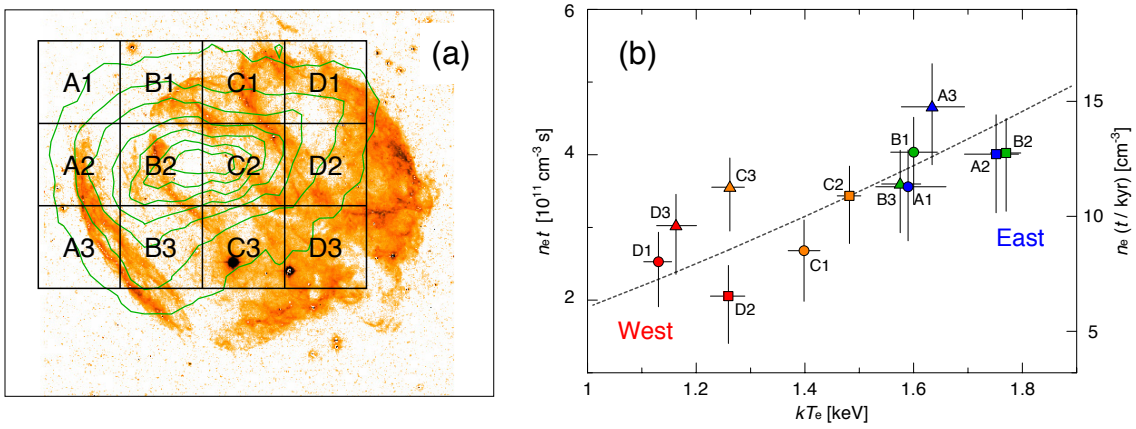

Figure 3.14: (a) Image of 1.64 μm [FeII] line around W44 indicating an ambient gas distribution. The green contours are the exposure corrected Fe Heα flux map. The boxes are sub-regions used in the X-ray spatial spectroscopy. (b) Relationship between kT_e and $n_e t$. The region names labeled near the data points correspond to those given in panel (a). The dashed line is a power-law function with an index of 1.5 which is derived from the relation $TV^{2/3} = \text{const}$ between the gas volume V and temperature kT_e expected in an adiabatic process of an ideal gas. (taken from Yamaguchi et al., 2018).

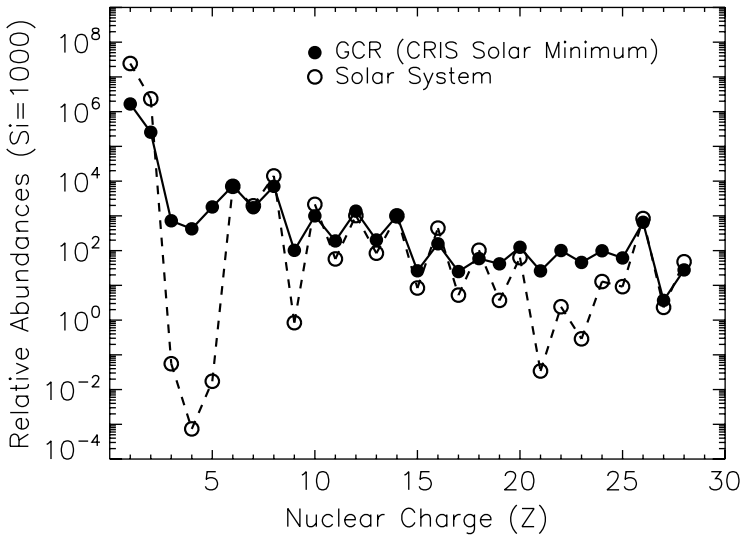

Figure 3.15: Composition of CRs and the solar abundance as a function of nuclear charge (George et al., 2009).

3.2 Particle Acceleration in SNRs

It is widely believed that particles accelerated in SNRs constitute a significant fraction of cosmic rays in our Galaxy. Cosmic rays (CRs) are one of the major components of the interstellar space in terms of energy density, and hence play an important role for the structure and evolution of our Galaxy. This section gives the relation between SNRs and cosmic rays, the diffusive shock acceleration theory as the most plausible mechanism for cosmic-ray production, and a summery of evidence for particle acceleration in SNRs.

3.2.1 SNRs as Galactic Cosmic Ray Sources

CRs are high energy particles in the space. The origin and the acceleration mechanism have been the important issues in physics since the discovery of them by Victor F. Hess in 1912. Currently, arriving cosmic rays are known to consist of mainly protons and ionized atomic nuclei (~ 98 %), as shown in Figure 3.15, and the rest are electrons and positrons. A noteworthy point is that the energy spectra dN/dE presented in Figure 3.16, are represented by an almost featureless nonthermal distribution over a very wide range of energies, from below $\sim 10^9$ eV up to $\sim 10^{20}$ eV. The spectra can be described by a power-law function as

$$dN/dE \propto \begin{cases} E^{-2.7} & (E \gtrsim 3 \times 10^{15}\ \mathrm{eV}) \\ E^{-3.1} & (E \lesssim 3 \times 10^{15}\ \mathrm{eV}), \end{cases} \tag{3.12}$$

where E is the kinetic energy per nucleon. The steepening at an energy of around $\sim 3 \times 10^{15}$ eV is called "knee".

CRs up to the knee are thought to be accelerated in astrophysical objects in our Galaxy. The gyro radii of such particles actually are much smaller than the thickness of our Galaxy so that they should be confined in our Galaxy. Therefore, CRs up to the knee energy are often called Galactic Cosmic Rays (GCRs). Currently, SNRs are believed to be the most probable

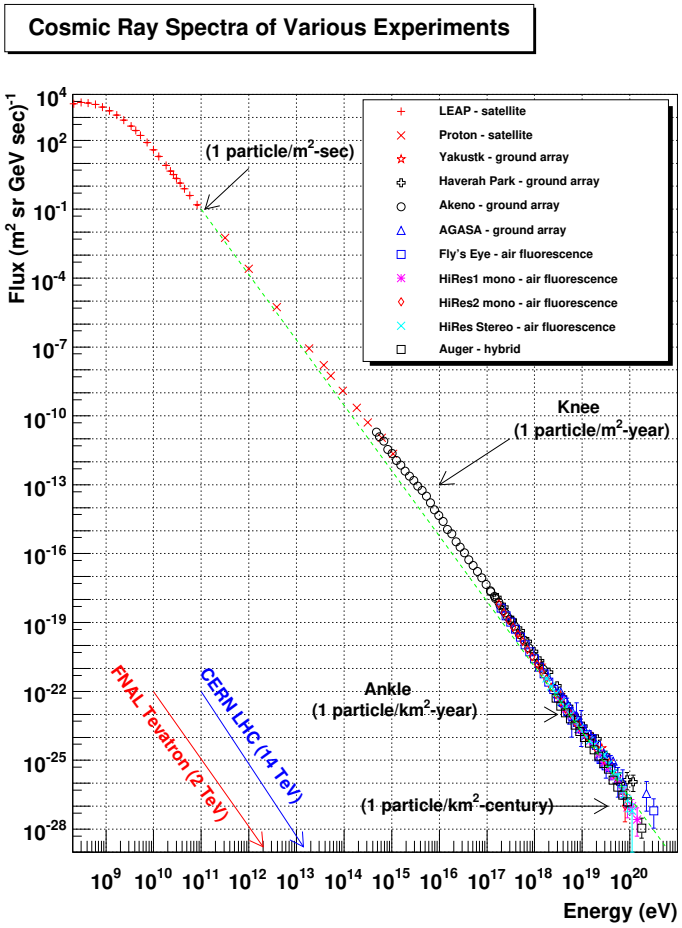

Figure 3.16: Energy spectra from 10^8 eV to 10^{21} eV of CRs.
<https://www.physics.utah.edu/~whanlon/spectrum.html>

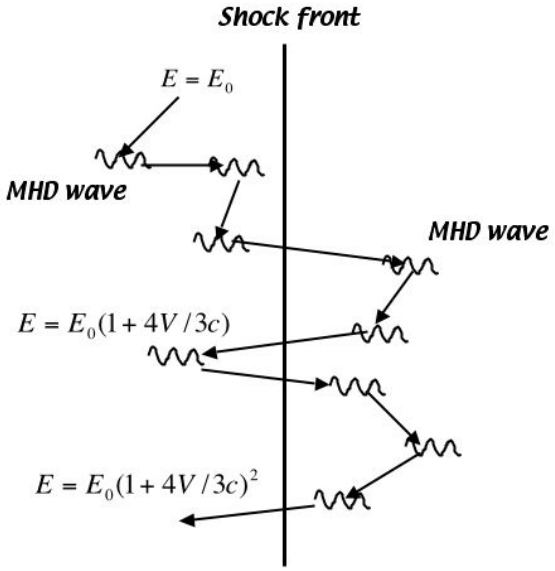

Figure 3.17: Schematic drawing of the scattering of particles in the DSA mechanism.

candidates for the acceleration sites of GCRs (Ginzburg & Syrovatskii, 1964) for the following two reasons.

One reason is that SNe are almost the only known astrophysical objects capable of providing kinetic energy needed to explain the injection rate of GCRs. The injection rate $L_{\rm CR}$ can be estimated as follows,

$$L_{\rm CR} \sim \frac{\epsilon_{\rm CR} V_{\rm Gal}}{\tau_{\rm CR}} \sim 5 \times 10^{41} \quad {\rm erg\,s^{-1}}, \tag{3.13}$$

where $\epsilon_{\rm CR}$ is the observed energy density (~ 1 eV cm^{-3}), $V_{\rm Gal}$ is the confinement volume of GCRs ($\sim 3 \times 10^{67}$ cm^3) taken to be the disk with a radius of 10 kpc and a thickness of 1 kpc, and $\tau_{\rm CR}$ ($\sim 3 \times 10^{14}$ s) is the resident timescale of GCRs within the confinement volume estimated by abundance of radioisotope (^{10}B) in GCRs. One SN event typically releases the kinetic energy of $\sim 10^{51}$ erg, and is considered to occur per ~ 30 yr in our Galaxy. Therefore, we can see that the energy budget for the production of GCRs can be satisfied if about 10 % of the total energy released in the SNe is somehow transferred to particle acceleration in SNRs.

The other reason is that SNRs can naturally explain the spectral property of GCRs. As discussed in Section 2.2.3, SNRs have extended radio morphologies formed by synchrotron emissions. The radio spectra of SNRs, especially shell type SNRs, are described by a power law distribution, $\epsilon \cdot dn_\gamma/dE \propto E^{-0.5}$, indicating the presence of relativistic electrons in a GeV order whose population is represented by $dN/dE \propto E^{-2}$. Here, the generation spectrum of GCRs at the acceleration sites should be harder and close to 2 because a part of the accelerated particles are escaping from the confinement volume during their propagation. Therefore, we can naturally explain the characteristic energy spectra of GCRs assuming SNRs are GCRs sources.

3.2.2 Diffusive Shock Acceleration Theory

Fermi (1949) first proposed an acceleration mechanism where charged particles gain energy in a stochastic manner via scattering by magnetized clouds in the ISM. The acceleration mechanism is often called the second-order Fermi acceleration mechanism. Bell (1978) and Blandford

& Ostriker (1978) developed the Fermi's idea into Diffusive Shock Acceleration (DSA) theory, which is widely accepted as the standard mechanism of particle acceleration in SNRs. Here, we summarize the DSA theory and explain the expected energy spectrum.

Figure 3.17 presents a schematic drawing of particle acceleration in the DSA theory. In this theory, charged particles undergo being repeatedly reflected by Alfvén waves in upstream and downstream of the shock waves. When a particle with energy E moves into the downstream from upstream, its energy E' in downstream can be derived by the Lorentz transformation,

$$E' = \gamma(E + Vp\cos\theta). \tag{3.14}$$

Here, the parameter V represents the difference of the shock speeds $v_{\rm u} - v_{\rm d}$ in upstream and in down stream as shown in Figure 2.6, p is the momentum of the particle, and θ is the angle between the moving direction of the particle and the axis perpendicular to the shock. Assuming the shock is non-relativistic, $V \sim 1$, and the particle is relativistic, $E \sim cp$, we can obtain the energy gain δE as

$$\delta E = E' - E = E\frac{V}{c}\cos\theta. \tag{3.15}$$

The average energy gain is calculated as

$$< \delta E >= E\frac{V}{c}\int_0^{\pi/2} 2\sin\theta\cos\theta\, d\theta = \frac{2V}{3c}E. \tag{3.16}$$

The particle again gain the same fractional energy increase as before, $< \delta E >= (2/3)(V/c)E$, when it moves into the upstream from downstream. Therefore, particles gain the average fractional energy, $\delta E/E = (4/3)(V/c)$, through one round trip across the shock (see Bell, 1978). Considering the energy increase is very tiny, $\delta E/E \ll 1$, we can give the the average energy E_n after n-times round trips,

$$E_n = E_0\left(1 + \frac{4V}{3c}\right)^n \sim E_0\exp\left(\frac{4V}{3c}n\right), \tag{3.17}$$

where E_0 is the energy of the particles before the scattering.

In the downstream, a part of accelerated particles escape by their convective motion. The number of particles crossing the shock is $Nc/4$, where N is the number density of the particles. The number of escaping particles by the convective motion is $n v_{\rm d}$. Therefore, we can obtain the probability of the particles escaping as $(N v_{\rm d})/(Nc/4) = 4v_{\rm d}/c$. The probability that the particles remain in the acceleration site just after n round trips is,

$$P_n = \left(1 - \frac{4v_{\rm d}}{c}\right)^n \sim \exp\left(-\frac{4v_{\rm d}}{c}n\right). \tag{3.18}$$

We can rewrite Equation 3.18 as $P_n = (E_{\rm n}/E_0)^{-3v_d/V}$, using Equations 3.17. With a relation between the differential energy spectrum dN/dE of the particles, and E_n and P_n, $P_n \propto \int_{E_n}^{\infty}\frac{dN}{dE}dE$, we can derive dN/dE as follows,

$$\frac{dN}{dE} \propto E^{-s}, \quad s = \frac{v_{\rm u}/v_{\rm d} + 2}{v_{\rm u}/v_{\rm d} - 1}. \tag{3.19}$$

For strong shocks in a monoatomic gas ($v_{\rm u}/v_{\rm d}$ = 4, see Equation 2.17), accelerated particles obey a power law distribution $dN/dE \propto E^{-2}$. The index expected in DSA is consistent with the ones obtained in the observations of radio synchrotron in SNRs in Section 3.2.3.

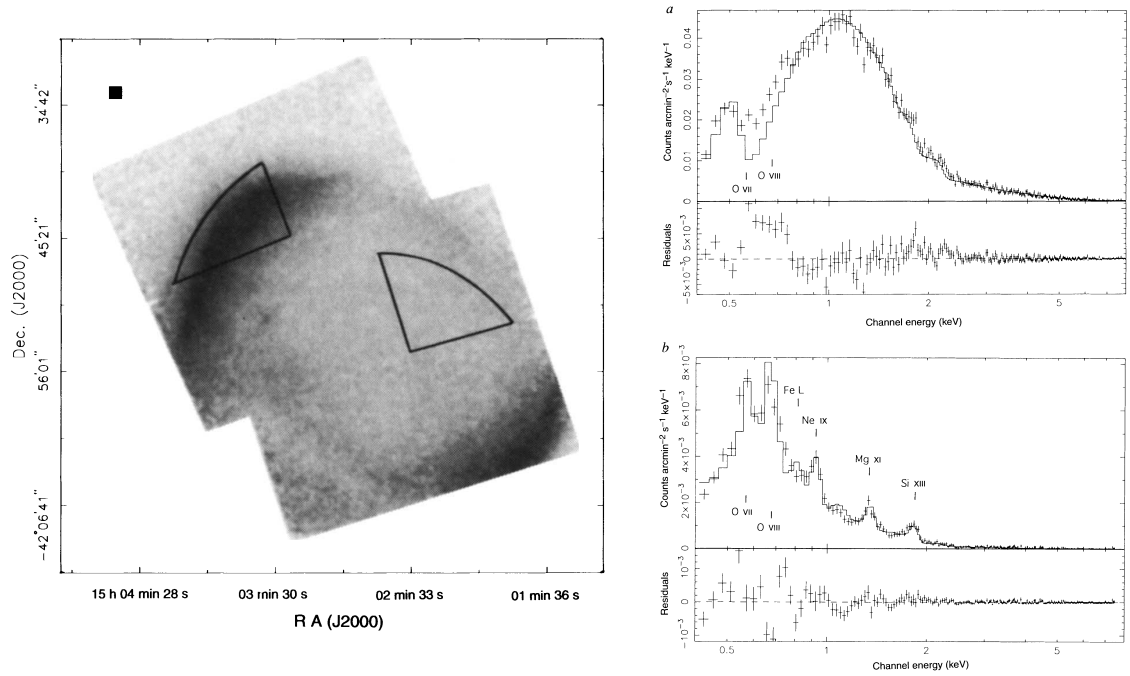

Figure 3.18: (left) X-ray images of SN 1006 in the energy band of 0.4–8.0 keV taken with *ASCA*. (upper right) Spectrum from the bright northeast rim. The solid line shows the best-fit model. (bottom right) Same as the upper right panel but for the interior region. (taken from Koyama et al., 1995).

3.2.3 Nonthermal Emissions from Accelerated Relativistic Particles

Particle acceleration in SNRs has been widely studied through detection of nonthermal emissions from accelerated particles. Here, we summarize radiation mechanisms and previous works concerning their detection of them in SNRs.

Synchrotron Radiation

Synchrotron radiation, which is from electrons accelerated in the magnetic field by Lorentz force, is a powerful tool to probe high energy electrons. The synchrotron radiation power per unit frequency from one relativistic electron is given by (Rybicki & Lightman, 1979)

$$P(\omega) = \frac{\sqrt{3}\,e^3 B \sin\theta}{2\pi\, m_e\, c^2} F(\omega/\omega_c). \tag{3.20}$$

Here, θ is the pitch angle, ω_c is the characteristic frequency described as

$$\omega_c = \frac{3\gamma^2\, e B \sin\theta}{2\, m_e\, c}, \tag{3.21}$$

and the function $F(x)$ gives the spectral energy distribution from a single electron expressed as

$$F(x) = x \int_x^\infty K_{5/3}(\xi) d\xi, \tag{3.22}$$

with a modified Bessel function $K_{5/3}$. The Function $F(x)$ has a peak at ~ 0.29 so that $P(\omega)$ has also a peak at $\omega \sim 0.29\ \omega_c$. The photon energy at the peak frequency $\sim 0.29\,\omega_c$ can be regarded as the average synchrotron photon energy from one electron, and is approximately written as

$$\epsilon \sim 3.3 \left(\frac{B}{10\ \mu\mathrm{G}} \right) \left(\frac{E_e}{100\ \mathrm{TeV}} \right)^2 \ \mathrm{keV}, \tag{3.23}$$

where E_e is the electron energy. We assumed the average angle of $\overline{\sin\theta}$ $(= \sqrt{\langle \sin^2\theta \rangle} = \sqrt{2/3})$. By integrating of Equation 3.20 over frequency, we calculate total power as

$$P_{\mathrm{sync}} = \frac{4}{3} \sigma_{\mathrm{T}}\, c\, \beta^2\, \gamma^2\, U_{\mathrm{B}}, \tag{3.24}$$

where U_B $(= B^2/8\pi)$ is the energy density of the magnetic field. We can derive the synchrotron spectrum from electrons with any energy distribution by using the spectrum from single-electron. Assuming the electrons obeying a power law distribution $dN/dE \propto E^{-s}$, the behavior of the synchrotron energy spectra $\epsilon \cdot dn_\gamma/d\epsilon$ can be approximately described as,

$$\epsilon \cdot dn_\gamma/d\epsilon \propto \int P(\omega) dN/dE dE \propto B^{(s+1)/2}\, \epsilon^{-(s-1)/2}, \quad \alpha = -(s-1)/2. \tag{3.25}$$

Koyama et al. (1995) discovered synchrotron X-ray emissions from SN 1006 with the *ASCA* X-ray observatory. They found that the rim of the remnant is dominated by the synchrotron component as shown in Figure 3.18, and concluded that electrons are accelerated up to $\sim$ 100 TeV at the shock waves (see Equation 3.23). In several other SNRs, such as RX J1713.7−3946 (Koyama et al., 1997) and RX J0852.0−4622 (Slane et al., 2001), the synchrotron X-ray emissions have also been detected. Recently, some authors (e.g., Uchiyama et al., 2007; Tsuji & Uchiyama, 2016) have studied key topics in particle accelerations such as an amplification of the magnetic fields in the shock waves and measurements of shock velocity, through the spatially resolved spectroscopy of synchrotron X-rays in SNRs.

Inverse Compton Scattering

Another piece of evidence for accelerated electrons in SNRs is gamma-ray emissions emitted via inverse Compton up-scattering. In this process, the low energy seed photons are scattered by high energy electrons to higher energies. Generally, in the case of SNRs, the Cosmic Microwave Background (CMB) photons are a dominant as seed photons. The total power of the gamma-rays emitted from a single electron, in the Thomson regime, is given by,

$$P_{\mathrm{IC}} = \frac{4}{3}\, \sigma_{\mathrm{T}}\, c\, \beta^2\, \gamma^2\, U_{\mathrm{CMB}}, \tag{3.26}$$

where σ_{T} is the Thomson cross section and $U_{\mathrm{CMB}} (= n_{\mathrm{CMB}}\, \overline{\epsilon_{\mathrm{CMB}}})$ is the the average energy density of the CMB photons. The n_{CMB} and $\overline{\epsilon_{\mathrm{CMB}}}$ are the number density of the CMB photons and the average energy per one CMB photon, respectively. Dividing Equation 3.24 by Equation 3.26, we obtain

$$\frac{P_{\mathrm{sync}}}{P_{\mathrm{IC}}} = \frac{U_{\mathrm{B}}}{U_{\mathrm{CMB}}}. \tag{3.27}$$

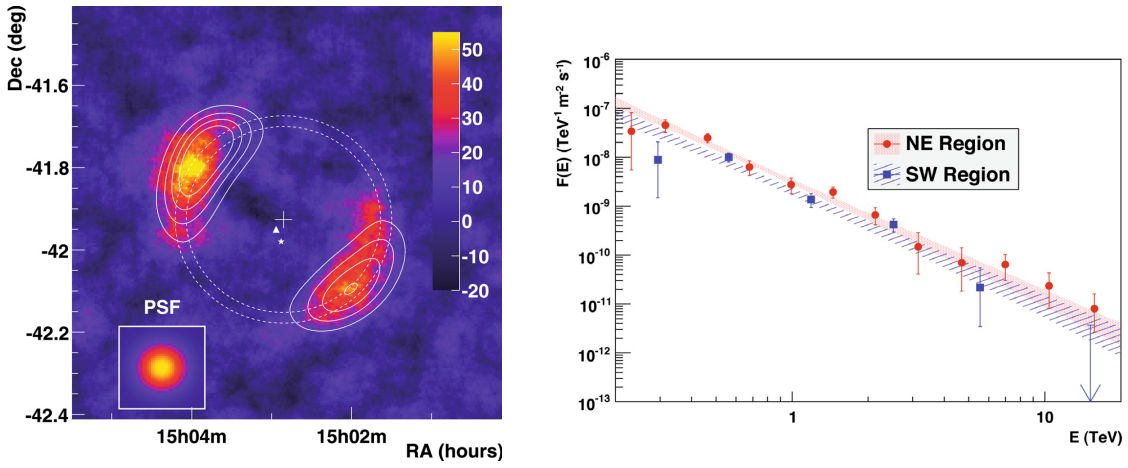

Figure 3.19: (left) H.E.S.S. gamma-ray map of SN 1006. The white solid contours show the X-ray image in the 2.0-4.5 keV energy range. (right) Energy spectra of SN 1006 extracted from the northeastern and southwestern shells. The shaded bands correspond to the range of the power-law fit with the 1 σ confidential levels. (taken from Acero et al., 2010)

This equation means that, if the energy density of seed photons are well known such as the CMB, we can probe the strength of the magnetic field with the flux ratio of synchrotron emission to inverse Compton emission. We can derive the average energy ϵ of the scattered photon as

$$\epsilon = \frac{4}{3}\beta^2\gamma^2\overline{\epsilon_{\rm CMB}}. \tag{3.28}$$

Here, we obtaine this equation dividing Equation 3.26 by the number of photons scattered per unit time is $c\,\sigma_{\rm T}\,n_{\rm CMB}$. For instance, the scattered photon energy is about 10 GeV when electrons of 5 TeV ($\beta \sim 1$, $\gamma \sim 10^7$) scatter the CMB photons ($\overline{\epsilon_{\rm CMB}} \sim 2.73$ K $\sim 2.3\times10^{-4}$ eV).

The gamma-ray spectra of the inverse Compton emission were calculated by some authors (e.g., Jones, 1968; Blumenthal & Gould, 1970). We can calculate the gamma-ray spectra $dn_\gamma/d\epsilon$ as follows,

$$dn_\gamma/d\epsilon \propto \int d\epsilon_0 \frac{dn_0}{d\epsilon_0}\int d\gamma \frac{dN}{d\gamma}\frac{d^2n_\gamma}{dt\,d\epsilon}, \tag{3.29}$$

where $dn_0/d\epsilon_0$ is the differential density spectrum of the seed photons, $dN/d\gamma$ is the differential spectrum of electrons, and $d^2n_\gamma/dt\,d\epsilon$ is the differential production rate of scattered photons. Assuming electrons are relativistic, Jones (1968) gave $d^2n_\gamma/dt\,d\epsilon$ as

$$\frac{d^2n_\gamma}{dt\,d\epsilon} = \frac{2\pi r_0{}^2 c}{\alpha_0\gamma^2}\left[2q\ln q + (1+2q)(1-q) + \frac{1}{2}\frac{(4\alpha_0\gamma q)^2}{1+4\alpha_0\gamma q}\right], \tag{3.30}$$

where r_0 is the classical electron radius, $q = \alpha/4\alpha_0\gamma^2(1-\alpha\gamma)$, $\alpha = \epsilon/m_e c^2$, and $\alpha_0 = \epsilon_0/m_e c^2$. With Equations 3.29 and 3.30, Blumenthal & Gould (1970) calculated the asymptotic behavior of the energy spectra $\epsilon\cdot dn_\gamma/d\epsilon$ of gamma-rays from nonthermal electors, $dN/dE \propto E^{-s}$, as $\propto \epsilon^{(-s+1)/2}$. Here, the seed photons are assumed to be the CMB photons.

Recently, the observations of high energy phenomena in the GeV–TeV bands was enabled by the advent of gamma-ray telescopes such as Large Area Telescope on Fermi Gamma-ray Space Telescope (*Fermi*) and the high energy stereoscopic system (H.E.S.S.) of Cherenkov Telescopes.

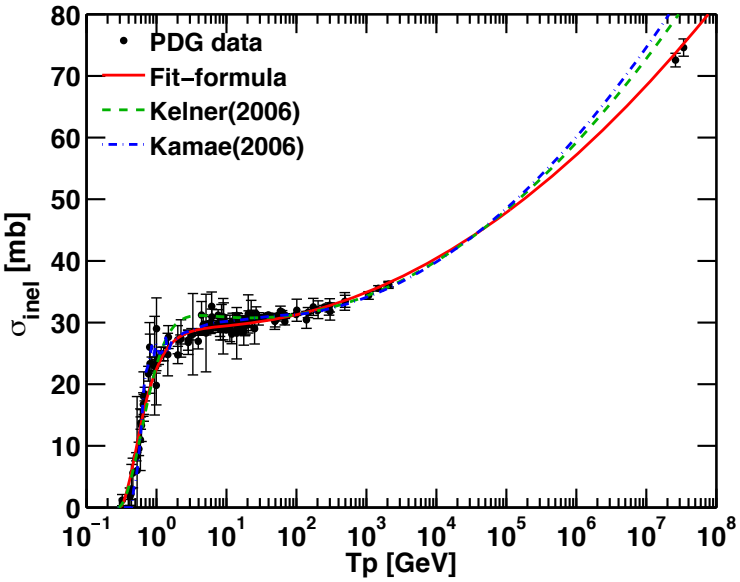

Figure 3.20: Cross section for inelastic proton-proton interaction as a function of the proton kinetic energy in the laboratory system. (taken from Kafexhiu et al., 2014)

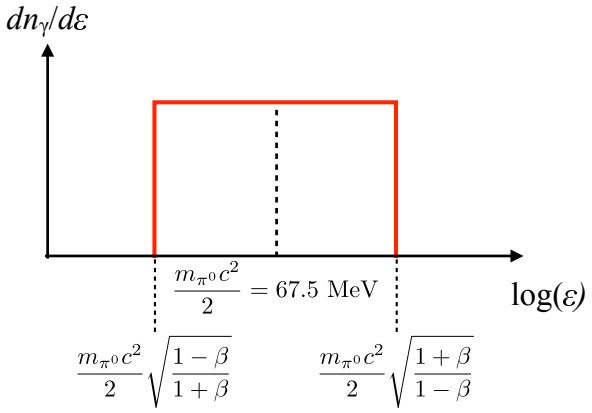

Figure 3.21: Spectrum of gamma-ray generated by π^0-decay.

Figure 3.19 presents a gamma-ray map of SN 1006 with H.E.S.S. (Acero et al., 2010). The map shows strongly spatially correlations between the gamma-ray emissions and the shock waves, and the synchrotron X-rays. These X-ray and gamma-ray observations established the picture that electrons can be accelerated to energies of $\sim$ TeV at shock waves in SNRs.

π^0 decay gamma-rays

A direct signature of high energy protons, which are major components of GCRs, is provided by gamma-ray emissions through the decay of π^0-mesons generated by inelastic collisions between protons in GCRs and that in the ISM as follows,

$$p\,(\text{GCRs}) + p\,(\text{ISM}) \rightarrow p + p + \pi^{+,-,0}, \tag{3.31}$$

$$\pi^0 \rightarrow 2\gamma. \tag{3.32}$$

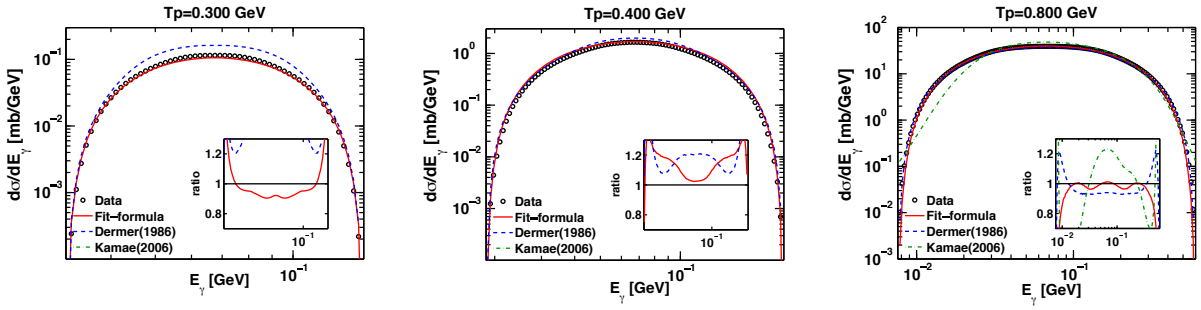

Figure 3.22: π^0-decay spectra for different proton collision energies T_p (left: $T_p = 0.3$ GeV; center: $T_p = 0.4$ GeV; right: $T_p = 0.8$ GeV).

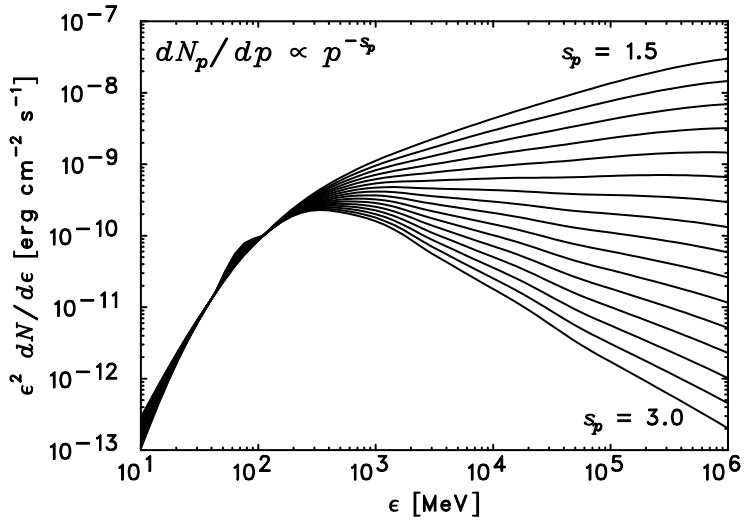

Figure 3.23: Gamma-ray spectra of decays of π^0-mesons by nonthermal protons ($dN/dE \propto E^{-s}$). If protons are relativistic, the protons distribution can be written as $dN/dp \propto p^{-s_p}$. The index s_p is equal to s. (Figure from Dr. Tanaka)

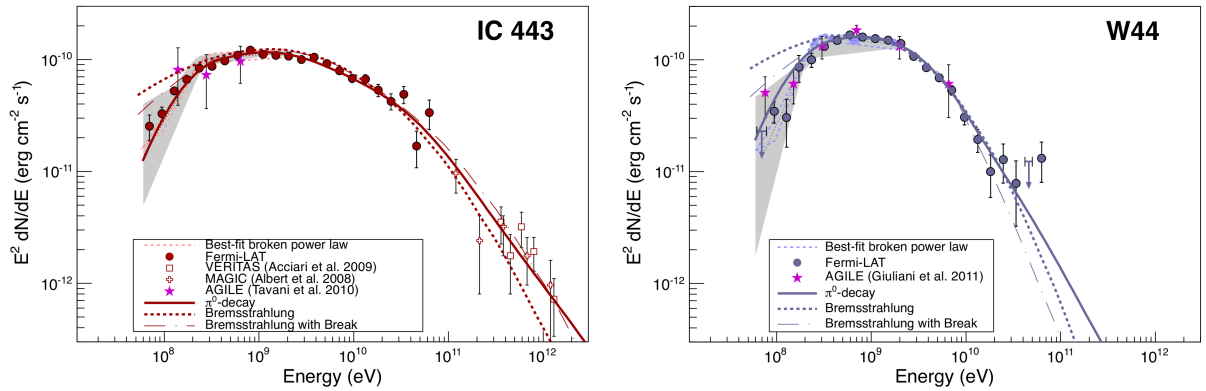

Figure 3.24: (left) GeV–TeV data of IC 443 taken from *Fermi*, *VERITAS*, *MAGIC*, and *AGILE*. Solid line denotes the best-fit curve with a π^0-decay model. Dashed, dash-dotted lines show the the best-fit models with a bremsstrahlung model, a bremsstrahlung model with an energy break, respectively. (right) Same as but for W44. (taken from Ackermann et al., 2013).

In the rest system of the produced pions, they decay with the mean lifetime 8.4×10^{-17} s, and emit two gamma-rays with the energy of a half of the π^0 rest mass ($m_\pi c^2/2 = 67.5$ MeV).

In Figure 3.21, we show the gamma-ray spectrum $dn_\gamma/d\epsilon$ expected through the decay of mono-energetic π^0-mesons. The gamma-rays are symmetrically distributed around 67.5 MeV ($= m_\pi c^2/2$) in the log energy scale (Stecker, 1971), and show a flat spectrum. The behavior of the gamma-ray spectrum can be understood as follows. We can derive energy ϵ of observed gamma-rays using the Lorentz transformation from the rest frame of π^0-mesons to the observer frame,

$$\epsilon = \gamma(\epsilon^* + v p^* \cos\theta^*), \tag{3.33}$$

where γ and v are gamma factor and velocity of π^0-mesons in the observer frame, respectively, and $\epsilon^* (= m_{\pi^0} c^2/2)$, p^* and θ^* are energy, momentum of emitted gamma rays, and the angle between the observer and the moving direction of π^0-mesons, in the in rest frame, respectively. The maximum $\epsilon_{\rm max} = m_\pi c^2 \sqrt{1+\beta}/2\sqrt{1-\beta}$ and minimum $\epsilon_{\rm min} = m_\pi c^2 \sqrt{1-\beta}/2\sqrt{1+\beta}$ energies in Figure 3.21 correspond to the cases in Equation 3.33 with $\theta^* = 0^\circ$ and 180°, respectively. We can describe a helpful relation between the maximum and minimum energies,

$$\frac{1}{2}(\log(\epsilon_{\rm max}) + \log(\epsilon_{\rm max})) = \log\left(\frac{1}{2} m_{\pi^0} c^2\right). \tag{3.34}$$

Equation 3.34 means that the center of the interval is half of the pion mass in log-log scale. The isotropic distribution $dn_\gamma/d\Omega^*$ of emitted photons in the π^0 rest frame can described as

$$\frac{dn_\gamma}{d\Omega^*} = \frac{1}{2\pi}\frac{dn_\gamma}{d(\cos\theta^*)} = \text{const.} \tag{3.35}$$

With this equation and a variation of Equation 3.33, $d\epsilon = d(\cos\theta^*)$, we can see that gamma-ray spectrum $dn_\gamma/d\epsilon$ is constant. Therefore, the gamma-ray emissions have a flat spectrum.

Figure 3.22 shows π^0-decay spectra for different proton collision energies. The spectrum is also symmetric because the spectrum is a superposition of the spectra of decays of mono-energetic π^0-mesons. In Figure 3.23, we present the $\nu F\nu$ spectra ($\epsilon^2 \cdot dn_\gamma/d\epsilon$) of gamma-rays by the protons with $dN/dE \propto E^{-s}$. The spectra above ~ 200 MeV are power law with indices which are the same as that of the proton distribution. On the other hand, the spectra below ~ 200 MeV do not depend on the proton distributions, and shows the characteristic "break" structures. The behavior in the low-energy band reflects the rapid increasing of the proton-proton inelastic cross section around 200 MeV–1 GeV (Figure 3.20).

Although the promising channel to prove accelerated protons have been considered to be the gamma-ray emissions through the π^0-decay, the identification of the gamma rays has been difficult. Gamma-rays via π^0-decay process show power law spectra in the energy range of above ~ 1 GeV. However, for example, as discussed in the section of Inverse Compton Scattering, the gamma-rays via this process can also represent the same featureless spectra. Ackermann et al. (2013) focused on the characteristic break signature below ~ 200 MeV only in the π^0-decay spectrum, and succeed in detecting the structures in spectra of W44 and IC 443 with *Fermi*. Figure 3.24 show the GeV–TeV spectra overlaid with π^0-decay and bremsstrahlung models. One can see the spectral breaks in the energy band of below 300 MeV.

3.2.4 Exploration of Sub-relativistic Particles

Sub-relativistic particles are one of the important components in particle acceleration because information on such particles are key to estimating total energy transferred into particle

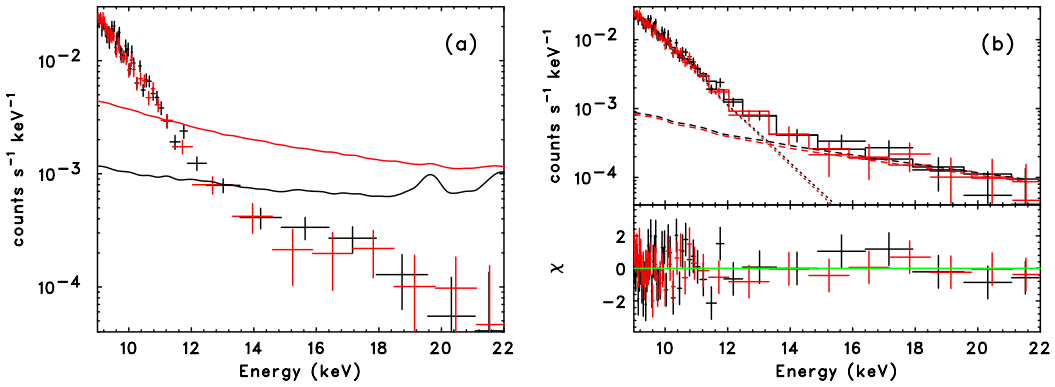

Figure 3.25: (a) Background-subtracted spectra of W49B from *NuSTAR* FPMA (black) and FPMB (red). The solid curves are the background models. (b) Same as the left figure but plotted with the best-fit model. The dotted and dashed curves indicate the RRC and power-law components, respectively. The bottom panel shows residuals from the model. (taken from Tanaka et al., 2018)

acceleration and to considering the injection mechanism of particle acceleration. However, sub-relativistic particles at acceleration sites are almost unexplored. This fact is because it is difficult to explore sub-relativistic particles through above radiation channels. Fluxes of synchrotron X-rays from and gamma-rays via Inverse Compton off sub-relativistic electrons are known to be extremely weaker than those by relativistic electrons. The threshold energy of protons for π^0 production is ~ 280 MeV $(= m_{\rm p}\,c^2 + 2\,m_{\pi}\,c^2 + {m_{\pi}}^2\,c^2/2\,m_{\rm p})$ in the rest system of protons in the ISM so that sub-relativistic protons cannot generate π^0-mesons. Therefore, other diagnostic tools are required to probe them.

Ramaty et al. (1979) pointed out nuclear gamma line emissions in MeV band as one of the promising tools to probe sub-relativistic particles. However, the even most prominent lines from celestial objects are only marginally detectable because of limited sensitivities of instruments and huge background (e.g., Schönfelder et al., 2000). Tanaka et al. (2018) found a significant power-law component, which can be best interpreted as nonthermal bremsstrahlung from sub-relativistic electrons, extending up to ~ 20 keV in *NuSTAR* data of W49B. Figure 3.25 shows the *NuSTAR* spectrum of W49B.

Chapter 4

Instruments

We perform an observational study of RPs utilizing spectral data taken with *XMM-Newton* and a theoretical study toward probing sub-relativistic particles accelerated in SNRs with *XRISM*. Figure 4.1 shows overviews of the X-ray satellites. Both X-ray observatories are equipped with X-ray mirror optics, and enable us to perform X-ray imaging spectroscopy. In the chapter, we briefly summarize basic properties of both satellites.

4.1 *XMM-Newton*

The X-ray Multi-Mirror Mission (*XMM-Newton*) is the X-ray astronomy mission of the European Space Agency. The *XMM-Newton* observatory was successfully launched on December 10, 1999, with an Ariane-V from the Guiana Space Centre. It was thrown into a highly elliptical orbit with an apogee of about 115000 km and a perigee of 6000 km. Its orbital period is about 48 hours. As of 2020, the satellite is in operation and provides us with highly worth data.

Figure 4.2 shows a sketch of *XMM-Newton*. *XMM-Newton* is equipped with three identical X-ray reflective mirrors, and carries three distinct types of cameras which make it possible to simultaneously access X-ray and optical/UV emissions. One of the cameras is the European Photon Imaging Camera (EPIC) consisting of three charge coupled devices (CCDs) for X-ray imaging and moderate resolution spectroscopy. Another is the Reflection Grating Spectrometer (RGS; den Herder et al., 2001) achieving high resolving power (150 to 800) over a range from 5 to 35 Å. The other is Optical/UV Monitor that is CCDs for optical/UV imaging and grism spectroscopy (Mason et al., 2001).

4.1.1 X-ray Telescope

The *XMM-Newton* X-ray Telescope (XRT) utilizes total reflection under the Wolter type-I configuration, which employs paraboloidal and hyperboloidal surfaces as primary and secondary mirrors, respectively. Figure 4.3 shows the overviews of the XRT assemblies. Incident X-rays are focused by the XRT, and ~ 40 % of the total light is dispersed with the grating assemblies in their light paths. The non-dispersed light passes to the EPIC cameras, and the intercepted one is detected by the CCD cameras of the RGS. Each of the three XRT assemblies is comprised of 58 Wolter I grazing-incidence mirrors which are nested in a coaxial and confocal configuration. The grazing angle is as shallow as $30'$, which enables to achieve high effective

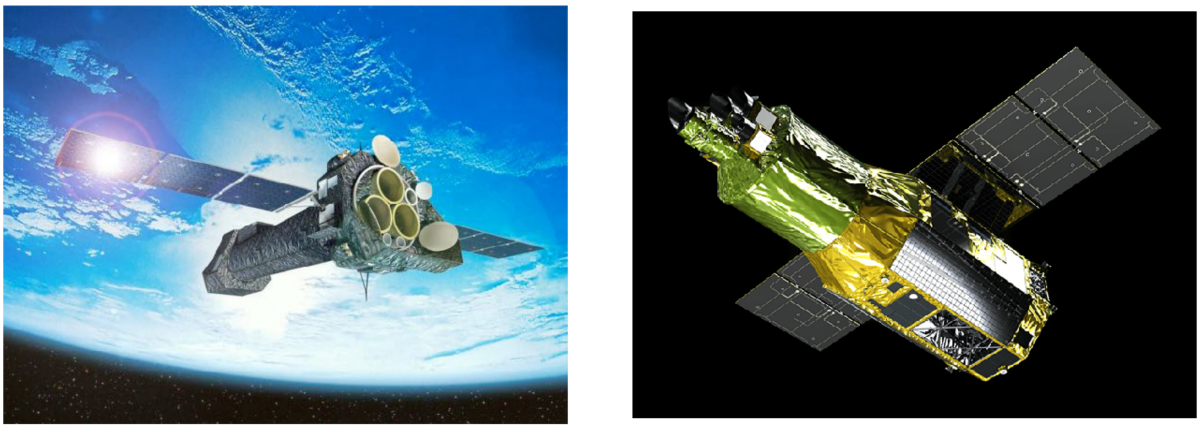

Figure 4.1: Artistic views of (left) *XMM-Newton* and (right) *XRISM* satellites.
<https://www.esa.int/Enabling_Support/Operations/XMM-Newton_operations; https://xrism.isas.jaxa.jp>

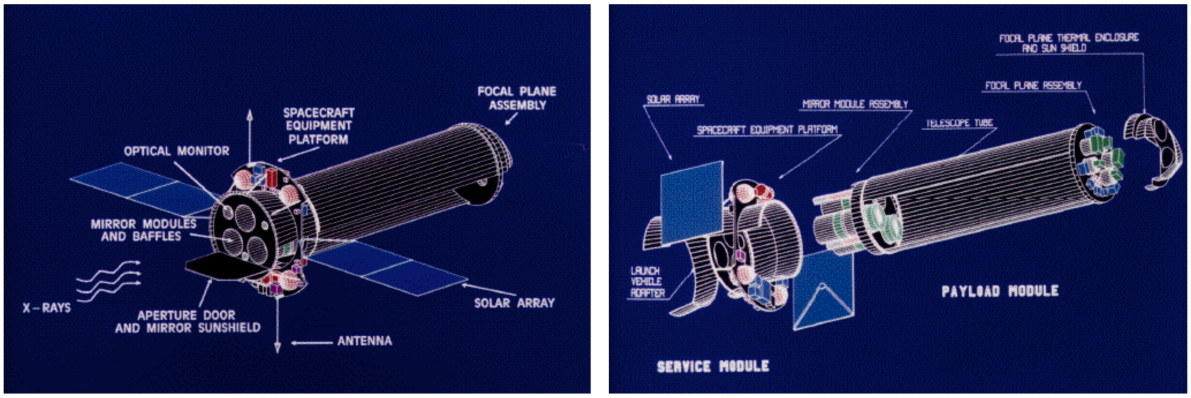

Figure 4.2: In-orbit configuration of the *XMM-Newton* satellite.
<https://heasarc.gsfc.nasa.gov/docs/xmm/xmmhp_gal_hard_schem.html>

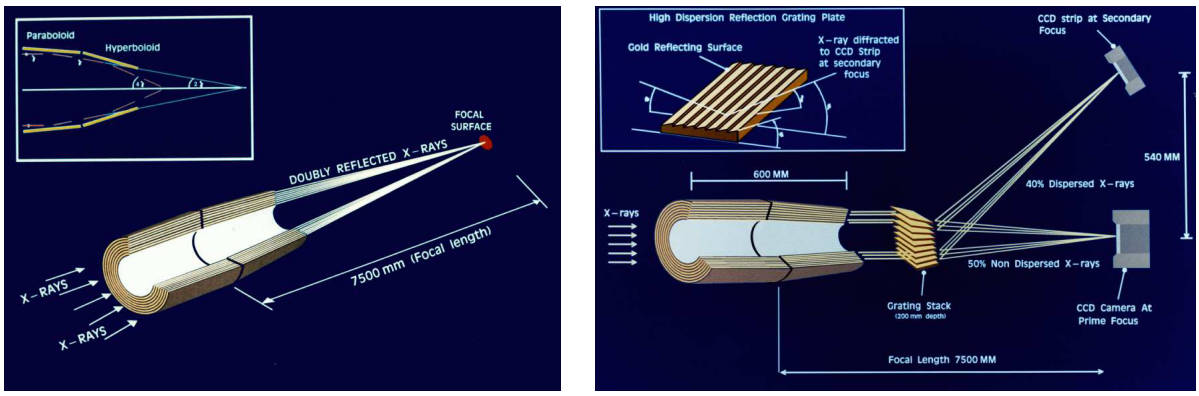

Figure 4.3: (left) Wolter type-I X-ray reflecting optics. (right) Light path in the *XMM-Newton* with grating assemblies. (taken from XMM-Newton Users Handbook)

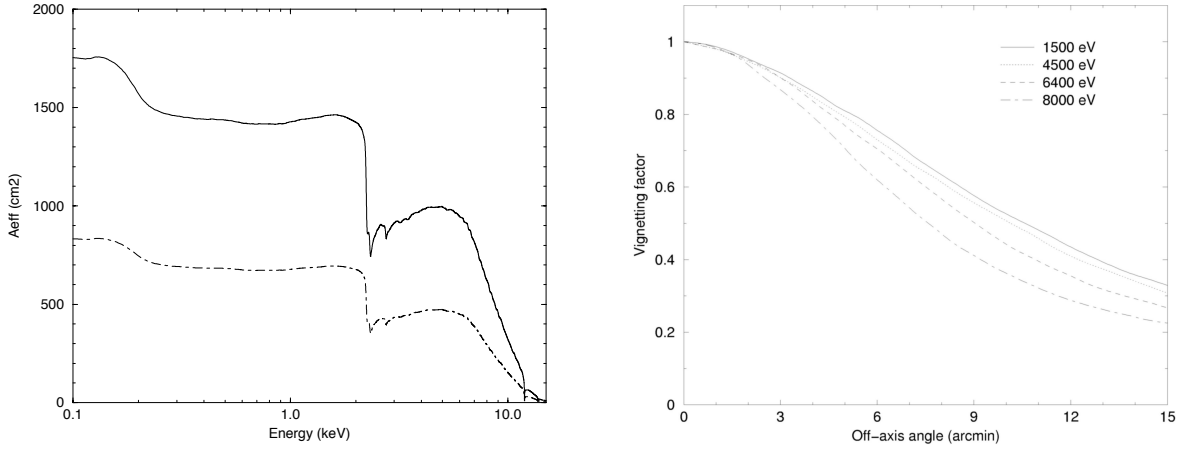

Figure 4.4: (left) Effective area as a function of energy. (right) Vignetting factor defined as the ratio of the effective area against incident angle to that on on-axis. (taken from XMM-Newton Users Handbook)

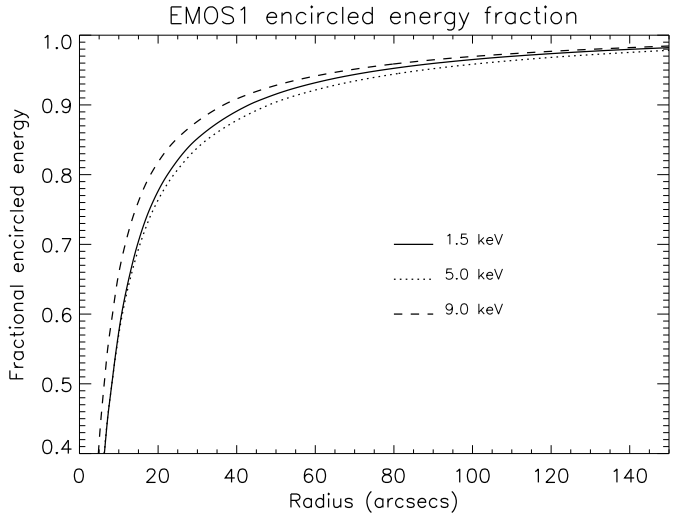

Figure 4.5: MOS fractional encircled energy as a function of angular radius (on-axis). (taken from XMM-Newton Users Handbook)

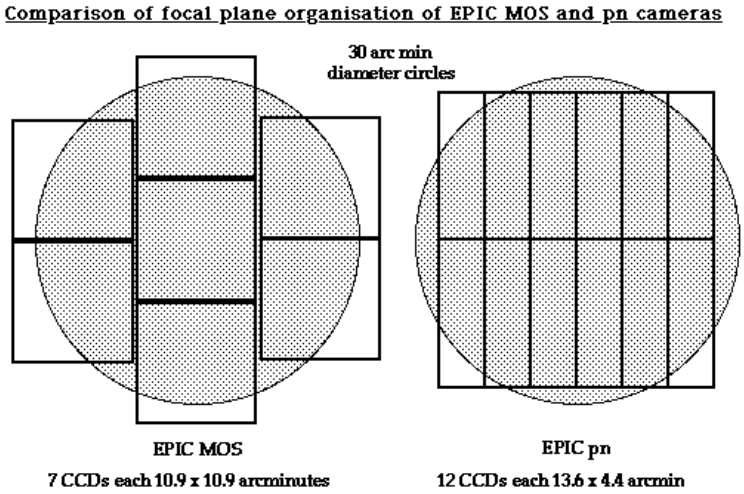

Figure 4.6: Field of view of the two types of EPIC camera; (left) MOS and (right) pn. The shaded circle depicts a 30 diameter area. (taken from XMM-Newton Users Handbook)

area over a wide energy range from 0.15 keV to around 7.0 keV as shown the left panel in Figure 4.4.

Figure 4.4 shows dependences of the effective area of one XRT of *XMM-Newton* against energy of incident X-rays and incident angle to that on on-axis. The dependence of effective area on incident angle is generally called "vignetting" effect. Figure 4.5 shows fractional encircled energy defined as the fraction of X-ray photons collected in a circular region as a function of a diameter. The diameter that encircles 50 % energy is called a Half Power Diameter (HPD), which are used a parameter to compare angular resolution in different satellites.

4.1.2 EPIC

EPIC is composed of two Metal Oxide Semi-conductor (MOS) type CCD cameras, namely MOS1 and MOS2 (Turner et al., 2001), and one pn CCD camera (Strüder et al., 2001). Each MOS camera is comprised of 7 front-illuminated (FI) CCDs as shown in Figure 4.6. The imaging area of the MOS camera is $\sim 2.5 \times 2.5$ cm and is equivalent to about a 30 arcmin-diameter circle. One CCD has 600×600, 40 μm square, pixels. The pn camera is comprised of 12 back-illuminated (BI) CCDs with 200×64 pixels. The pixel size is 150×150 μm. The layout of the pn CCDs is represented in Figure 4.6. The pn array has the imaging area of about 6×6 cm, and almost completely covers the same 30 arcmin-diameter circle as MOS cameras.

Figure 4.7 shows energy resolutions of the MOS and pn CCDs immediately after the launch of the satellite. The quoted values are full widths at half maximum (FWHM) of the Al Kα and Mn Kα lines for on-board calibration after corrections for charge transfer inefficiency. The MOS cameras have better energy resolutions than pn. In Figure 4.7, the energy resolution rapidly degraded by $\sim$10 % early in the mission. In order to suppress thermal noise in CCDs and improve the energy resolution, the decreasing of operation temperature was performed between November and December 2002 (Rev.#530 to #560). After the cooling, the resolution was improved to almost the same value as the pre-launch. Since then, the resolutions of the MOS cameras remain nearly at the improved values. For the pn camera, the energy resolution degrades at about constant small rate as reported by Meidinger et al. (2004). For instance, the rate for the Mn Kα line is ~ 1.2 eV yr^{-1}.

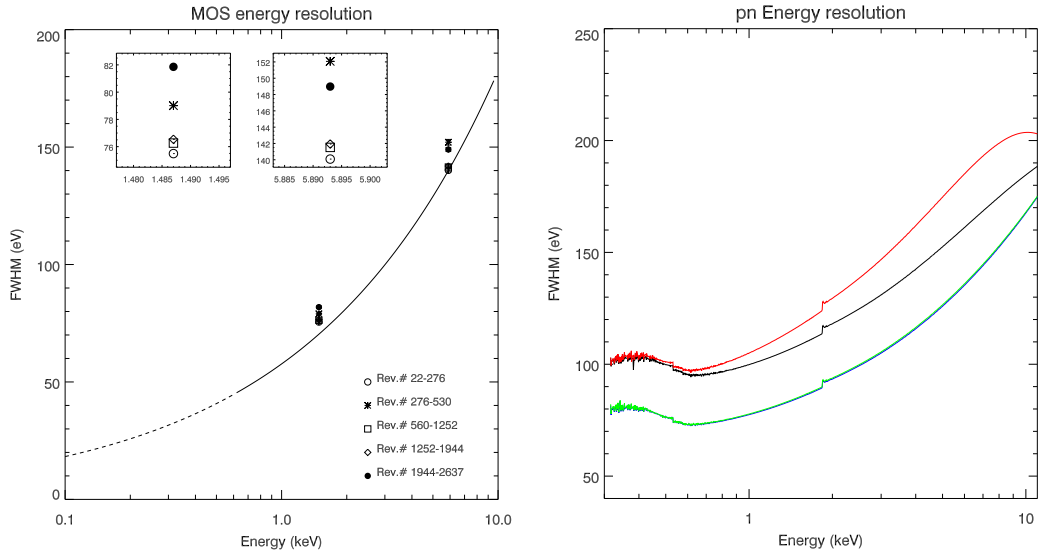

Figure 4.7: (left) Temporal evolution of MOS energy resolution (FWHM) as a function of energy. The solid line is a best-fit curve with a $E^{0.5}$-function based on ground calibration data. Data points represent the FWHM value of the Al Kα (1.478 keV) and Mn Kα (5.893 keV) lines in five different epochs. (right) pn energy resolution for singles. The black, blue, red, green curves correspond to energy resolution calculated with single event data at the bore-sight, single event data closest to the readout node, double event data at the bore-sight, and double event data closet to the readout node, respectively. (taken from XMM-Newton Users Handbook)

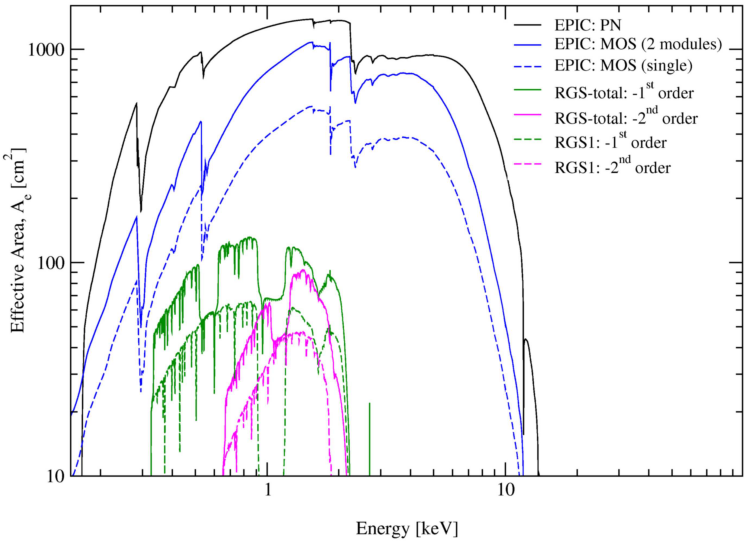

Figure 4.8: Net effective area of EPIC cameras and RGS spectrometer (taken from XMM-Newton Users Handbook)

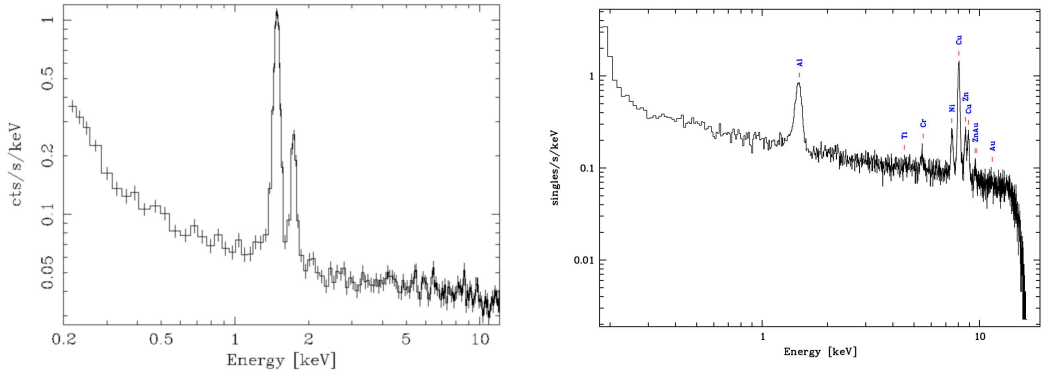

Figure 4.9: Instrumental background spectra of (left) MOS and (right) pn cameras. (taken from XMM-Newton Users Handbook)

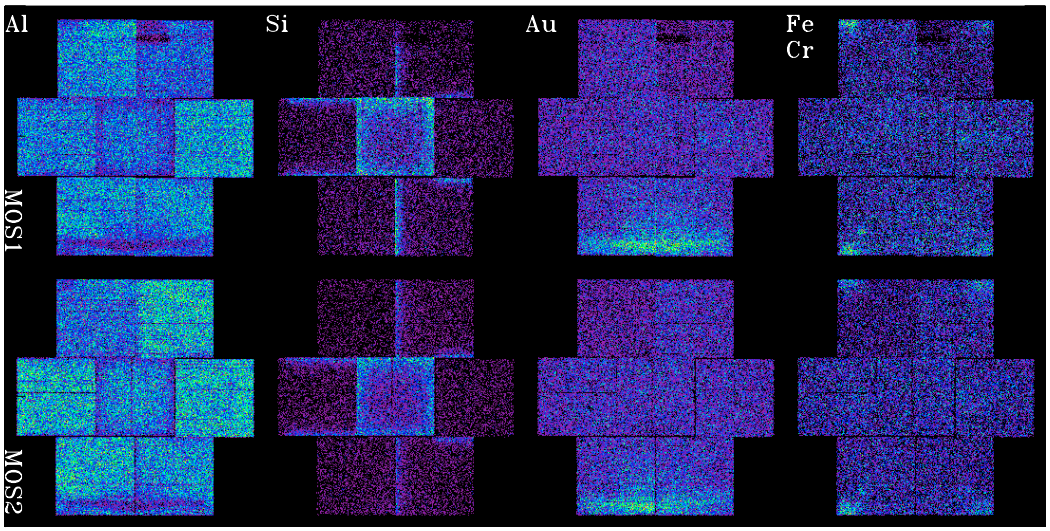

Figure 4.10: Position-to-position variations of the intensities of fluorescent lines on MOS detector plane in instrumental background spectra (Kuntz & Snowden, 2008).

Figure 4.8 shows net effective areas of MOS and pn cameras which is calculated from multiplying the XRT effective area by the quantum efficiencies of them. In contrast to the energy resolution, the pn cameras have larger effective area than MOS. The difference of the curve shape reflects whether the CCDs are FI or BI types. Low-energy X-rays are largely absorbed by the optical blocking filter and by the gate structures of the CCD chips. Since BI chip has the gate on the opposite side from the XRT, the quantum efficiency of the BI CCD used in the pn camera is larger than those of the FI CCD in MOS cameras, in a low-energy band.

EPIC background

EPIC background includes X-ray emission from celestial objects and instrumental background. The latter can be divided into detector noise which becomes dominant at low energies (i.e. below 300 eV) and a component caused by interaction of high energy particles with the structure surrounding the detectors and the detectors themselves. Figure 4.9 shows the instrumental background spectra of MOS and pn cameras. In the energy band above 300 eV, the

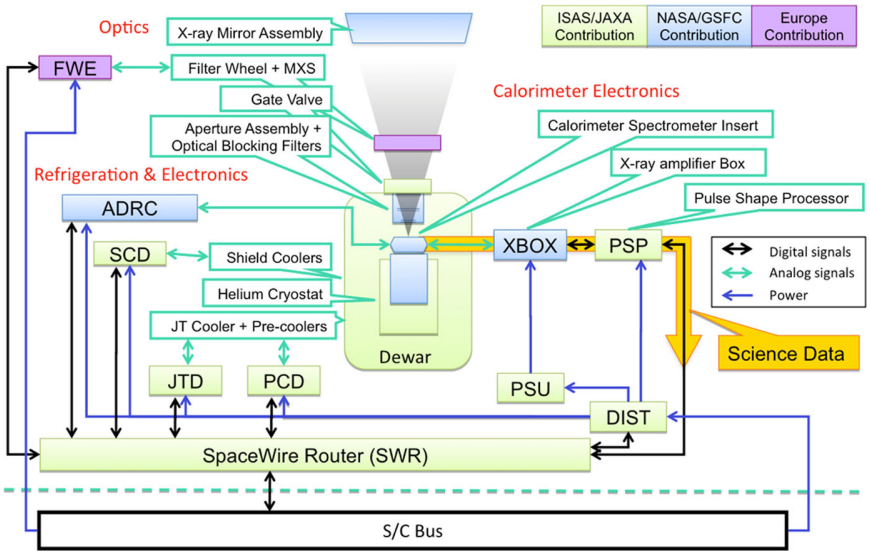

Figure 4.11: Blocking diagram of Resolve (Ishisaki et al., 2018).

spectra have continuum components which are mainly X-rays caused by interaction between cosmic rays and the satellite, and charge generated by invasion of cosmic ray in the CCDs from the direction of the XRT. Further, one can see florescence Al Kα, Si Kα, Ni Kα and Kβ, and Au Lα, Lβ and Mα from materials of the spacecraft. The intensity of these lines has been known to have a very strong spatial dependence as shown in Figure 4.10 (Kuntz & Snowden, 2008).

4.2 *XRISM*

The X-ray Imaging and Spectroscopy Mission (*XRISM*), formerly known as the X-ray Astronomy Recovery Mission (*XARM*), is the 7th Japanese X-ray astronomy satellite, which is to be launched in fiscal year 2022 on a JAXA H-IIA rocket. The *XRISM* satellite carries two X-ray mirror assemblies (XMAs), which are basically identical to those on the *Hitomi* satellite launched in 2016. One of the focal plane detectors, Resolve, is an X-ray micro calorimeter array which will achieve unprecedented high-resolution spectroscopy (FWHM: 5–7 eV) in the 0.3–12 keV bandpass. The other is Xtend using an X-ray CCD camera with a moderate energy resolution and a large field of view of $38' \times 38'$. With these two complementary instruments, *XRISM* will precisely measure plasma condition and kinematics, and open up a new view of the X-ray universe. In this section, we briefly explain the properties of both modules.

4.2.1 Resolve

Resolve is a soft X-ray spectrometer using silicon-thermistor micro-calorimeters. Micro calorimeters are instruments to measure the energies of X-ray photons by using slightly increasings of temperatures of their elements that the X-rays hit. Therefore, during their operations, micro calorimeters are required to be kept in a very low temperature. In Figure 4.11, we show a blocking diagram of Resolve. The Resolve system is divided into the four sub-systems, optics, refrigeration, sensor, and calorimeter electronics. The X-ray micro calorimeters are built into the sensor system, which is cooled in a dewer in the refrigeration system. Calorimeter

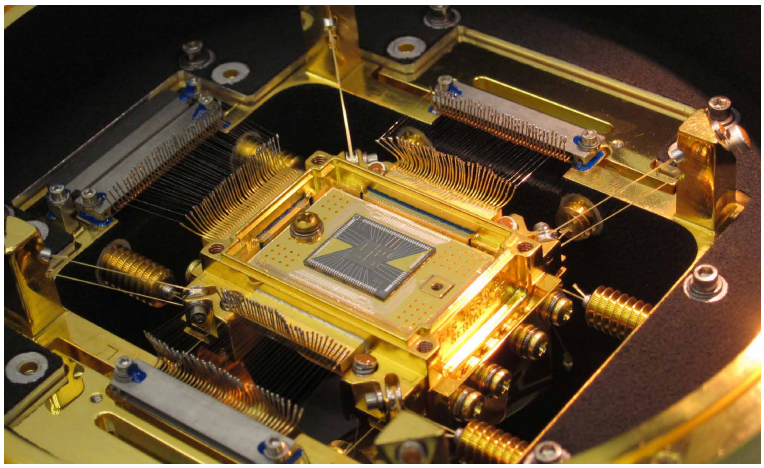

Figure 4.12: Photograph of SXS onboard *Hitomi*. <https://svs.gsfc.nasa.gov/12120>

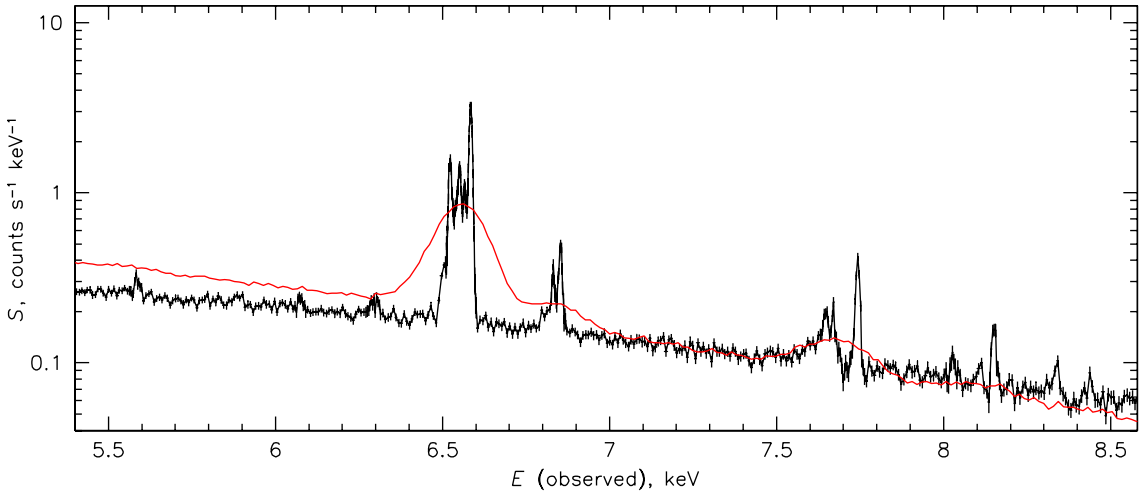

Figure 4.13: Perseus spectrum obtained with SXS onboard *Hitomi* (Hitomi Collaboration et al., 2016). Red line denotes simulated X-ray emission from Perseus folded with instrumental response of the X-ray CCD (XIS) onboard *Suzaku*.

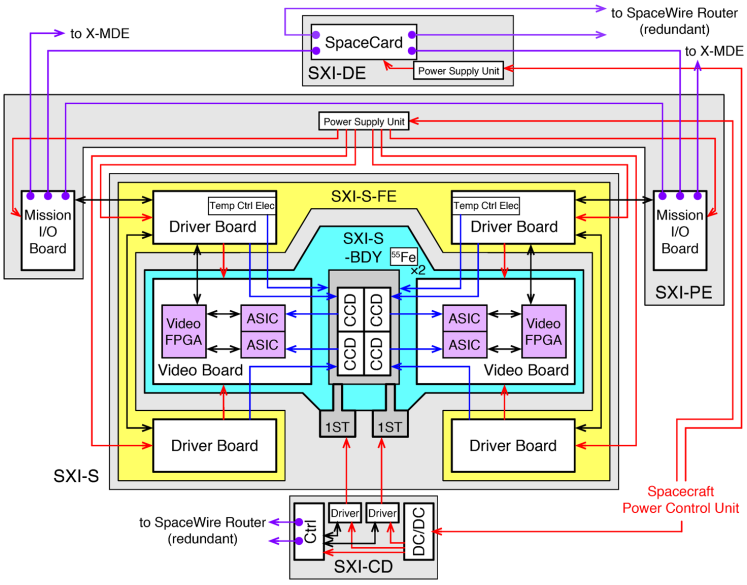

Figure 4.14: Blocking diagram of Xtend (Hayashida et al., 2018).

electronics control the X-ray micro calorimeters and act as a processor of signals output by the micro-calorimeter. Optical system is equipped with filters used if the satellite observes bright celestial objects and an X-ray generator for energy calibration.

Resolve uses a 36-pixel array of X-ray micro calorimeters as shown in Figure 4.12. The Resolve instrument is mostly a copy of the X-ray calorimeter onboard the *Hitomi* (SXS) and its soft X-ray telescope design, though several changes are applied based on the lessons learned from *Hitomi* (e.g., Takei et al., 2018). The instrument was designed to achieve an energy resolution better than 7 eV over the 0.3–12 keV energy range, operated at only 50 mK. The actual energy resolution of the instrument is 4–5 eV as demonstrated during extensive ground tests. Figure 4.13 shows X-ray spectrum of Perseus cluster obtained by the SXS onboard *Hitomi* overlaid with a model folded with instrumental response of *Suzaku* CCDs (XIS) (Hitomi Collaboration et al., 2016). In table 4.1, we summarized key parameters of Resolve.

4.2.2 Xtend

Xtend is a soft X-ray imaging spectrometer with CCDs. Figure 4.14 shows a blocking diagram of the Xtend system. Xtend consists of the camera part (SXI-S) which includes CCDs, analog electronics (the Video Boards and SXI-S-FE), and mechanical coolers (SXI-S-1ST), the pixel processing electronics (SXI-PE), the digital electronics (SXI-DE), and the cooler driver (SXI-CD). The Video Boards digitize singles output by the CCDs and sent them to SXI-PE. Subsequently, the digitized signals are applied to some corrections in SXI-PE and SXI-DE, and event data are extracted from them. During operations of the CCDs, they are cooled down to -120°C with the SXI-S-1ST. SXI-S-1ST is controlled by SXI-CD based on house keeping data (e.g., CCD temperature) monitored by SXI-S-FE.

The Xtend detectors are four P-channel CCDs manufactured by Hamamatsu Photonics K. K, and are designed almost the same as SXI on *Hitomi*. Figure 4.15 shows a layout of the CCDs and a schematic view of one CCD. Each CCD is comprised of 1280×1280 pixels with a 24 μm $\times$ 24 μm pixel size, which yields an imaging area size of 30 mm $\times$ 30 mm. Considering

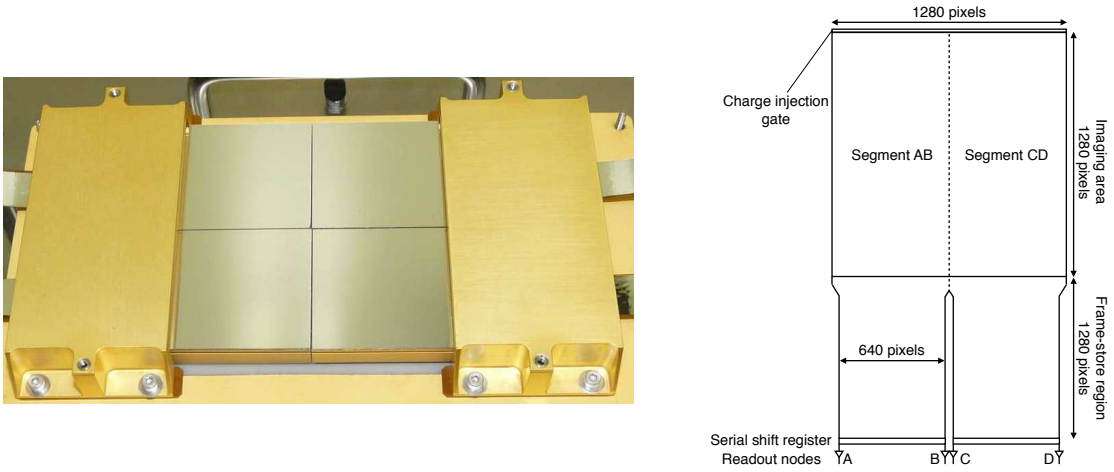

Figure 4.15: (right) Photograph of SXI onboard *Hitomi*, and (left) schematic view of one CCD. (taken from Tanaka et al., 2018)

the advantage of high resistance to damage by micrometeoroids, we employed BI type device. As demonstrated in the case of *Hitomi*, we used the n-type substrates with high resistivity, resulting in higher quantum efficiency for the hard X-ray band compared to BI CCDs onboard previous X-ray satellites. Some improvements have been applied by Kanemaru et al. (2020) and Uchida et al. (2020). Table 4.1 summarizes the required performance of the Xtend.

Table 4.1: Key parameters of Resolve and Xtend.

Item	Resolve	Xtend
Angular resolution (HPD)	$\leq 1.3'$	$\leq 1.3'$
Focal length	5.6 m	5.6 m
Energy band	0.4–12 keV	0.3–12 keV
Energy resolution (FWHM)	≤ 7 eV	≤ 200 eV*/250 eV†
Field of view	$2.9' \times 2.9'$	$38' \times 38'$
Effective Area (at 1 keV)	≥ 160 cm^2	N/A
Effective Area (at 6 keV)	≥ 210 cm^2	≥ 360 cm^2
Time resolution	5 μs	4 s (normal)/0.1 s (burst)
Instrumental background	$\leq 2 \times 10^{-3}$ counts/s/keV/array	$\leq 1 \times 10^{-6}$ counts/s/keV/arcmin^2/cm^2
Operation temperature	50 mK	-120 °C

Detailed parameters from Ishisaki et al. (2018) and Hayashida et al. (2018).
$*$ Required FWHM in begin of life.
† Required FWHM in end of life.

Chapter 5

Physical Origin of RPs in SNRs

5.1 Our Objective and Target Selection

We analyzed *XMM-Newton* data of RP-SNRs, W44 and IC 443, aiming to comprehensively understand the physical origin of RPs in SNRs. Previous studies of RP-SNRs (e.g., Okon et al., 2018; Yamaguchi et al., 2018) demonstrated that spatial comparison between distributions of plasma parameters and that of interacting gas is a powerful tool to investigate the formation process of RPs. These SNRs are ideal targets to carry out this study because interaction between their shock waves and ambient clouds have been studied in detail with radio and infrared observations (e.g., Seta et al., 2004; Lee et al., 2008). W44 and IC 443 have large apparent sizes of $\sim 40'$ and $\sim 65'$, respectively. In addition to a high angular resolution with *XMM-Newton*, the large sizes of them help us to investigate detailed spatial variations of plasma parameters. Throughout this chapter, errors are quoted at 90% confidence levels in the tables and text. Error bars shown in figures correspond 1 σ confidence levels.

5.2 W44

5.2.1 Overview of W44

W44 (a.k.a., G34.7−0.4 or 3C 392) is a Galactic MM SNR with an estimated distance of ~ 3 kpc (Claussen et al., 1997; Ranasinghe & Leahy, 2018). The age of W44 is estimated to be ~ 20 kyr (Smith et al., 1985a; Wolszczan et al., 1991; Harrus et al., 1997). Wolszczan et al. (1991) discovered a radio pulsar, PSR B1853+01, in the southern part of the remnant, indicating that W44 is a remnant of a core-collapse supernova. W44 is known to be interacting with molecular clouds as evidenced by radio observations of OH masers 1720 MHz (Frail & Mitchell, 1998; Claussen et al., 1999) and ^{12}CO lines (Seta et al., 1998, 2004; Yoshiike et al., 2013). Figure 5.1 show the known interacted gas distribution Seta et al. (2004). In the X-ray band, Jones et al. (1993) observed W44 with *Einstein* and reported that the emission is predominantly thermal, based on the presence of Mg, Si, and S emission lines. In *Suzaku* data, Uchida et al. (2012) found RRCs of Si and S, and concluded that the plasmas in the central bright region (Figure 5.2) are in an over-ionized state.

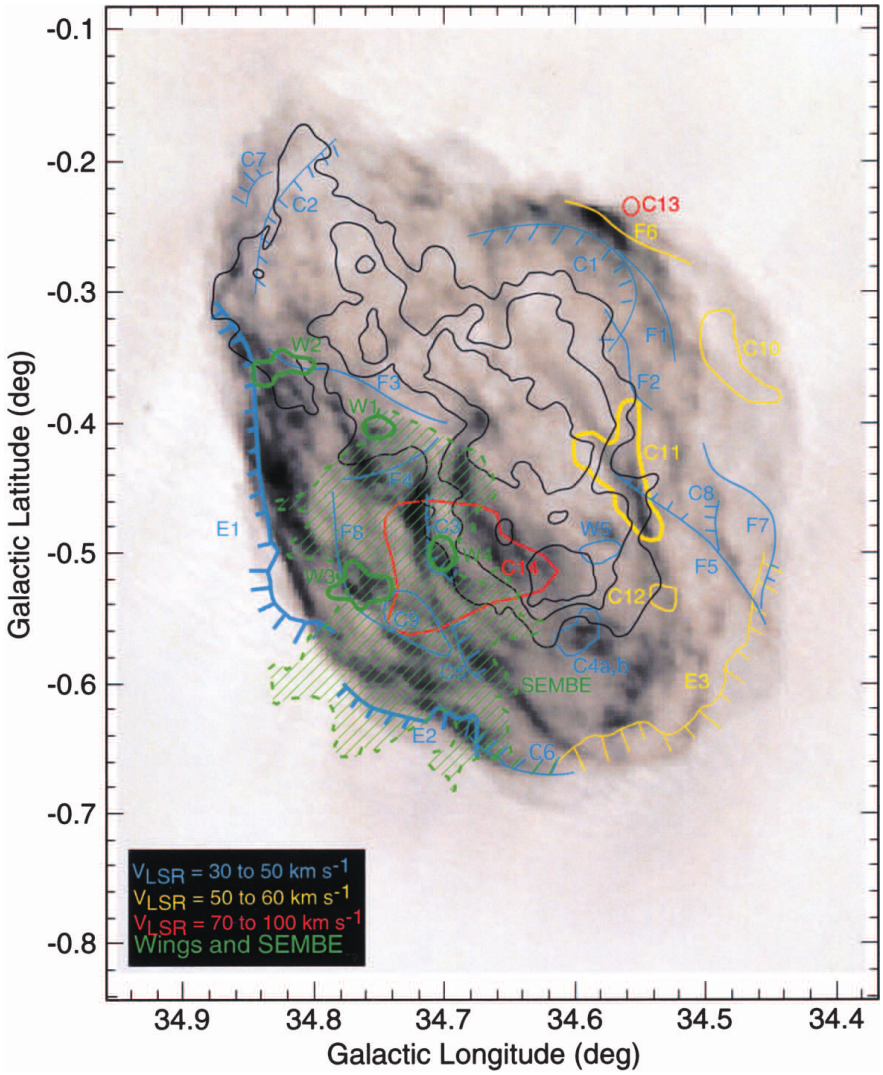

Figure 5.1: Schematic illustration of identified CO features around W44. The colors represent the different velocity ranges of the features. The gray scale shows the radio continuum emission of 1.4 GHz (Jones et al., 1993). The black contours represent the X-ray emission reproduced from Rho et al. (1994). (taken from Seta et al., 2004)

Table 5.1: Observation log of W44.

Target	Obs. ID	Obs. date	(R.A., Dec.)	Exposure
W44 PWN	0551060101	2009 April 24	($18^{\rm h}56^{\rm m}11^{\rm s}.00$, $+01^\circ12'28''.0$)	65 ks
W44	0721630101	2013 October 18	($18^{\rm h}56^{\rm m}06^{\rm s}.99$, $+01^\circ17'54''.0$)	110 ks
W44	0721630201	2013 October 19	($18^{\rm h}56^{\rm m}06^{\rm s}.99$, $+01^\circ17'54''.0$)	92 ks
W44	0721630301	2013 October 23	($18^{\rm h}56^{\rm m}06^{\rm s}.99$, $+01^\circ17'54''.0$)	93 ks

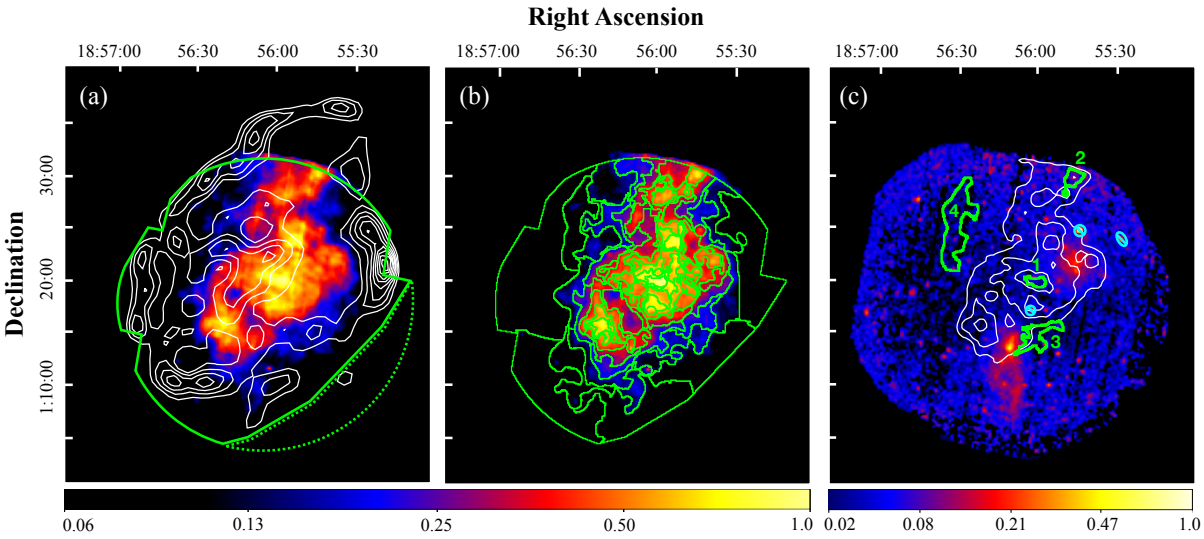

Figure 5.2: MOS+pn images of W44 in the energy band of (a)(b) 0.5–4.0 keV and (c) 4.0–8.0 keV after NXB subtraction and correction for the vignetting effect. The coordinate refers to the J2000.0 epoch. The white contours in panel (a) indicate a radio continuum image at 1.4 GHz taken with the Karl G. Jansky Very Large Array whereas those in panel (c) are the 0.5–4.0 keV X-ray image. The source and background spectra were extracted from the regions enclosed by the solid and dashed lines in panel (a). The source region was divided into 70 sub-regions as shown in panel (b). The regions enclosed by the green lines in panel (c) are the four representative sub-regions whose spectra are plotted in Figure 5.3. The cyan ellipses are regions excluded in the spectral analysis to remove bright point sources.

5.2.2 Observations and Data Reduction

W44 was observed several times with *XMM-Newton* from 2003 to 2013. We discarded datasets whose effective exposures are extremely short because of flaring backgrounds, As a result, four datasets (Obs.ID=0551060101, 0721630101, 0721630201, and 0721630301) were left for further analysis. The details of the observations used are summarized in table 5.1. In what follows, we analyze data obtained with two MOS (Turner et al., 2001) and one pn (Strüder et al., 2001) CCD cameras.

Following the cookbook for analysis procedures of extended sources[1], we reduced the data with the Science Analysis System software version 16.0.0 and the calibration database version 3.9 released in January 2, 2017[2]. We estimated the non-X-ray background (NXB) with `mos-back`. We generated the redistribution matrix files and the ancillary response files by using `mos-spectra`. We used version 12.9.0u of the XSPEC software (Arnaud, 1996) for the following spectral analysis. In the image analysis, we merged MOS1, MOS2 and pn data of the each observation for better photon statistics. In the spectral analysis, we only used the MOS data because of their lower detector background level than the pn data.

[1] ftp://xmm.esac.esa.int/pub/xmm-esas/xmm-esas.pdf
[2] http://xmm2.esac.esa.int/docs/documents/CAL-TN-0018.pdf

5.2.3 Analysis and Results

Imaging Analysis

Figure 5.2 shows vignetting- and exposure-corrected images of W44 taken with the EPIC after NXB subtraction. The soft-band image in Figure 5.2(a) reveals the center-filled morphology and small bright knots as already reported by Shelton et al. (2004) based on *Chandra* data. In order to perform a spatially resolved spectroscopic analysis, we applied the contour binning algorithm (Sanders, 2006) to the 0.5–4.0 keV image, and divided the source region in Figure 5.2(a) into 70 subregions as displayed in Figure 5.2(b). The algorithm generates subregions along the structure of the surface brightness so that each subregion has almost the same signal-to-noise ratio. We manually excluded bright point sources identified in the hard band image in Figure 5.2(c).

Background Estimation

To estimate the X-ray background, we extracted spectra from the off-source region (Figure 5.2) in the field-of-views of each observation. After subtracting the NXB from each of the spectra, we co-added them to perform spectral fitting. The applied model consists of the cosmic X-ray background (CXB), the Galactic ridge X-ray emission (GRXE), and Al and Si Kα lines of instrumental origin which are not included in the NXB spectra estimated with `mos-back` (Lumb et al., 2002). By referring to Kushino et al. (2002), the CXB component was expressed as a power law with a photon index of 1.4 and a 2–10 keV intensity of 6.38×10^{-8} erg cm^{-2} s^{-1} sr^{-1}. We employed the GRXE model by Uchiyama et al. (2013), which is composed of the foreground emission (FE), the high-temperature plasma emission (HP), the low-temperature plasma emission (LP), and the emission from cold matter (CM). We used the Tuebingen-Boulder interstellar medium (ISM) absorption model (TBabs; Wilms et al., 2000) to estimate the column density ($N_{\rm H}{}^{\rm GRXE}$) for the total Galactic absorption in the line of sight toward W44. Most of the parameters of GRXE were fixed to those shown by Uchiyama et al. (2013). Free parameters are $N_{\rm H}{}^{\rm GRXE}$, kT_e of the LP, and the normalization of each component. The best-fit parameters are summarized in table 5.2. We used the best-fit model to account for the X-ray background in the source spectra in §5.2.3.

Spectral Analysis

Figure 5.3 shows background-subtracted MOS spectra extracted from the representative four sub-regions shown in Figure 5.2(c), where emission lines from highly ionized Ne, Mg, Si, S, Ar and Ca are clearly resolved. The Lyα-to-Heα ratios and the continuum shape below ~ 2 keV are different from each other, suggesting significant region-to-region variations of plasma parameters and of absorption column densities. We first fitted spectra from all 70 subregions with a CIE model. The result implies that the X-ray emitting plasma in W44 is over-ionized not only in a part of the remnant, as reported by Uchida et al. (2012) based on *Suzaku* data of the central region, but in the whole remnant.

We then fitted all spectra with the RP model, VVRNEI (Foster et al., 2017), in XSPEC. The model describes emission from a thermal plasma $n_e t$ after an abrupt decrease of the electron temperature from $kT_{\rm init}$ to kT_e under an assumption that the plasma initially was in CIE. Using the TBabs model, we took into account photoelectric absorption by the foreground gas with the solar abundances of Wilms et al. (2000). We allowed the column density $N_{\rm H}$, the electron

Table 5.2: Best-fit model parameters of the background spectrum of W44..

Component function	Model function	Parameter	Value
FE	TBabs (Absorption)	$N_{\rm H}{}^{\rm FE}$ (10^{22} cm^{-2})	0.56 (fixed)
	APEC ($\rm FE_{low}$)	kT_e (keV)	0.09 (fixed)
		$Z_{\rm all}$ (solar)	0.05 (fixed)
		Norm[a]	$1.05^{+0.12}_{-0.16}$
	APEC ($\rm FE_{high}$)	kT_e (keV)	0.59 (fixed)
		$Z_{\rm all}$	0.05 (fixed)
		Norm[a]	$\leq 1.68 \times 10^{-3}$
GRXE	TBabs (Absorption)	$N_{\rm H}{}^{\rm GRXE}$ (10^{22} cm^{-2})	$1.71^{+0.10}_{-0.03}$
	APEC (LP)	kT_e (keV)	$0.56^{+0.03}_{-0.03}$
		$Z_{\rm Ar}$	1.07 (fixed)
		$Z_{\rm other}$	0.81 (fixed)
		Norm[a]	$1.53^{+0.02}_{-0.01}\times 10^{-2}$
	APEC (HP)	kT_e (keV)	6.64 (fixed)
		$Z_{\rm Ar}$	1.07 (fixed)
		$Z_{\rm other}$	0.81 (fixed)
		Norm[a]	= LP Norm. $\times$ 0.29
	Power law (CM)	Γ	2.13 (fixed)
		Norm[b]	≤ 0.20
CXB	TBabs (Absorption)	$N_{\rm H}{}^{\rm CXB}$	$= N_{\rm H}{}^{\rm GRXE} \times 2$
	Power law	Γ	1.40 (fixed)
		Norm[b]	9.69 (fixed)
χ^2_ν (ν)[c]			1.64 (229)

[a] The emission measure integrated over the line of sight, i.e., $(1/4\pi D^2)\int n_e n_{\rm H} dl$ in the unit of 10^{-14} cm^{-5} sr^{-1}.
[b] The unit is photons s^{-1} cm^{-2} keV^{-1} sr^{-1} at 1 keV.
[c] The parameters ${\chi_\nu}^2$ and ν indicate a reduced chi-squared and a degree of freedom, respectively.

Table 5.3: Best-fit model parameters of the spectra from the representative sub-regions in W44.

Model function	Parameters	Region 1	Region 2	Region 3	Region 4
TBabs	$N_{\rm H}$ (10^{22} cm^{-2})	$1.51^{+0.01}_{-0.03}$	1.43±0.07	1.83±0.03	2.8±0.1
VVRNEI	kT_e (keV)	$0.503^{+0.019}_{-0.003}$	$0.55^{+0.04}_{0.03}$	$0.239^{+0.004}_{-0.002}$	0.26±0.01
	$kT_{\rm init}$ (keV)	1.0 (fixed)	1.0 (fixed)	1.0 (fixed)	1.0 (fixed)
	$Z_{\rm Ne}$ (Solar)	$1.29^{+0.06}_{-0.07}$	0.8±0.1	1.7±0.1	3.0±1.0
	$Z_{\rm Mg}$ (Solar)	$1.55^{+0.07}_{-0.05}$	1.1±0.1	1.5±0.1	$2.2^{+0.8}_{-0.4}$
	$Z_{\rm Si}$ (Solar)	$2.68^{+0.09}_{-0.05}$	1.7±0.1	$2.6^{+0.2}_{-0.1}$	$2.6^{+0.9}_{-0.5}$
	$Z_{\rm S} = Z_{\rm Ar} = Z_{\rm Ca}$ (Solar)	2.1±0.1	1.3±0.2	$3.1^{+0.4}_{-0.2}$	3.2±1.0
	$Z_{\rm Fe} = Z_{\rm Ni}$ (Solar)	$0.14^{+0.02}_{-0.01}$	$0.17^{+0.05}_{-0.04}$	1.1±0.1	$1.0^{+0.6}_{-0.5}$
	$n_e t$ (10^{11} cm^{-3}s)	$5.3^{+0.2}_{-0.1}$	6.0±0.1	6.0±0.2	4.0±0.3
	Norm[a]	$0.048^{+0.005}_{-0.003}$	$0.026^{+0.006}_{-0.005}$	0.11±0.04	$0.19^{+0.02}_{-0.01}$
χ^2_ν (ν)[b]		1.45 (217)	1.12 (104)	1.57 (215)	1.25 (104)

[a] The emission measure integrated over the line of sight, i.e., $(1/4\pi D^2)\int n_e n_{\rm H} dl$ in the unit of 10^{-14} cm^{-5} sr^{-1}.
[b] The parameters ${\chi_\nu}^2$ and ν indicate a reduced chi-squared and a degree of freedom, respectively.

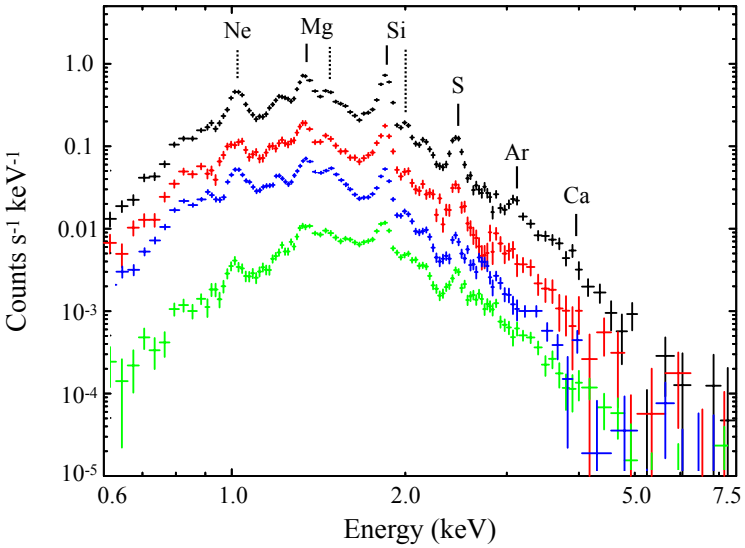

Figure 5.3: MOS (MOS1 + MOS2) spectra extracted from the sub-regions 1 (black), 2 (red), 3 (blue), and 4 (green), whose locations are shown in Figure 5.2(c). The NXB and X-ray background are subtracted. For a display purpose, the spectra of Regions 3 and 4 are scaled by factors of 0.05 and 0.1, respectively. The vertical solid and dashed lines denote the centroid energies of the Heα lines and Lyα lines, respectively.

temperature kT_e, recombining timescale n_et, and normalization of the VVRNEI component to vary. The parameter $kT_{\rm init}$ was fixed in the fittings. We tried $kT_{\rm init}$ of 1.0 keV, 2.0 keV, 3.0 keV, and 5.0 keV, and found that the data are best reproduced with $kT_{\rm init} = 1.0$ keV. We thus show results obtained with $kT_{\rm init}$ fixed at 1.0 keV in what follows. We note that parameters such as $N_{\rm H}$, kT_e, and n_et are insensitive to the choice of $kT_{\rm init}$. The abundances of Ne, Mg, Si, S, and Fe were left free, whereas Ar and Ca were linked to S, and Ni was linked to Fe. The other abundances were fixed to the solar values. To the model for the W44 emission, we added the background model with the parameters fixed to those in Table 5.2. We allowed the normalizations of the Al and Si Kα lines to vary since the line intensities are known to have location-to-location variations on the detector plane (Kuntz & Snowden, 2008).

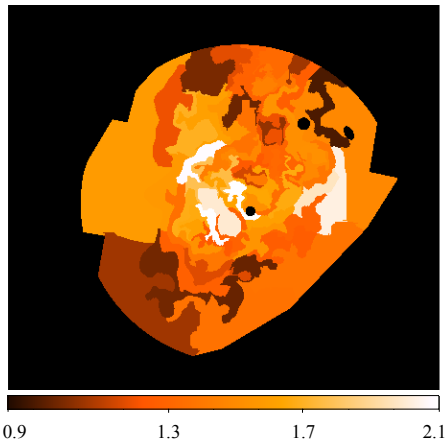

Figure 5.4: Reduced chi-squared map of W44.

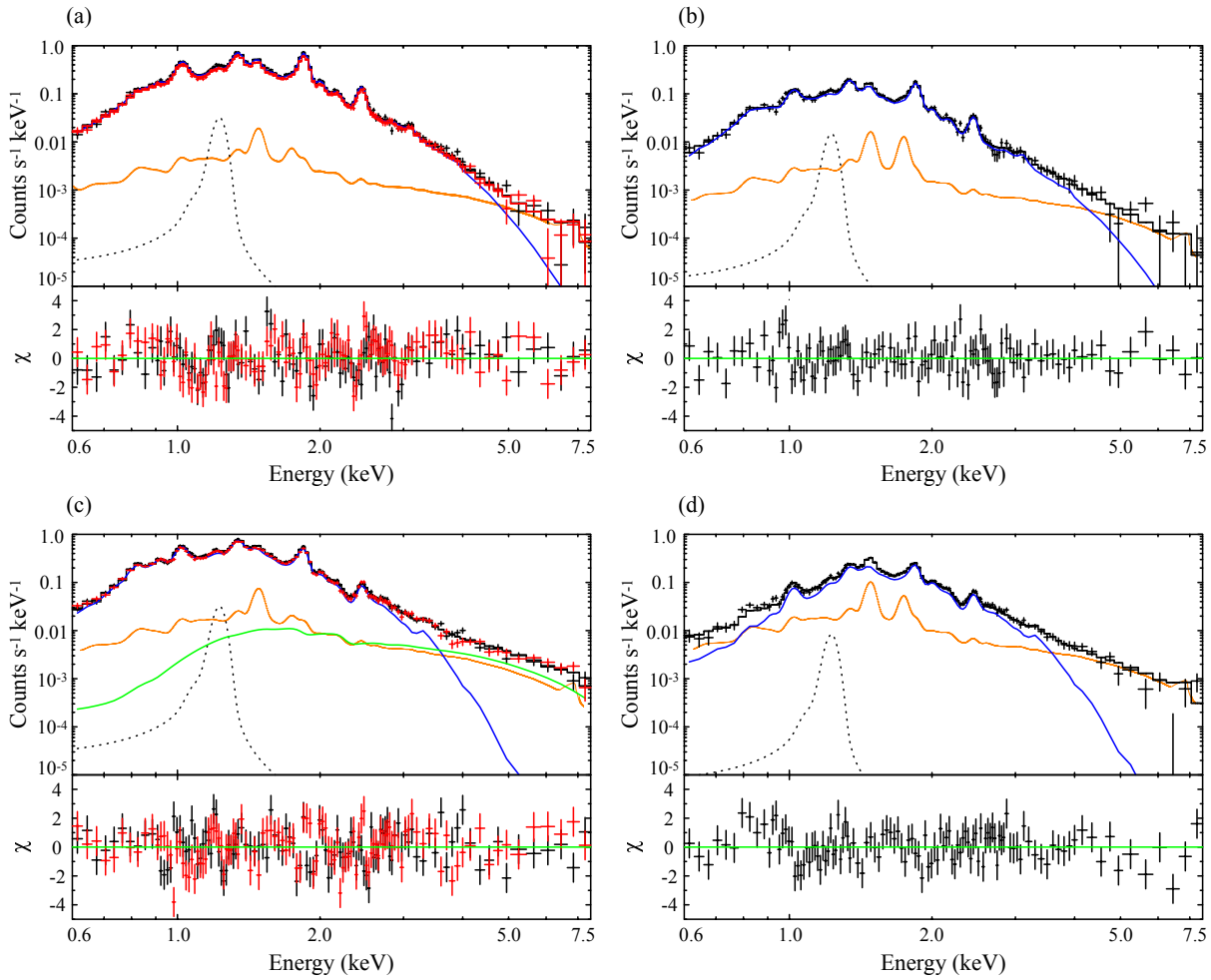

Figure 5.5: (a) MOS1 (red) and MOS2 (black) spectra from Region 1 plotted with the model without a Gaussian for Fe L lines (see text for details). The blue, orange, and black curves represent the RP model, the background, and the sum of the models, respectively. The black dotted curve represent a Gaussian at 1.23 keV added to the model (the black dotted curve). (b)–(d) Same as panel (a) but for Regions 2–4. Since Region 3 is contaminated by the southern hard source (PSR B1853+01 and its PWN), the model includes a power law shown as the green curve. Only MOS2 data are available in Regions 2 and 4 because of malfunction of CCD chips of MOS1.

In the fittings, we noticed line-like residuals at ~ 1.2 keV in most of the sub-regions. However, the used NEI plasma code takes into account of the Fe-L lines (Foster et al., 2017). The residuals could be attributed to uncertainty in emissivity data of Fe-L lines in the code or to physical processes such as charge exchange that are not taken into account here. While the reason for the residuals is not clear, an addition of a Gaussian at 1.23 keV significantly improved the fits. In the case of Region 1 shown in Figure 5.5(a), the fitting statistic was improved from $\chi^2_\nu = 1.54$ with $\nu = 218$ to $\chi^2_\nu = 1.45$ with $\nu = 217$. On the other hand, the addition of the Gaussian does not change the parameters obtained beyond the 90% confidence level. In the spectral analyses, therefore, we used the model including the Gaussian.

Additional components are necessary to fit the spectra from the sub-regions where two extended hard sources are detected (Figure 5.2(c)). Nobukawa et al. (2018) pointed out that the northeastern source, which was discovered by Uchida et al. (2012), is probably a galaxy cluster. To account for the emission, therefore, we employed a CIE model, in which the abundance and kT_e were fixed to the values as determined by Matsumura (2018) while the normalization was left free. The southern source encompasses PSR B1853+01 and its associated pulsar wind nebular (PWN) detected with *Chandra* (Petre et al., 2002). Since their X-ray emissions have featureless continuum spectra (Petre et al., 2002), we used a power law model for the southern source, in which the photon index Γ and the normalization were free parameters.

All 70 spectra are well reproduced by the above RP (with an additional component) model. In addition to the result from Region 1 in Figure 5.5(a), we plot the best-fit models overlaid on the observed spectra from Regions 2–4 in Figure 5.5(b)–(d). In a map in Figure 5.4, we present χ^2_ν values of each sub-region, which range from 0.98 to 2.15. Among all 70 sub-regions, 20 sub-regions have $\chi^2_\nu \geq 1.5$, and 4 sub-regions have $\chi^2_\nu \geq 2.0$.

5.2.4 Discussion on W44

Foreground Gas Distribution

The X-ray absorption column densities ($N_{\rm H}$) obtained from the spectral fittings present a tool to probe the spatial distribution of the gas in front of W44. Figure 5.6 shows a map of $N_{\rm H}$, where a significant spatial variation is clearly visible. The values, ranging from 1.3×10^{22} cm^{-2} to 2.8×10^{22} cm^{-2}, are roughly consistent with the previous studies with *Suzaku* by Uchida et al. (2012) and Matsumura (2018), but the present map revealed a spatial distribution in much finer angular scales. We found that the X-ray absorption column densities are higher in the outer regions and are peaked in the northwestern rim. Based on CO line data, Seta et al. (2004) estimated the column density of foreground gas of $\sim 1 \times 10^{22}$ cm^{-2} and $\sim 2 \times 10^{22}$ cm^{-2} in the inner and outer regions, respectively, which agree well with our X-ray results. Note that the ISM around W44 is dominated by molecular gas and that the contribution from atomic gas amounts to only $\sim 10\%$ of the total mass (Yoshiike et al., 2013). In the northwestern region with the highest X-ray absorption column density, it is known that a giant molecular cloud in the near side of W44 was hit by the SNR shock (Seta et al., 2004). When we select a velocity range of 40–50 km s^{-1}, which includes the most of the gas in the giant molecular cloud, the CO contours show almost a perfect match with the X-ray column density map (Figure 5.6(b)). According to Seta et al. (2004), the foreground gas in the northeastern rim has a column density of $N_{\rm H} \sim 3 \times 10^{22}$ cm^{-2}, which is again consistent with the values estimated from our X-ray analysis.

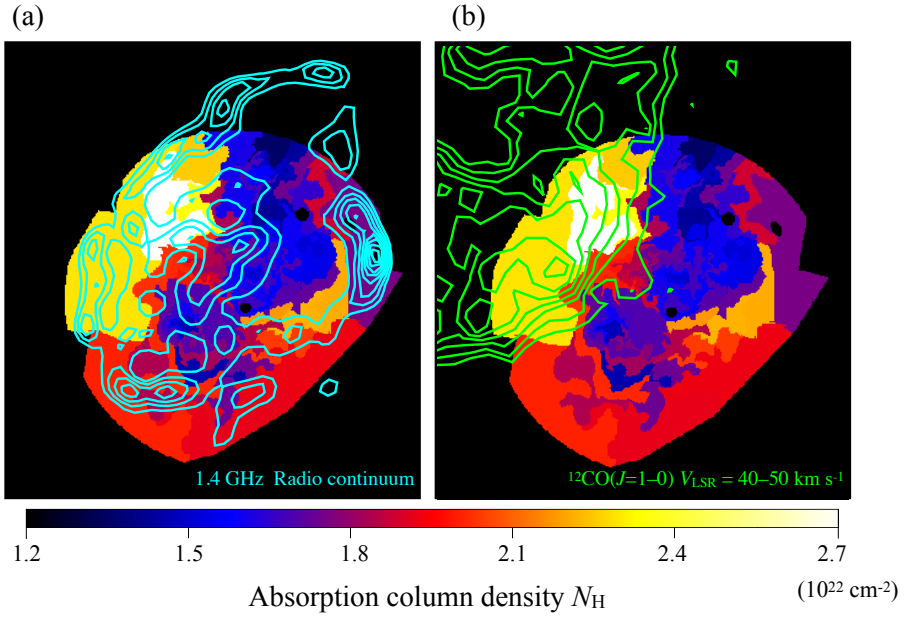

Figure 5.6: Distribution of X-ray absorption column density $N_{\rm H}$. The same radio continuum image as that in Figure 5.2(a) are overlaid as cyan contours in panel (a). The green contours in panel (b) denote ^{12}CO(J = 1–0) emissions in a velocity range of $V_{\rm LSR}$ = 40–50 km s^{-1} as observed with the Nobeyama 45 m radio telescope in the FUGIN project (Umemoto et al., 2017).

Physical Origin of RPs on W44

We now discuss the physical origin of the RPs in W44 based on spatial distributions of the parameters such as kT_e and n_et, and their comparison with interacting gas distributions. Figure 5.7(a) shows a kT_e map. In panel (a-ii), we overlaid a ^{12}CO(J = 2–1)-to-^{12}CO(J = 1–0) intensity ratio map. The line ratio serves as a good indicator of shock-cloud interactions. A ratio well above the typical value in the unshocked part of the cloud, 0.6, indicates that the gas is shocked and/or heated (Yoshiike et al., 2013). The electron temperature kT_e tends to be lower at the locations where the ^{12}CO(J = 2–1)-to-^{12}CO(J = 1–0) ratio is higher. Similar tendencies were found also in other MM SNRs with RPs, IC 443 and W28 (Matsumura et al., 2017b; Okon et al., 2018). Those authors claimed that the tendencies are most probably explained by thermal energy exchanges between the plasmas and clouds via thermal conduction (Zhang et al., 2019). Thus, our result on W44 would also be suggestive of significant thermal conduction between the X-ray emitting plasma and interacting gas.

Information from another parameter, n_et, whose spatial distribution is presented in Figure 5.7(b), has revealed far more convincing evidence for thermal conduction. In Figure 5.8, we plot kT_e and n_et derived for each sub-region. The data points are divided into two groups. The blue points come from regions where Seta et al. (2004) discovered ^{12}CO(J = 1–0) lines broader than ΔV = 7 km s^{-1} in full width at half maximum (see panels (a-iii) and (b-iii) of Figure 5.7 and also Figure 5.8(a) for the locations), referred to as spatially extended moderately broad emission (SEMBE) by Seta et al. (2004). The red points, on the other hand, are from the other regions. The two groups are clearly separated from each other, and each of the two groups shows a clear anti-correlation between kT_e and n_et.

The result in Figure 5.8(b) can be well understood in a context of the thermal conduction scenario as follows. Let us assume that the X-ray emitting plasma initially had an ionization degree close to CIE ($n_e t \sim 10^{12}$ cm^{-3}s) and an electron temperature of $kT_{\rm init} \sim 1$ keV as we assumed in the spectral fittings in 5.2.3. After the shock encountered the molecular cloud, the plasma was rapidly cooled due to thermal conduction. At this point, the plasma switched into an over-ionized state since the cooling proceeded in a timescale shorter than the recombination rate. Once the cooling rate became slower, recombination started to dominate to make the ionization degree gradually approach CIE. What we are currently observing in W44 would be emission from the plasma in this phase. Figure 5.8(c) presents schematic trajectories of the plasma on the kT_e-$n_e t$ plane in the above scenario. The clear separation between the SEMBE and non-SEMBE regions suggests that the plasma was more efficiently cooled in the SEMBE regions.

Although the nature of the SEMBE is not clear yet, a plausible interpretation would be that the SEMBE is emitted by unresolved dense clumps shocked and disturbed by the SNR shock (Seta et al., 2004; Sashida et al., 2013) (Figure 5.9). Since those clumps are embedded in the hot X-ray emitting plasma, cloud evaporation would occur through thermal conduction between the plasma and the clumps, making the plasma in the SEMBE regions efficiently cooled. Cloud evaporation in SNRs are numerically studied with hydrodynamical simulations (e.g., Zhou et al., 2011; Zhang et al., 2019) as well as with magneto-hydrodynamical simulations (e.g., Orlando et al., 2008). According to the result by Zhang et al. (2019), cloud evaporation plays a role in rapid cooling of hot plasma and thus also in over-ionization. Sashida et al. (2013) estimated the clumps in the SEMBE region have a size of $\ll 0.3$ pc. The typical evaporation timescale of the clumps through thermal conduction can be evaluated as $t_{\rm evap} \approx 5.4 \times 10^{10} (n_e/1\ {\rm cm}^{-3})(l/1\ {\rm pc})^2 (kT_e/1\ {\rm keV})^{-5/2}$ s $\ll 10^{11}$ s (e.g., Orlando et al., 2005) , assuming the plasma density $n_e = 1$ cm^{-3}, the clump size $l \ll 0.3$ pc, and the average plasma temperature $kT_e = 0.3$ keV. The evaporation timescale is sufficiently smaller than the timescale for a plasma to reach CIE ($t_{\rm CIE} \approx 10^{12} (n_e/1\ {\rm cm}^{-3})^{-1}$ s), and, therefore, cloud evaporation can make the plasma over-ionized. ALMA would be able to resolve dense clumps of the SEMBE gas in W44 as pointed out by Sashida et al. (2013). Spatially resolved spectroscopy in X-rays with angular scales similar to that of ALMA then should observationally reveal the process of cloud evaporation and resulting over-ionization.

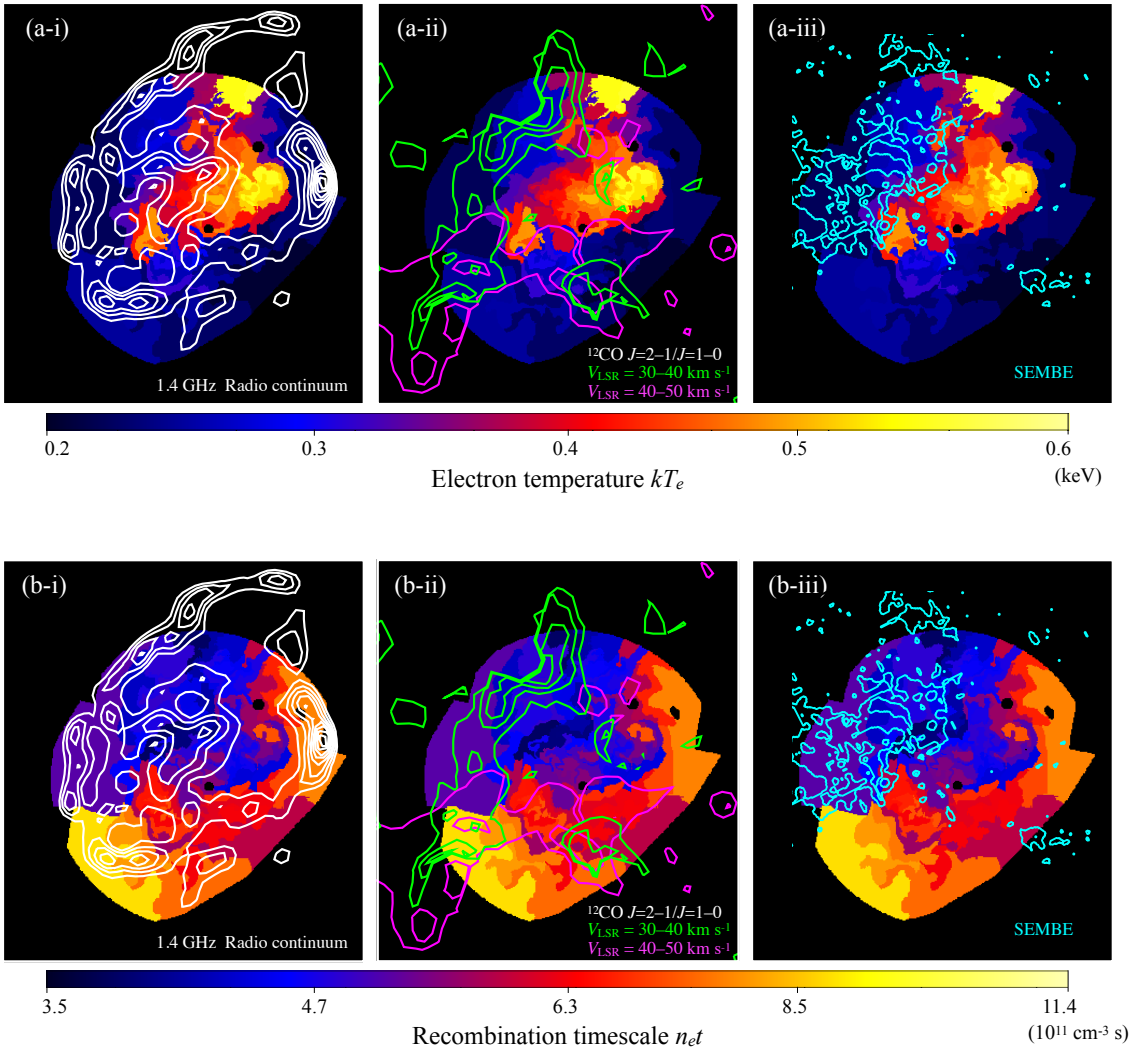

Figure 5.7: Maps presenting the distributions of (a) kT_e and (b) $n_e t$. The white contours in the panels (a-i) and (b-i) indicate the same radio continuum image as that in Figure 5.2(a). The green and magenta contours in panels (a-ii) and (b-ii) denote a ^{12}CO($J = 2$–1)-to-^{12}CO($J = 1$–0) intensity ratio map drawn every 0.1 from 0.7 in $V_{\rm LSR} = 30$–40 km s^{-1} and $V_{\rm LSR} = 40$–50 km s^{-1} taken from Yoshiike et al. (2013). The velocity ranges correspond to that of the giant molecular cloud interacting with W44. In panels (a-iii) and (b-iii), the cyan contours denote the half-intensity line width diagram for the ^{12}CO($J = 1$–0) in $V_{\rm LSR} = 20$–60 km s^{-1} obtained with the Nobeyama 45 m radio telescope by Seta et al. (2004). Each contour represents 7, 10, and 13 km s^{-1}.

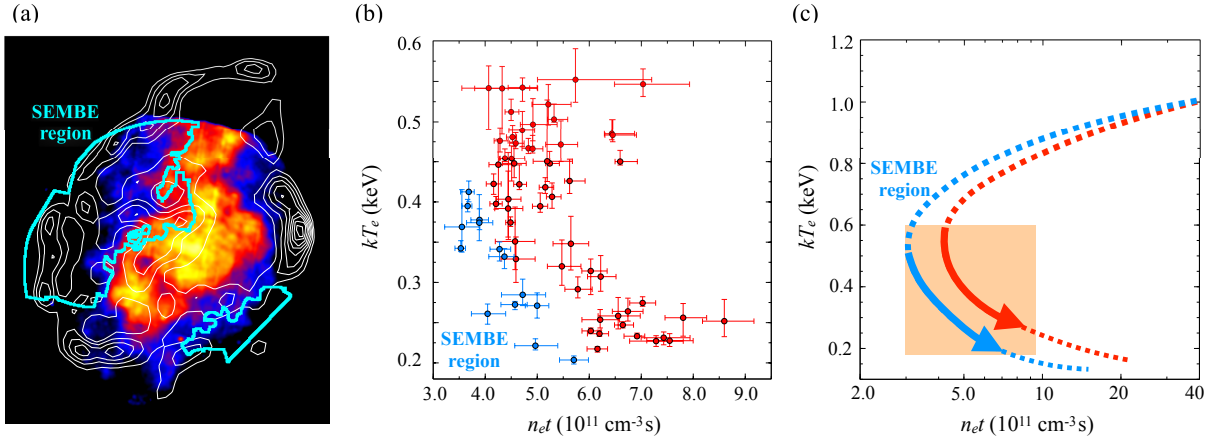

Figure 5.8: (a) Same as Figure 5.2(a) but with the definition of the SEMBE regions in cyan. (b) Relationship between $n_e t$ and kT_e. The blue points are from the SEMBE regions whereas the red points are from the other regions. (c) Schematic trajectories of plasma during its evolution after a shock-cloud collision. The color scheme is the same as that of panel (b). The shaded area corresponds to the range plotted in panel (b).

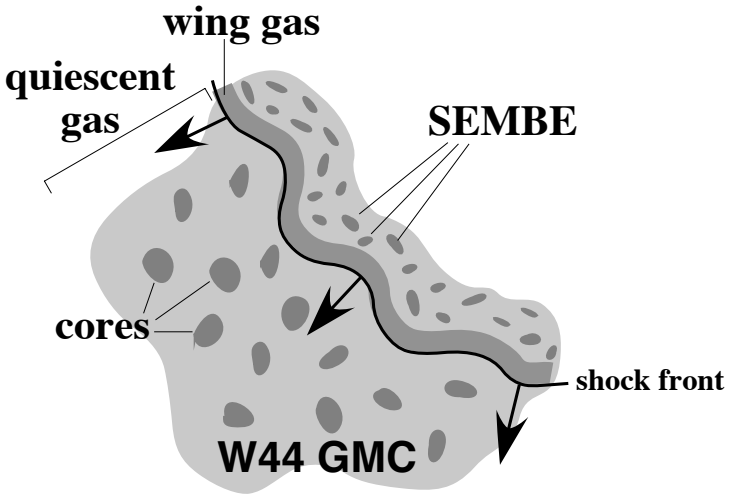

Figure 5.9: Schematic view of the W44 blast wave interacting with the giant molecular cloud (GMC).

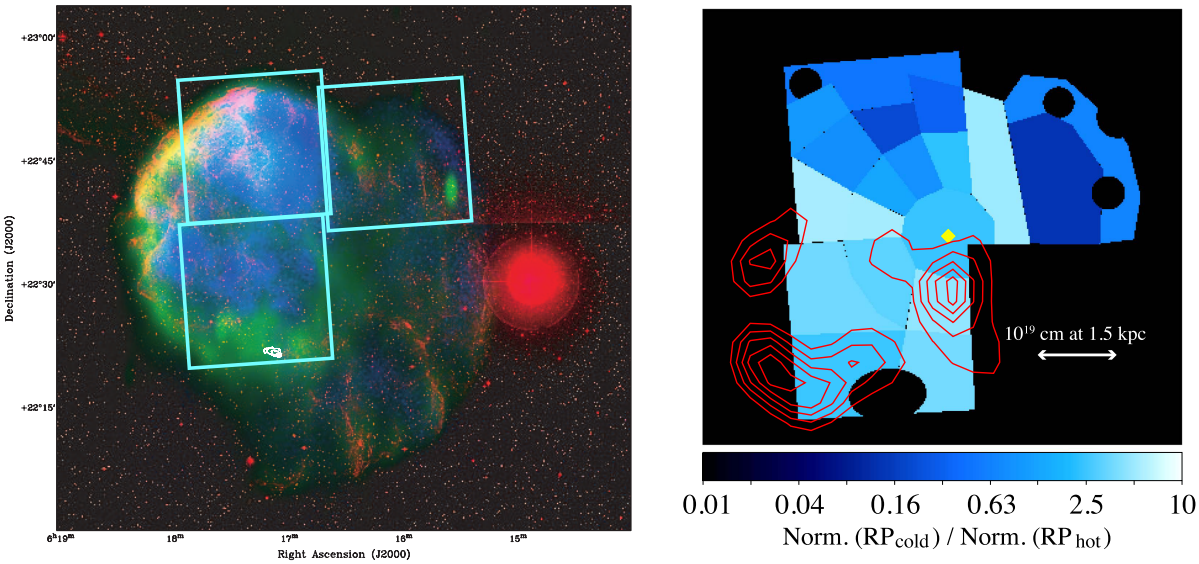

Figure 5.10: (left) Multi-wavelength view of IC 443. The red, green, and, blue correspond to optical (670 nm) taken with the Second Palomar Observatory Sky Survey, 1.4 GHz radio taken by the DRAO Synthesis Telescope, and 0.1–2.4 X-ray images taken by *ROSAT*, respectively. The bright source at the west of IC 443 is a star (Gaensler et al., 2006). The cyan boxes indicate three fields covered by *Suzaku*. (b) Maps of normalization ratio of cold RPs ($kT_e \sim$ 0.15–0.30 keV) to hot RPs ($kT_e \sim$ 0.4–0.6 keV) obtained with *Suzaku* data. The red contours show the ^{12}CO($J = 2$–1) intensity ratio intensity ratio (Yoshiike, 2017). (taken from Matsumura et al., 2017b)

5.3 IC 443

5.3.1 Overview of IC 443

IC 443 (a.k.a., G189.1+3.0) is a Galactic MM-SNR at a distance of ∼1.5 kpc (Welsh & Sallmen, 2003) toward the Galactic anticenter. The age of IC 443 is estimated to be ∼ 20–30 kyr (Olbert et al., 2001; Lee et al., 2008). Olbert et al. (2001) found a PWN 1SAX J0617.1+2221 in the southeastern part of the remnant, suggesting the SNR is of a core-collapse origin. IC 443 is known to be interacting with dense clouds through detections of ^{12}CO lines (Denoyer, 1979; Xu et al., 2011) and H_2 emissions (Rho et al., 2001; Kokusho et al., 2020). Figure 5.11 shows a spatial distribution of ambient clouds traced by ^{12}CO lines (Lee et al., 2012). Previous observations of IC 443 with *Einstein* revealed a centrally concentrated X-ray morphology and the presence of thermal emissions from the bright center (Petre et al., 1988). Kawasaki et al. (2002) claimed that the ionization degree of the plasma is higher than that expected in CIE based on a measurement of the Lyα to Heα line intensity ratio with *ASCA*, as summarized in Section 3.1.3. Yamaguchi et al. (2009) discovered RRCs of Si and S in *Suzaku* data, and showed unequivocal evidence of RPs in IC 443. Subsequent observations with *Suzaku* revealed that that heavier ions such as Ca and Fe are also in the over-ionized state (Ohnishi et al., 2014).

The formation process of RPs in IC 443 has been discussed by some authors such as Matsumura et al. (2017b), Greco et al. (2018), and Hirayama et al. (2019). Matsumura et al. (2017b) found a tendency that the plasma temperature is lower in the region where the shock waves interact with ambient clouds. They claimed that this result is caused by a rapidly cooling of the

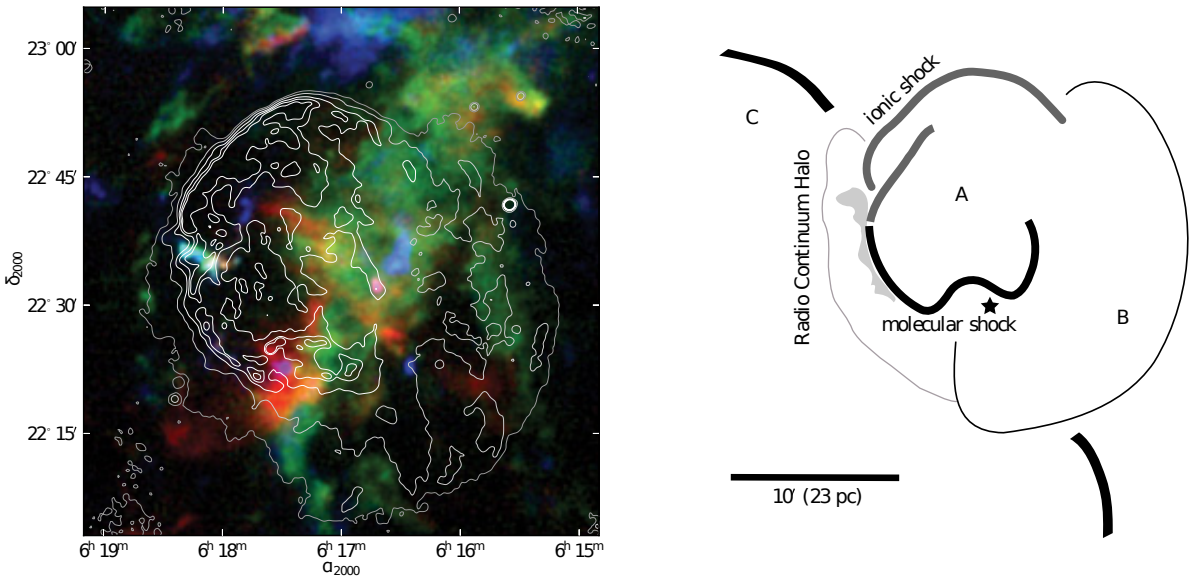

Figure 5.11: (left) Three color (red, green and blue) maps of the integrated intensity of ^{12}CO($J=1$–0) line obtained with the FCRAO 14 m telescope. The difference of the colors corresponds to the difference of radial velocities of the identified CO clouds. The white contours show HI image taken with the Very Large Array. (right) Schematic view of the shell morphology of IC 443. The asterisk indicates the position of PWN 1SAX J0617.1+2221. (taken from Lee et al., 2012)

plasma due to thermal conduction with interacting clouds, and the same mechanism can account for RPs as well. With *XMM-Newton* data, Greco et al. (2018) claimed that an adiabatic expansion in rarefaction scenario proposed by Itoh & Masai (1989) and Shimizu et al. (2012) is responsible for the over-ionization. Their analysis showed that metal-rich plasma, which is interpreted as an ejecta dominant plasma, is in a strongly over-ionized state. Hirayama et al. (2019) focused on the neutral Fe line which would be due to K-shell ionization of Fe atoms in the gas by sub-relativistic protons accelerated in IC 443 (Nobukawa et al., 2019), and proposed a new scenario that is completely different from the above two scenarios. In this scenario, sub-relativistic protons promote ionization of ions in plasma and generate RPs. Given ionization cross sections for them, such protons can more efficiently ionize them than electrons in the SNR plasma. These authors' claims contradict each other and the physical origin of RPs have been still under debate.

In the case of W44, we found that kT_e and n_et of RPs is in the region where the shock is interacting with molecular clouds (Section 5.2). This finding indicate an efficiently cooling via thermal conduction between X-ray emitting and the cold dense gas as the origin of the over-ionization. Therefore, if thermal conduction between SNR plasma and ambient clouds is responsible for RPs in IC 443 as the same as the W44 case, we would expect RPs in a strongly over-ionized sate in the shock-cloud regions.

5.3.2 Observations and Data Reduction

IC 443 was observed with *XMM-Newton* several times from 2003 to 2013. Table 5.4 summarizes the details of the used observations. Once all the observations are combined, the entire

Table 5.4: Observation log of IC 443.

Target	Obs. ID	Obs. date	(R.A., Dec.)	Exposure
IC 443	0114100101	2000-09-26	($6^h17^m27^s.99$, $22°41'44''.0$)	11 ks
IC 443	0114100201	2000-09-25	($6^h16^m14^s.99$, $22°41'60''.0$)	5 ks
IC 443	0114100301	2000-09-27	($6^h17^m27^s.99$, $22°25'14''.0$)	22 ks
IC 443	0114100401	2000-09-28	($6^h16^m14^s.99$, $22°18'02''.5$)	23 ks
IC 443	0114100501	2000-09-25	($6^h16^m14^s.99$, $22°41'60''.0$)	15 ks
IC 443	0114100601	2000-09-27	($6^h17^m27^s.99$, $22°25'14''.0$)	4 ks
IC 443	0301960101	2006-03-30	($6^h18^m04^s.29$, $22°27'33''.0$)	46 ks
IC 443	0600110101	2010-03-17	($6^h17^m06^s.00$, $22°43'24''.0$)	26 ks

region of IC 443 is completely covered by the field of view of *XMM-Newton*. In what follows, we analyze data obtained with the MOS and pn CCD cameras.

We reduced the data with the Science Analysis System software version 16.0.0, following the cookbook for analysis procedures of extended sources[3]. We used the calibration database version 3.9 released in 2017 January 2.9[4]. We generated the redistribution matrix files and the ancillary response files by using `mos-spectra`. In the image analysis, we merged MOS1, MOS2, and pn data of the each observation for better photon statistics, whereas, in the spectral analysis, we only used the MOS data because of their lower detector background level than the pn data.

5.3.3 Analysis and Results

Imaging Analysis

Figure 5.12 shows vignetting- and exposure-corrected images of IC 443 in the energy bands of 0.5–4.0 keV and 4.0–8.0 keV. The source region is overlaid in Figure 5.12(a). To perform spatially resolved spectroscopic analysis, we applied the same method as that used in the image analysis of W44. We applied the contour-binning algorithm (Sanders, 2006) to the 0.5–4.0 keV image, and divided the source region into 110 subregions as displayed in Figure 5.12(b). We found the PWN 1SAX J0617.1+2221, its PSR, and some bright point sources in the the 4.0–8.0 keV image (Figure 5.12(c)), which are reported by Bocchino & Bykov (2003). For the following spectral analysis, we manually excluded the identified point sources whereas we performed a model fitting of X-rays from the PWN and its PWN according to the work by Bocchino & Bykov (2003).

Background Estimation

For X-ray background estimation, we used spectrum extracted from the source-off region in Figure 5.12(c). After subtracting the non-Xray background (NXB) estimated with `mos-back` from the spectra, we fitted the spectra with a model consisting of the X-ray background model by Masui et al. (2009) who studied the soft X-ray emission from the the Galactic anticenter. The model consists of the cosmic X-ray background (CXB), the local hot bubble (LHB), two thermal

[3] ftp://xmm.esac.esa.int/pub/xmm-esas/xmm-esas.pdf
[4] http://xmm2.esac.esa.int/docs/documents/CAL-TN-0018.pdf

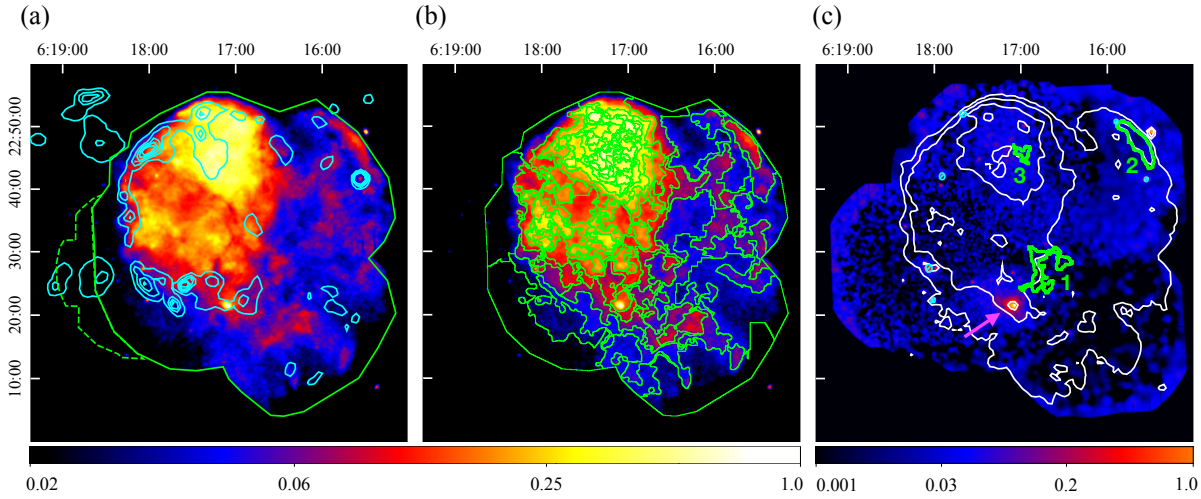

Figure 5.12: MOS+pn images of IC 443 in the energy band of (a)(b) 0.5–4.0 keV and (c) 4.0–8.0 keV after NXB subtraction and correction for the vignetting effect. The coordinate refers to the J2000.0 epoch. The cyan contours in panel (a) indicate a radio continuum image at 1.4 GHz taken with the the NRAO VLA Sky Survey whereas those in pane (c) are the 0.5–4.0 keV X-ray image. The source and background spectra were extracted from the regions enclosed by the solid and dashed lines in panel (a). The source region was divided into 110 sub-regions as shown in panel (b). The regions enclosed by the green lines in panel (c) are the three representative sub-regions whose spectra are plotted in Figure 5.13. The cyan ellipses are regions excluded in the spectral analysis to remove bright point sources. The magenta arrow indicates PWN 1SAX J0617.1+2221.

components for the Galactic halo (GH_{cold} and GH_{hot}). The photon index of the CXB component was fixed to 1.4 in Kushino et al. (2002) whereas the normalization and the column density (N_H^{CXB}) for the total Galactic absorption were allowed to vary. We used the Tuebingen-Boulder interstellar medium absorption model (TBabs; Wilms et al., 2000) for the interstellar absorption. Most of the parameters of the LHB, GH_{hot}, and GH_{cold} models were fixed to values given by Masui et al. (2009), whereas we sat the electron temperature kT_e of GH_{hot} and the normalization of each component as free parameters. We used additional two Gaussian components to model neutral Al and Si Kα lines of instrumental background, which are not included in the NXB spectra (Lumb et al., 2002). The normalization of the Al and Si Kα lines were allowed to vary. The best-fit parameters are summarized in Table 5.5. In the subsequent spectral analysis, we used the best-fit model to account for the X-ray background.

Spectral analysis

Figure 5.13 shows spectra extracted from the representative regions in Figure 5.12(c). One can clearly see resolved emission lines from highly ionized O, Ne, Mg, Si, S, and Ar ions, and the different Lyα-to-Heα intensity ratio and the continuum shape in each spectrum. The different spectral features, as demonstrated in the W44 case, indicate significant region-to-region variations of plasma parameters and of absorption column densities toward IC 443. When we tried a collisional ionization equilibrium (CIE) model for all spectra from 110 subregions, almost all fittings left apparent hump-like residuals at ~ 2.7 keV and ~ 3.5 keV, which correspond

Table 5.5: Best-fit model parameters of the background spectrum of IC443.

Component function	Model function	Parameter	Value
GH	APEC (GH_{cold})	kT_e (keV)	0.658 (fixed)
		Norm[a]	12.5 ± 1.2
	APEC (GH_{hot})	kT_e (keV)	1.22 ± 0.02
		Norm[a]	$66.8^{+5.7}_{-6.9}$
LHB	APEC	kT_e (keV)	0.105 (fixed)
		Norm[a]	$45.1^{+7.7}_{-7.6}$
CXB	TBabs (Absorption)	$N_H{}^{CXB}$	$0.60^{+0.06}_{-0.05}$
	Power law	Γ	1.40 (fixed)
		Norm[b]	$12.1^{+1.3}_{-1.1}$
χ^2_ν (ν)[c]			1.44 (187)

[a] The emission measure integrated over the line of sight, i.e., $(1/4\pi D^2)\int n_e n_H dl$ in the unit of 10^{-14} cm^{-5} sr^{-1}.
[b] The unit is photons s^{-1} cm^{-2} keV^{-1} sr^{-1} at 1 keV.
[c] The parameters ${\chi_\nu}^2$ and ν indicate a reduced chi-squared and a degree of freedom, respectively.

Table 5.6: Best-fit model parameters of the spectra from the representative sub-regions in IC443..

Model function	Parameters	Region 1	Region 2	Region 3 (RP)	Region 3 (RP+CIE)
TBabs	N_H (10^{22} cm^{-2})	$1.02^{+0.4}_{-0.03}$	0.82±0.04	0.82±0.03	0.90±0.01
VVRNEI	kT_e (keV)	0.24 ± 0.02	$0.22^{+0.03}_{0.02}$	0.35±0.02	0.26±0.02
(RP comp)	kT_{init} (keV)	5.0 (fixed)	5.0 (fixed)	5.0 (fixed)	5.0 (fixed)
	Z_O (Solar)	0.4 ± 0.1	0.5±0.2	0.7±0.2	< 1.6
	Z_{Ne} (Solar)	0.9±0.2	0.7±0.2	1.1±0.2	1.6±0.2
	Z_{Mg} (Solar)	0.7±0.1	0.7±0.2	0.8±0.1	$1.1^{+0.1}_{-0.2}$
	Z_{Si} (Solar)	0.4±0.1	$1.0^{+0.3}_{-0.2}$	1.2±0.2	1.8±0.2
	$Z_S = Z_{Ar} = Z_{Ca}$ (Solar)	$0.7^{+0.2}_{-0.1}$	1.3±0.2	1.1±0.2	1.3±0.2
	$Z_{Fe} = Z_{Ni}$ (Solar)	$0.24^{+0.07}_{-0.08}$	0.5±0.1	0.30±0.05	0.4±0.1
	$n_e t$ (10^{11} cm^{-3}s)	$4.5^{+0.3}_{-0.2}$	$13.0^{+1.4}_{-1.3}$	6.1±0.3	$5.5^{+0.4}_{-0.3}$
	Norm[a]	$0.3^{+0.009}_{-0.007}$	0.13±0.03	0.15±0.02	0.07±0.01
APEC	kT_e (keV)	-	-	-	$0.22^{+0.09}_{-0.08}$
(CIE comp)	Z_{all} (Solar)	-	-	-	1.0 (fixed)
	Norm[a]	-	-	-	$0.11^{+0.02}_{-0.03}$
χ^2_ν (ν)[b]		1.07 (224)	0.98 (224)	2.08 (224)	1.39 (222)

[a] The emission measure integrated over the line of sight, i.e., $(1/4\pi D^2)\int n_e n_H dl$ in the unit of 10^{-14} cm^{-5} sr^{-1}.
[b] The parameters ${\chi_\nu}^2$ and ν indicate a reduced chi-squared and a degree of freedom, respectively.

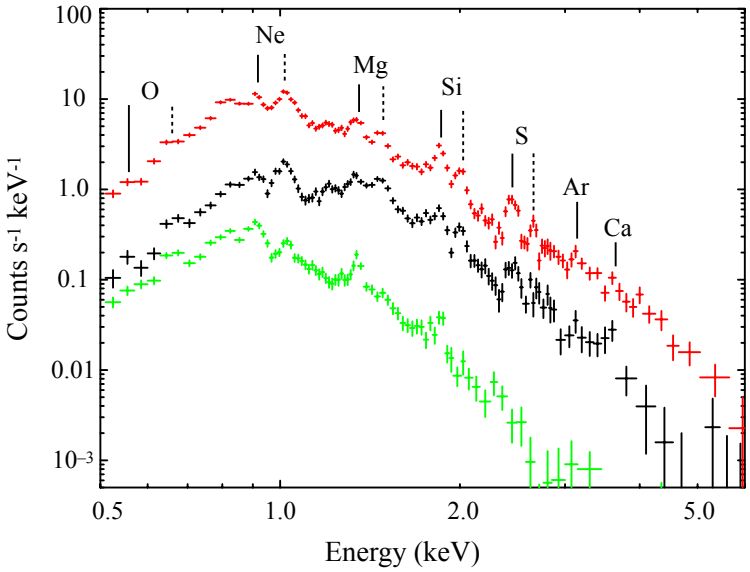

Figure 5.13: MOS (MOS1 + MOS2) spectra extracted from the sub-regions 1 (black), 2 (red), 3 (blue), and 4 (green), whose locations are shown in Figure 5.12(c). The NXB and X-ray background are subtracted. For a display purpose, the spectra of Regions 3 and 4 are scaled by factors of 0.05 and 0.1, respectively. The vertical solid and dashed lines denote the centroid energies of the Heα lines and Lyα lines, respectively.

to the edges of the H-like Si and H-like S RRCs, respectively. The result implies that the X-ray emitting plasma is in over-ionized state not only in a part of IC 443 reported by the previous works (e.g., Matsumura et al., 2017b; Greco et al., 2018), but also almost in the whole remnant.

We then fitted all spectra with the VVRNEI (Foster et al., 2017) model implemented in the XSPEC software version 12.10.1f (Arnaud, 1996). To take account for photoelectric absorption by the foreground gas, we applied the TBabs model with the solar abundances (Wilms et al., 2000). We allowed the column density $N_{\rm H}$, the present electron temperature kT_e, recombining timescale n_et, and normalization of the VVRNEI component to vary. The initial plasma temperature $kT_{\rm init}$ in the spectral fittings is constrained to be ≥ 5 keV, in which, except for Fe, ions such as O–S are almost fully ionized. We fixed the initial plasma temperature $kT_{\rm init}$ at 5 keV because parameters such as $N_{\rm H}$, kT_e, and n_et are insensitive to the choice of $kT_{\rm init}$. The abundances of O, Ne, Mg, Si, S, and Fe were left free, whereas Ar and Ca were linked to S, and Ni was linked to Fe. The abundances of the other elements were fixed to solar. In spectral fittings of the subregions where PWN 1SAX J0617.1+2221 or its pulsar are observed, we applied a model which consists of the VVRNEI model and an additional power law to account for emission from them. The photon index Γ and the normalization of the power law component were free parameters. We allowed the Al and Si Kα line intensity to vary since the line intensities are known to have location-to-location variations on the detector plane (Kuntz & Snowden, 2008).

Most spectra from all subregion are well reproduced by the RP model (or the RP model with the additional power law). In Figure 5.14(a) and (b), we show the results of the fittings in Regions 1 and 2 indicated in Figure 5.12. We also present a map of χ^2_ν obtained with all spectral fittings in Figure 5.15(c-i). Among 110 subregions, 36 sub-regions have $2.0 > \chi^2_\nu \geq 1.5$, and 17 subregions have $\chi^2_\nu \geq 2.0$. The locations of all $\chi^2_\nu \geq 2.0$ subregions are enclosed by the cyan line in Figure 5.15(a). Figure 5.14(c-i) shows the spectral fitting in Region 3, which is one of

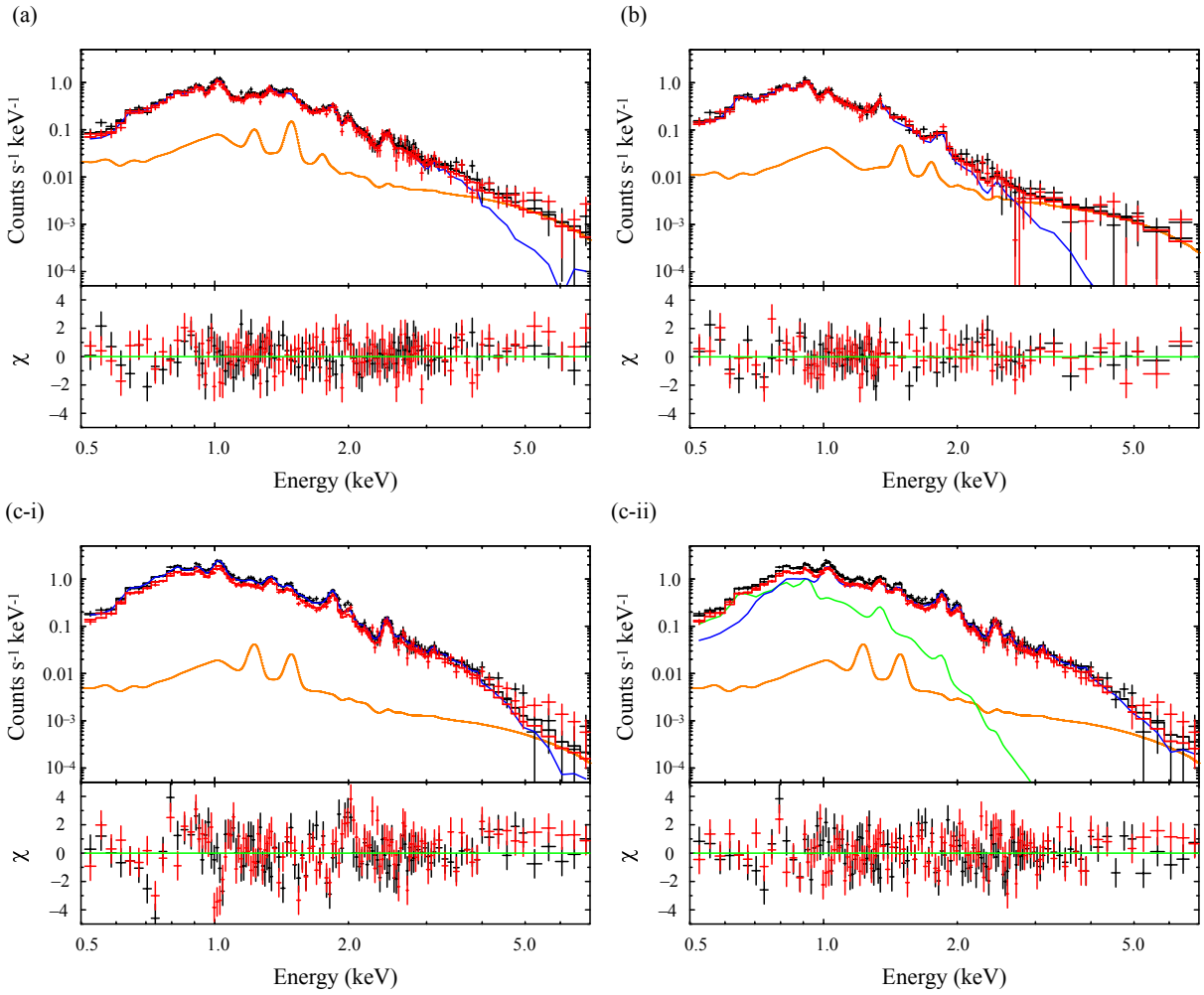

Figure 5.14: (a) MOS1 (red) and MOS2 (black) spectra from Region 1 plotted with the model. The blue and black curves represent the RP model and the sum of the models for MOS1 data, respectively. The red line represent the sum of the models for MOS2 data. (b)–(c) Same as panel (a) but for Regions 2–3. In Region 3, the green curve show the CIE component.

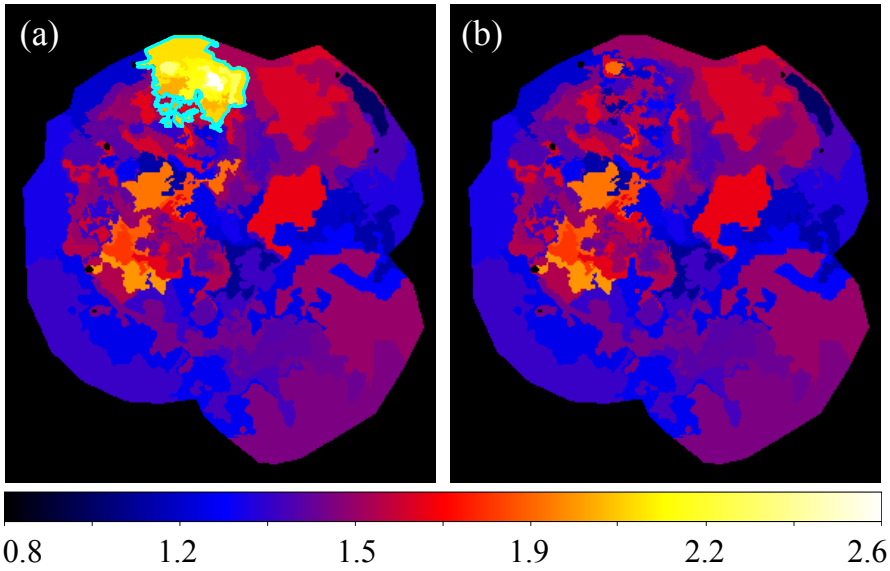

Figure 5.15: (a) Reduced chi-squared map with the single-RP model. The cyan curve indicates the $\chi^2_\nu \geq 2.0$ subregions. (b) Same as (a) but for the RP+CIE model.

the $\chi^2 \geq 2.0$ subregions. The fitting left remarkable residuals at $\sim$ 1.0 keV around H-like Ne Lyα line and $\sim$ 2.0 keV around H-like Si Lyα line, suggesting that required ion population of ions are different between the soft-band and hard-band. We obtained similar results in all fitting with $\chi^2_\nu \geq 2.0$ subregions. Using *Suzaku* data, Matsumura et al. (2017b) reported that a cold ISM component is not negligible in addition to the hot RP. Greco et al. (2018) showed similar fitting results with *XMM-Newton* data. Following the previous works, we add the CIE of the ISM origin to the RP model. The CIE+RP model can explain well the overall spectrum of Region 3 in Figure 5.13(c-ii), and the fit statistic was improved from χ^2_ν = 2.08 with ν = 225 to χ^2_ν =1.39 with ν = 223. We applied the CIE+RP model for spectral fitting in all $\chi^2_\nu \geq 2.0$ subregions. Figure 5.15(b) presents a map of χ^2_ν, and all subregions finally have $\chi^2_\nu \leq 2.0$.

5.3.4 Discussion on IC 443

Foreground Gas Distribution

In a map in Figure 5.16, we present the X-ray absorption column density $N_{\rm H}$ of each subregion. The map shows higher values in sub-regions where the ^{12}CO($J = 1-0$) line is detected with the NANTEN2 telescope (Yoshiike, 2017). The match between the ^{12}CO contours and $N_{\rm H}$, pointed out first by Matsumura et al. (2017b), supports an interpretation that most of the gas traced by the CO line present in front of IC 443. We roughly estimated the column density of the foreground gas to be $\sim 0.6 \times 10^{22}$ cm^{-2} by subtracting the low $N_{\rm H}$ in the ^{12}CO line not observed sub-regions from the high one in the ^{12}CO line observed sub-regions. Yoshiike (2017) estimated the column density $N_{\rm H,\ CO} \sim 0.6 \times 10^{22}$ cm^{-2} of the gas with the CO data of NANTEN2. Given that the amount of the atomic gas traced by HI emissions is less than that of the gas traced by the CO line (Yoshiike, 2017), our measurement can be regarded to be consistent with the radio one.

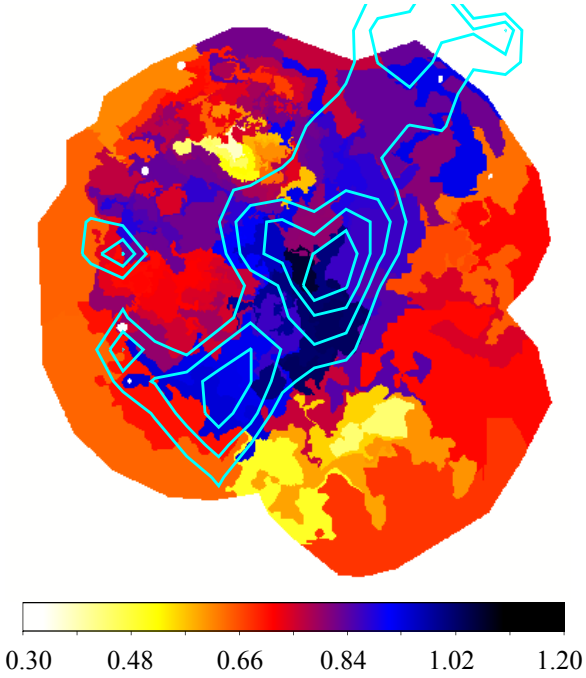

Figure 5.16: Distribution of X-ray absorption column density $N_{\rm H}$. The cyan contours denote ^{12}CO(J = 1–0) emissions in a velocity range of $V_{\rm LSR} = -18$–$+2$ km s^{-1} as observed with obtained from the NANTEN2 (Yoshiike, 2017).

Physical Origin of RPs on IC 443

Matsumura et al. (2017b) reported that the decrease of kT_e in the shock-cloud region is most probably caused by a thermal energy exchange between the plasma and the clouds. They also claimed that a cooling by the thermal energy exchange can generate RPs in IC 443 as well. In Figure 5.17, we present maps of kT_e and n_et, and overlay the ^{12}CO($J = 2-1$) to ^{12}CO($J = 1-0$) intensity ratio (Yoshiike, 2017) and H_2 1–0 S(1) line contours, which are good indicators of shock-cloud interactions. In Figure 5.18, we showed the values of kT_e and n_et derived for each sub-region, and divided data points into red and blue groups. The red points are from on-cloud subregions where the ^{12}CO line ratio or H_2 emissions are detected, whereas the blue points are from the other subregions. The maps and plot revealed that RPs in the on-cloud subregions tend to have smaller kT_e and n_et. In the context of the plasma cooling proposed by Matsumura et al. (2017b), this tendency is naturally interpreted as the result of rapid cooling.

It is notable that our results on IC 443 is similar to the W44 case. Regions with lower kT_e and n_et in W44 completely coincide with the locations where spatially extended broad ^{12}CO line, so called SEMBE, is observed (Subsubection 5.2.4). Although the nature of SEMBE is not clear yet, the emission is considered to be from small clumps ($\ll 0.3$ pc) disturbed after the shock propagation (Seta et al., 2004; Sashida et al., 2013). Based on the observational results, we pointed out that hot plasma is efficiently cooled by the evaporation of the clumps via thermal conduction (Subsubsection 5.2.4). The noteworthy facts suggest that the same mechanism accounts for the kT_e and n_et tendency in IC 443.

Charge fractions for each ion species, computed with Equation 3.10, and kT_e and n_et, are parameters which enable us to directly evaluate the over ionization degree in RPs. Following the theoretical work by Zhang et al. (2019), we used the average charge of ions $C_{\rm RP}$ in RPs, and

the deviation of the average charge ΔC from the CIE state with the same kT_e,

$$\overline{C} = \sum c_i F_i \tag{5.1}$$

$$\Delta C = \overline{C_{\rm RP}}(kT_e, n_e t, kT_{\rm init} = 5\ {\rm keV}) - \overline{C_{\rm CIE}}(kT_e), \tag{5.2}$$

where c_i and F_i are the charge number and fraction of i-times ion, respectively. Larger ΔC would be expected in RPs in a strongly over-ionized state.

Figure 5.19(a-i)-(e-i) and (a-ii)-(f-ii) show $C_{\rm RP}$ and ΔC values as functions of $n_e t$ and kT_e, respectively. We overlay the same kT_e-$n_e t$ plot as Figure 5.18 on the $C_{\rm RP}$ and ΔC maps. In Figure 5.19(a-iii)-(f-iii), we present maps of ΔC computed with the best-fit values. RPs in the on-cloud sub-regions tend to have larger ΔC for Ne-Si ions, which is consistent with the interpretation of over-ionization by the rapid cooling in the thermal conduction scenario. On the other hand, the ΔC map for Fe ions shows a different tendency from that of Ne-S ions. The ΔC of Fe ions is larger in RPs with higher kT_e and smaller $n_e t$, which seems to be difficult to explain by simple thermal conduction between the molecular clouds and plasma. In order to discuss ΔC in more detail, spectral analysis taking account for SNR evolution would be helpful. For instance, we assumed that plasma initially was in a CIE state and its ionization state is uniform over the entire remnant, but two condition would be not realistic. Inhomogeneous gas distribution around SNRs should be considered as discussed in Ustamujic et al. (2020).

Another plausible formation process of RPs is a rapid cooling through adiabatic expansion. Yamaguchi et al. (2018) found a clear positive correlation between kT_e and $n_e t$ in W49B, which is naturally interpreted as the result of the efficient cooling in a rarefied region with a lower density. IC 443 has northeast and southwest shells with different radii, which reflect an ambient gas density (e.g., Lee et al., 2008). The kT_e-$n_e t$ plot in IC 443 shows not a positive but roughly negative correlation as shown in Figure 5.18. This tendency is indeed similar to the W44 case where Okon et al. (2020) claimed the thermal conduction scenario as the formation process of RPs. The rarefaction scenario cannot naturally explain the spatial variation of ΔC. If we consider rarefaction as the formation process of RPs, larger ΔC would be in the southwest region with a low ambient gas density.

We also test the possibility of the over-ionization caused by bombardment of sub-relativistic protons proposed by Hirayama et al. (2019). Figure 5.20 summarizes the Si ion population in RPs with typical parameters obtained, $kT_e = 0.3$ keV, $n_e t = 6.0 \times 10^{11}$ cm^{-3}s, and $kT_{\rm init} = 5.0$ keV, and that in CIE plasma with the same kT_e. To explain the strong H-like Si RRC in the IC 443 spectra, He-like Si ions must be ionized to H-like Si by sub-relativistic protons.

Let us estimate the required energy density of sub-relativistic protons under the condition that the ionization by the proton bombardment proceeds faster than the relaxation toward CIE state. The ionization rate ξ and the energy density $\epsilon_{\rm p}$ can be described as follows,

$$\xi = \int \sigma_{\rm i} v \frac{dn_{\rm p}}{dE} dE, \tag{5.3}$$

$$\epsilon_{\rm p} = \int E \frac{dn_{\rm p}}{dE} dE, \tag{5.4}$$

where $\sigma_{\rm i}$ is ionization cross section from He-like Si to H-like Si ion by proton impacts. Assuming the LECRps spectrum $dn_{\rm p}/dE \propto E^{-2}$ expected in diffusive shock acceleration at a strong shock, the ξ and $\epsilon_{\rm p}$ can be estimated as

$$\xi \sim \left(\frac{n_{\rm p}}{1.0\ {\rm cm}^{-3}}\right) \times 4.4 \times 10^{-12}\ {\rm s}^{-1}, \tag{5.5}$$

$$\epsilon_{\rm p} \sim \left(\frac{n_{\rm p}}{1.0\ {\rm cm}^{-3}}\right) \times 1.2\ {\rm MeV/cm}^3, \tag{5.6}$$

where the n_p is the LECRp density integrated from the energy range from 0.2 MeV to 200 MeV corresponding to the integral range of equations 5.3 and 5.4. Smith & Hughes (2010) computed the characteristic timescale toward CIE state at

$$\Lambda \sim \left(\frac{n_e}{1.0\ {\rm cm}^{-3}}\right)^{-1} \times 10^{12}\ {\rm s}. \tag{5.7}$$

If ξ is larger than Λ^{-1}, the ionization proceeds faster than the relaxation toward the CIE state. To realize this condition, the LECRp density n_p and energy density ϵ_p are required to be ≥ 0.22 cm^{-3} and ≥ 0.24 MeV cm^{-3} if n_e is 1.0 cm^{-3}. If protons are filled in the entire IC 443, whose volume is assumed to be a sphere with a radius of $\sim$ 10 pc, the total proton energy exceeds the typical kinetic energy ($\sim 10^{51}$ erg) in SNe. Our estimation indicates that the ionization by LECRp is difficult to generate RPs.

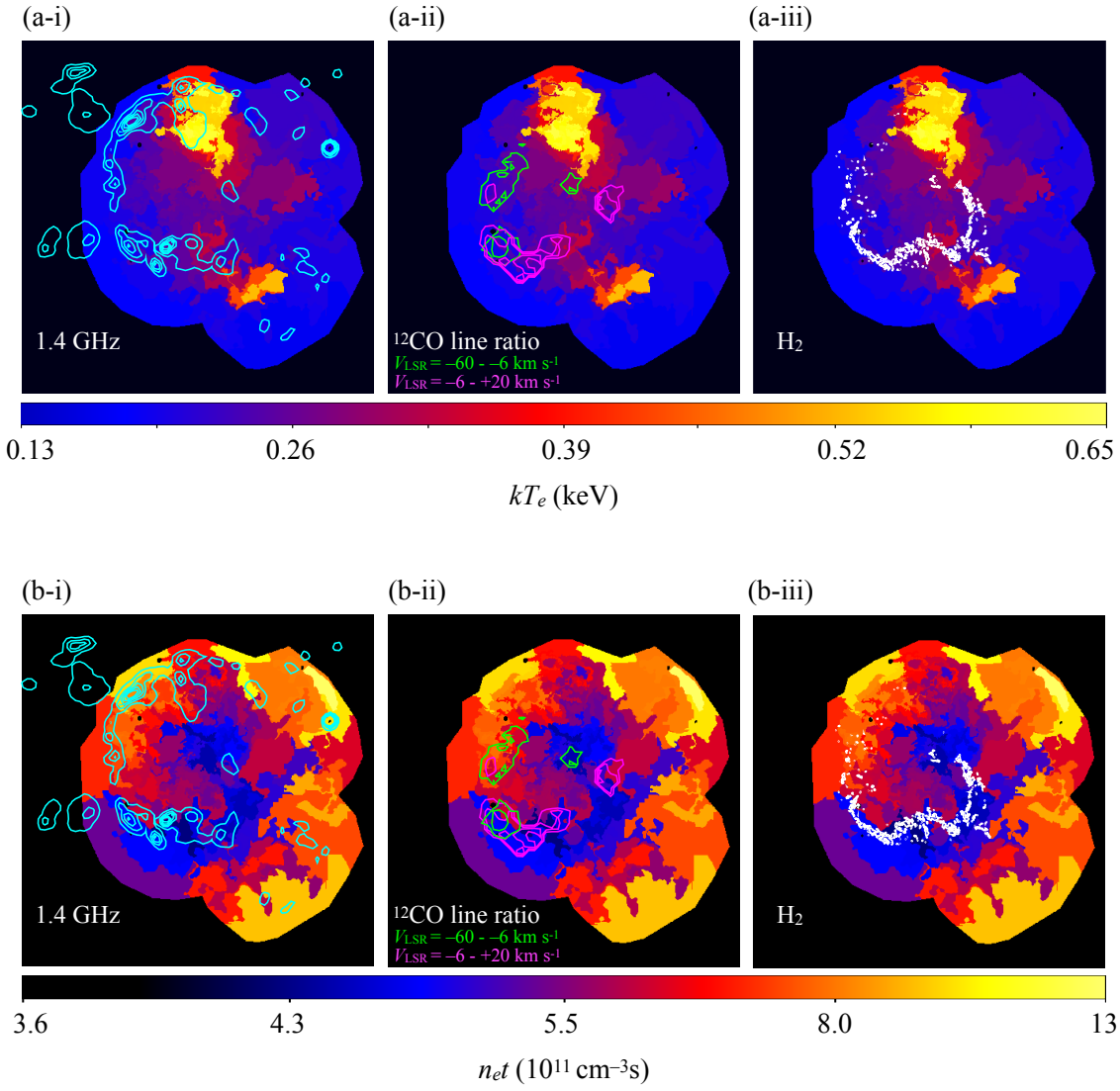

Figure 5.17: Maps presenting the distributions of (a) kT_e and (b) $n_e t$. The cyan contours in the panels (a-i) and (b-i) indicate the same radio continuum image as that in Figure 5.12(a). The green and magenta contours in panels (a-ii) and (b-ii) denote a ^{12}CO($J = 2$–1)-to-^{12}CO($J = 1$–0) intensity ratio map drawn every 0.8 from 1.0 in $V_{\rm LSR} = -6$–20 km s^{-1} and $V_{\rm LSR} = -60$–6 km s^{-1} taken from Yoshiike et al. (2013). In panels (a-iii) and (b-iii), the white contours denote H_2 1–0 S(1) lines taken with the near-IR camera Simultaneous Infrared Imager for Unbiased Survey installed on the InfraRed Survey Facility 1.4 m telescope (Kokusho et al., 2020).

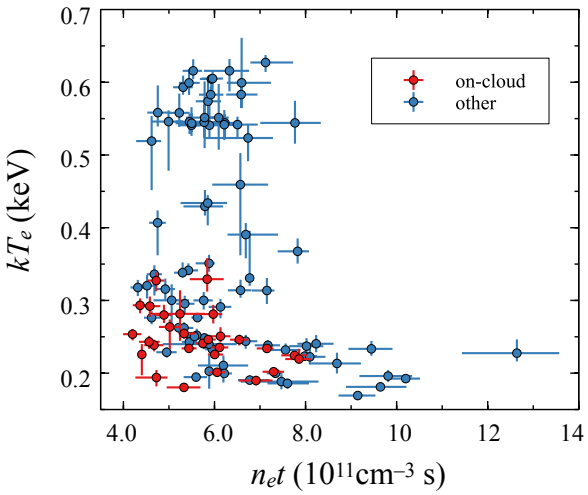

Figure 5.18: Plot of the values of the kT_e and $n_e t$. The red points are from the on-cloud region whereas the blue points are from the other regions.

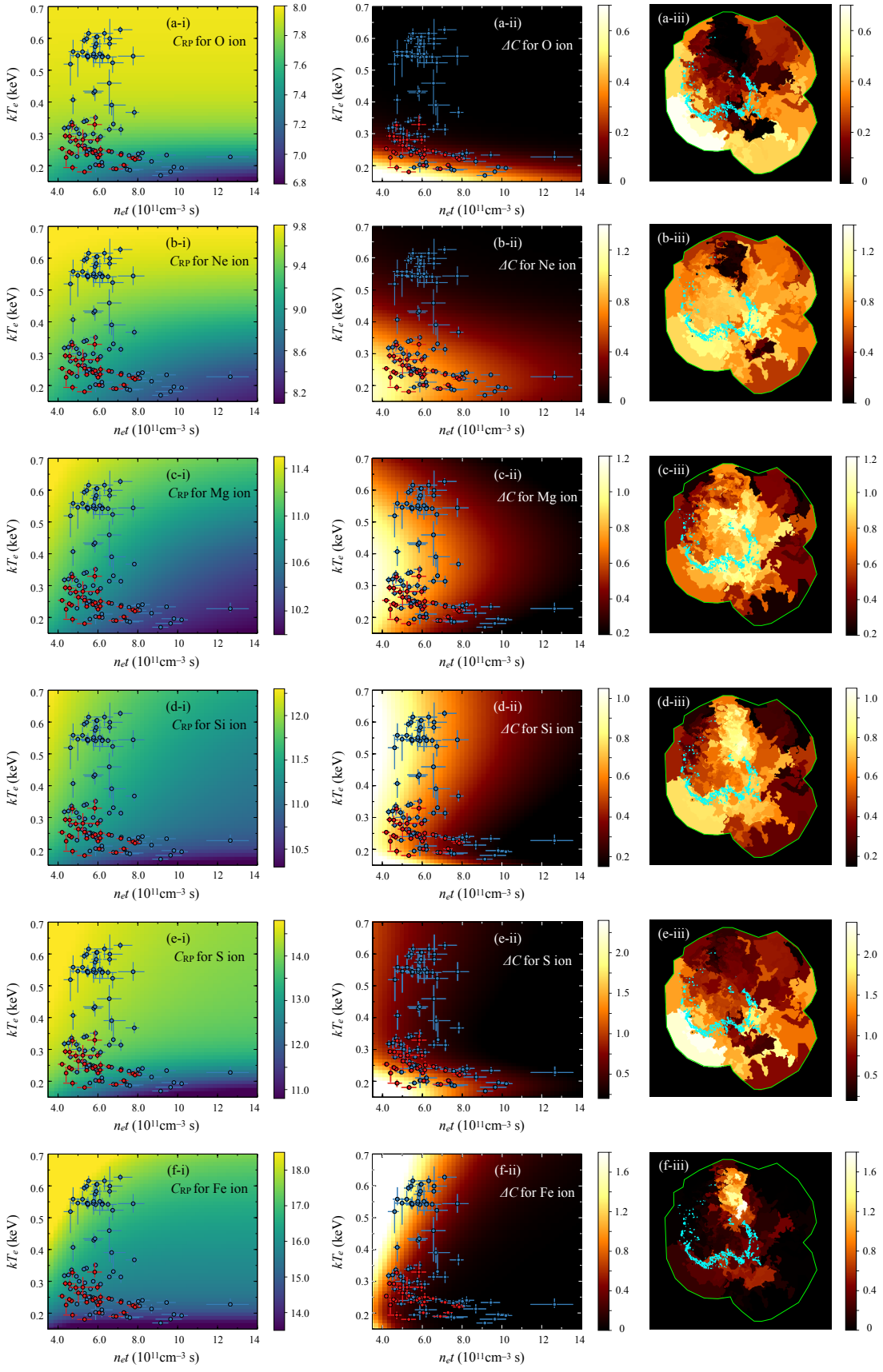

Figure 5.19: Average charge C_{RP} and charge deviation ΔC for O-Fe ions in the panels (a-i)-(f-i) and (a-ii)-(f-ii), respectively, shown on color scales. We overlay the same plot as that in Figure 5.18 on each map. In panels (a-iii)-(f-iii), maps of ΔC computed with best-fit values. The cyan contours denote the same radio H_2 image as that in Figure 5.17.

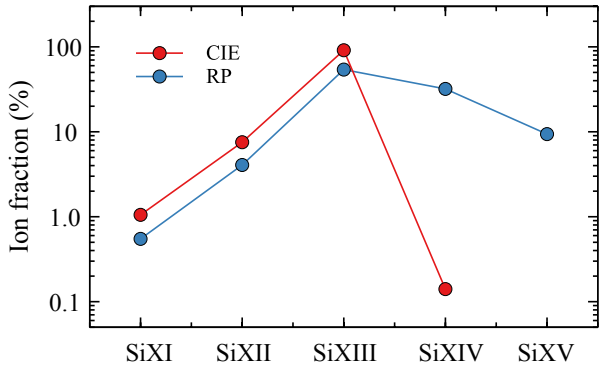

Figure 5.20: Si ion fraction in CIE plasma with kT_e=0.3 keV and RP with kT_e = 0.3 keV, $kT_{\rm init}$ = 5.0 keV, and $n_e t = 6.0\times10^{11}$ cm^{-3}s.

5.4 Discussion

Table 5.7: Comparison between three RP-SNRs, W44, IC 443, and W49B.

	W44	IC 443	W49B
Age (kyr)	$\sim$20[a]	$\sim$20–30[b]	$\sim$1–6[c]
kT_e (keV)	0.20–0.60	0.15–0.65	1.1–1.8[d]
kT_e-n_et correlation	Negative	Negative	Positive
Shock-cloud interaction	Entire	Local	Local
RPs near molecular clouds	Lower kT_e and n_et[e]	Lower kT_e and n_et	No correlation
Cooling process	Thermal conduction	Thermal conduction	Rarefaction

[a] Smith et al. (1985a), Wolszczan et al. (1991), and Harrus et al. (1997).
[b] Olbert et al. (2001) and Lee et al. (2008).
[c] Pye et al. (1984) and Smith et al. (1985b).
[d] Yamaguchi et al. (2018).
[e] Remarkable in the SEMBE region.

We discuss the comprehensive physical origin of RPs in SNRs based on our results and their comparison of other SNRs. Our results provided clear evidence for thermal conduction as the over-ionization in W44 and IC 443. Recent studies showed the same mechanism seems to be responsible for RPs in other SNRs as well: G166.0+4.3 (Matsumura et al., 2017a), W28 (Okon et al., 2018), and CTB 1 (Katsuragawa et al., 2018). A clear exception is W49B. Analyzing *NuSTAR* data of W49B, Yamaguchi et al. (2018) found a result opposite to this, a positive correlation between kT_e and n_et as shown in Figure 3.14. The correlation can be well explained by an efficient cooling by adiabatic expansion in low density areas. The result led Yamaguchi et al. (2018) to conclude that adiabatic expansion plays a predominant role in over-ionizing the plasma in W49B. What is a key to determining the thermal conduction scenario or the rarefaction scenario? Table 5.7 summarizes the observational characteristics of the W44, IC 443, and W49B. An important hint would be their age. Cooling through adiabatic expansion is expected to work efficiently in the early phase of SNR evolution when the blast wave breaks out of dense circumstellar matter into tenuous ISM (Itoh & Masai, 1989; Shimizu et al., 2012). On the contrary, thermal conduction can be effective only after the blast wave hits dense ambient ISM, and thus would be expected to be predominant at later stages. G166.0+4.3, W28, and CTB 1 whose thermal conduction is the most plausible formation process of RPs are much older (few 10 kyr) than W49B, supporting our interpretation. Based on hydrodynamical simulations, Zhang et al. (2019) reached a similar conclusion that both thermal conduction and adiabatic expansion contribute to plasma cooling in SNRs and that the dominant channel can be changed as SNRs evolve. Systematic observational studies as well as their comparison with theoretical and numerical studies are necessary to further clarify the over-ionization process in SNRs.

Chapter 6

Probing Sub-Relativistic Particles with the Neutral Fe Kα Line

6.1 Previous Works and Our Objective

6.1.1 Detection of Neutral Fe Kα Line

We detected enhanced neutral Fe Kα ($\sim$ 6.4 keV) line emission in the northeastern rim of the SNR W28 (Figures 3.12 and 6.1 1; region 1) (Okon et al., 2018). The line surface brightness is significantly higher than a level expected for GRXE (e.g., Yamauchi et al., 2016), which also emits the neutral Fe Kα line. We, therefore, conclude that most of the neutral Fe Kα line emission can be attributed to W28, not to the GRXE. One possible origin of this line is thermal emission from the remnant, however, it is less plausible because W28 is one of the middle-aged and core-collapse SNRs, from which Kα lines of nearly-neutral Fe generally are not expected (Yamaguchi et al., 2014). Interestingly, this region corresponds to the locations where the shock is interacting with a molecular cloud. An alternative possibility is thus that the enhanced natural Fe Kα line emission is generated by K-shell ionization of Fe in the cloud by accelerated particles. GeV and TeV gamma rays also detected there indicate that the cloud is bombarded by particles accelerated in W28 if π^0 decay is the gamma-ray production mechanism as duscussed by Abdo et al. (2010) and Aharonian et al. (2008) (Figure 6.2). The fact supports our interpretation of the origin about the neutral Fe Kα line.

In addition to the example of W28, *Suzaku* data recently revealed the presence of the enhanced neutral Fe Kα line emission in some SNRs interacting with dense clouds: i.e., W44: Nobukawa et al. (2018); G323.7$-$1.0: Saji et al. (2018). In most cases, the line emission spatially coincides with dense gas in the vicinity of the SNRs as shown in Figure 6.3. Since the cross section of the neutral Fe Kα production peaks at $\sim$ 10 MeV and $\sim$10 keV for protons and electrons, respectively (Dogiel et al., 2011), the observed line emission would be emitted by sub-relativistic particles regardless of the particle species. These results suggest that the neutral Fe Kα line emission, along with bremsstrahlung continuum as demonstrated by Tanaka et al. (2018), would work as a diagnostic tool to study largely unknown sub-relativistic particles.

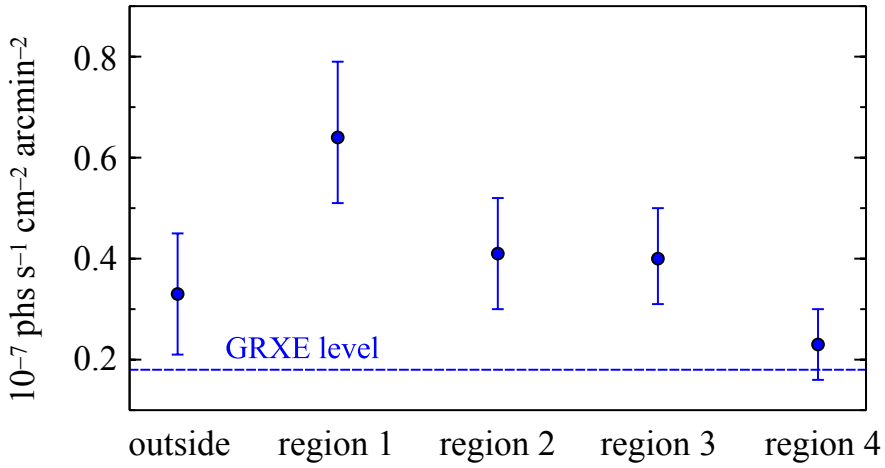

Figure 6.1: Intensities of the neutral Fe Kα line line of the five regions (Figure 3.12) in W28 (Okon et al., 2018). The horizontal dashed lines indicate the GRXE level expected by a phenomenological model in Yamauchi et al. (2016).

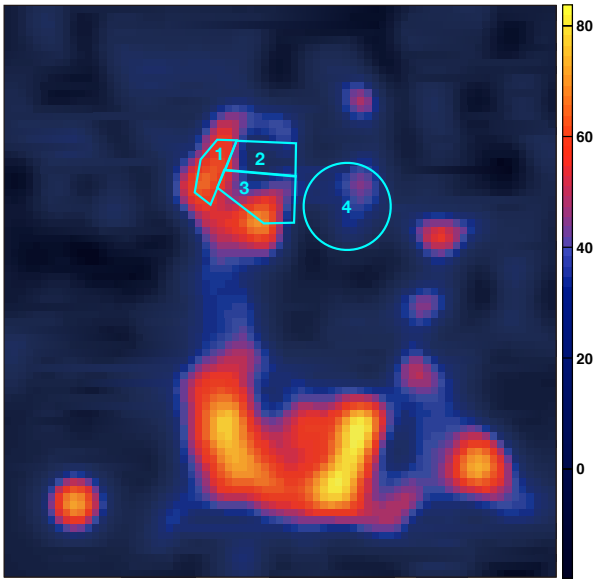

Figure 6.2: H.E.S.S. gamma-ray map ($>$ 0.1 TeV) (Aharonian et al., 2008). The cyan lines indicate the same regions as in Figure 3.12.

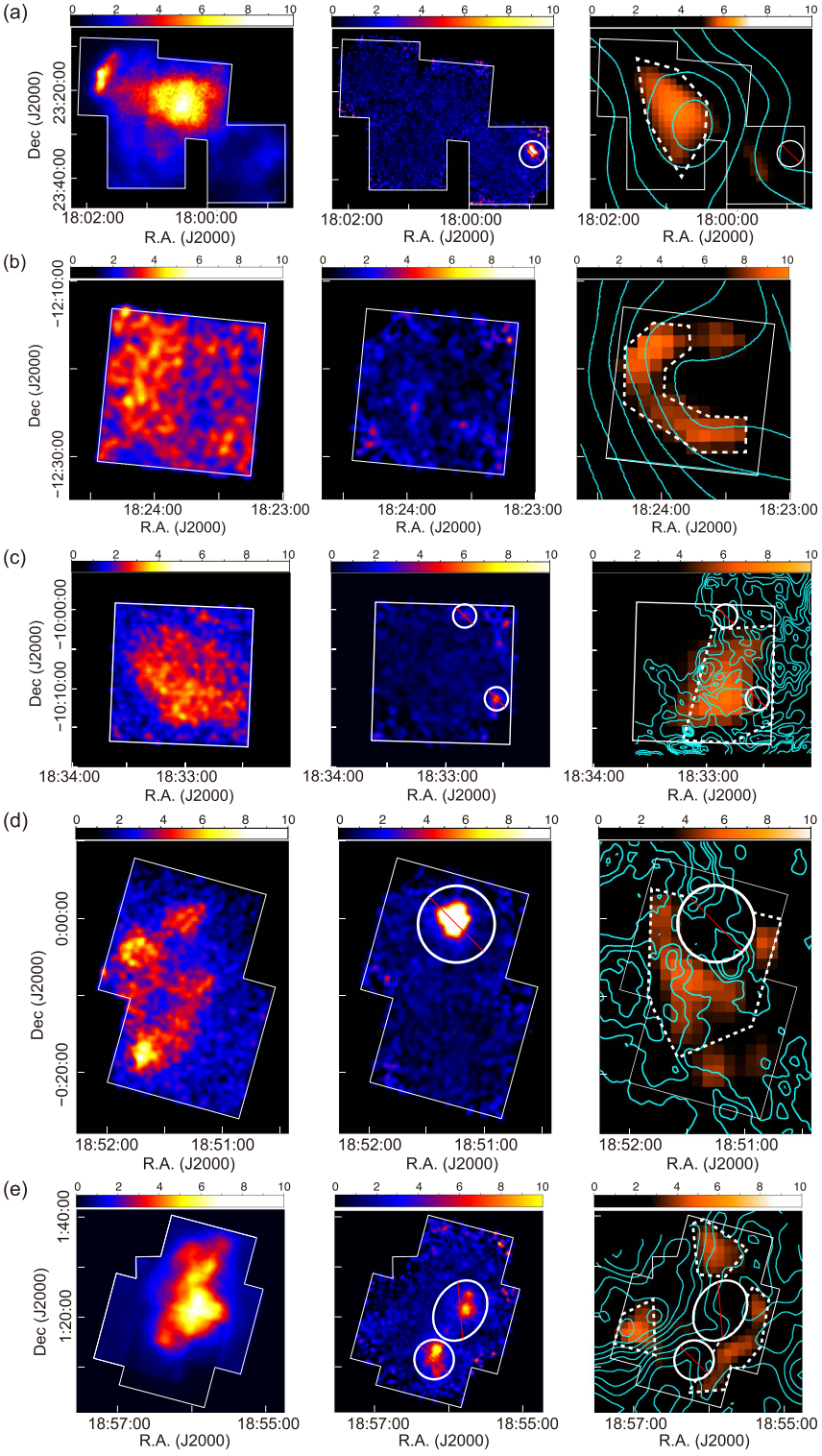

Figure 6.3: Band images of (a) W28, (b) Kes 67, (c) Kes 69, (d) Kes 78, and (e) W44. The left, center, and right panels correspond to the soft band (0.5–2 keV), the hard band (5–8 keV), and the Fe-K (6.2–6.5 keV) band that covers the neutral Fe Kα line (6.4 keV), respectively. Vignetting is corrected and the instrumental background is subtracted. Point-like and slightly extended sources are marked with the solid lines. In the right panels, those regions are excluded from the images. The cyan contours in the right panels show the gas distributions. (taken from Nobukawa et al., 2018).

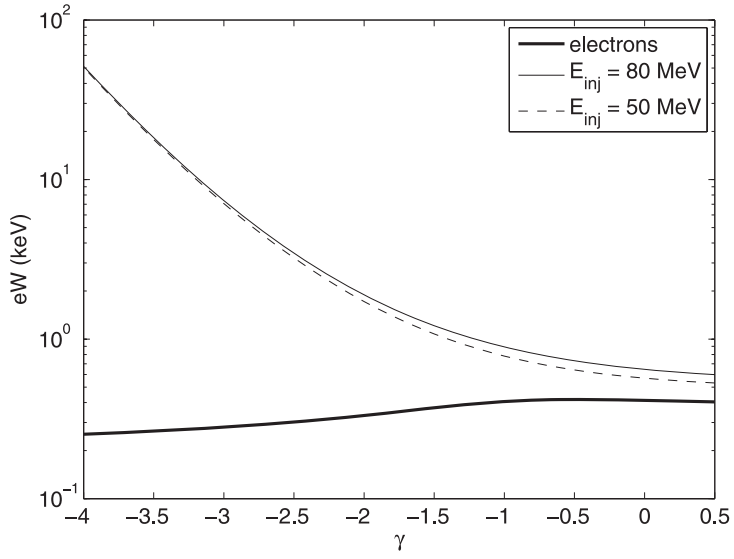

Figure 6.4: Equivalent width of the Fe Kα line produced by sub-relativistic particles as a function of their spectral index. The thick solid line indicates electron case. The thin solid and dashed curves represent proton case for injection energy $E_{\rm inj}$ = 80 MeV and $E_{\rm inj}$ = 50 MeV, respectively. (taken from Dogiel et al., 2011)

6.1.2 Neutral Fe Kα line as a Diagnostic Tool to Study Sub-Relativistic Particles

Information on accelerated sub-relativistic particles can be exploited using the neutral Fe line emission. Dogiel et al. (2011) proposed an idea that species of radiating particles can be distinguished based on the equivalent width of the Fe line with respect to a non-thermal bremsstrahlung continuum from the same population of particles. In Figure 6.4, we show the equivalent widths for protons and electrons as functions of their spectral indices. Using the idea, Nobukawa et al. (2018), Nobukawa et al. (2019), and Saji et al. (2018) claimed that protons account for the majority of the Fe line emission in some SNRs. Makino et al. (2019) presented an analytical model in which they consider energy-dependent escape of CRs from an SNR shock into an interacting cloud, and calculated emission spectra from the cloud, i.e., Fe line emission from sub-relativistic protons and π^0-decay emission from relativistic protons. Applying their model to W44 and W28, they successfully reproduced both the observed Fe line emission intensity and the gamma-ray spectra.

Fine structures of the Fe Kα line, if detected, can make another step forward in the study of sub-relativistic particles accelerated in astrophysical objects. Tatischeff et al. (2012) pointed out that the electron transfer process from ambient neutral atoms to fast heavy ions can produce broad line structures accompanying narrower K-shell lines. Figure 6.5 shows the line structures, which are sums of transition lines from captured electron, broadened mainly by the Doppler effect of the fast moving ions. Detection of such structures would allow us to prove the presence of heavy ions in accelerated particles and to constrain their composition. Apart from electron transfer, multiple ionization, which is the topic of this dissertation, is another potentially important process caused by accelerated heavy ions, and thus can be a powerful diagnostic tool to probe accelerated particles.

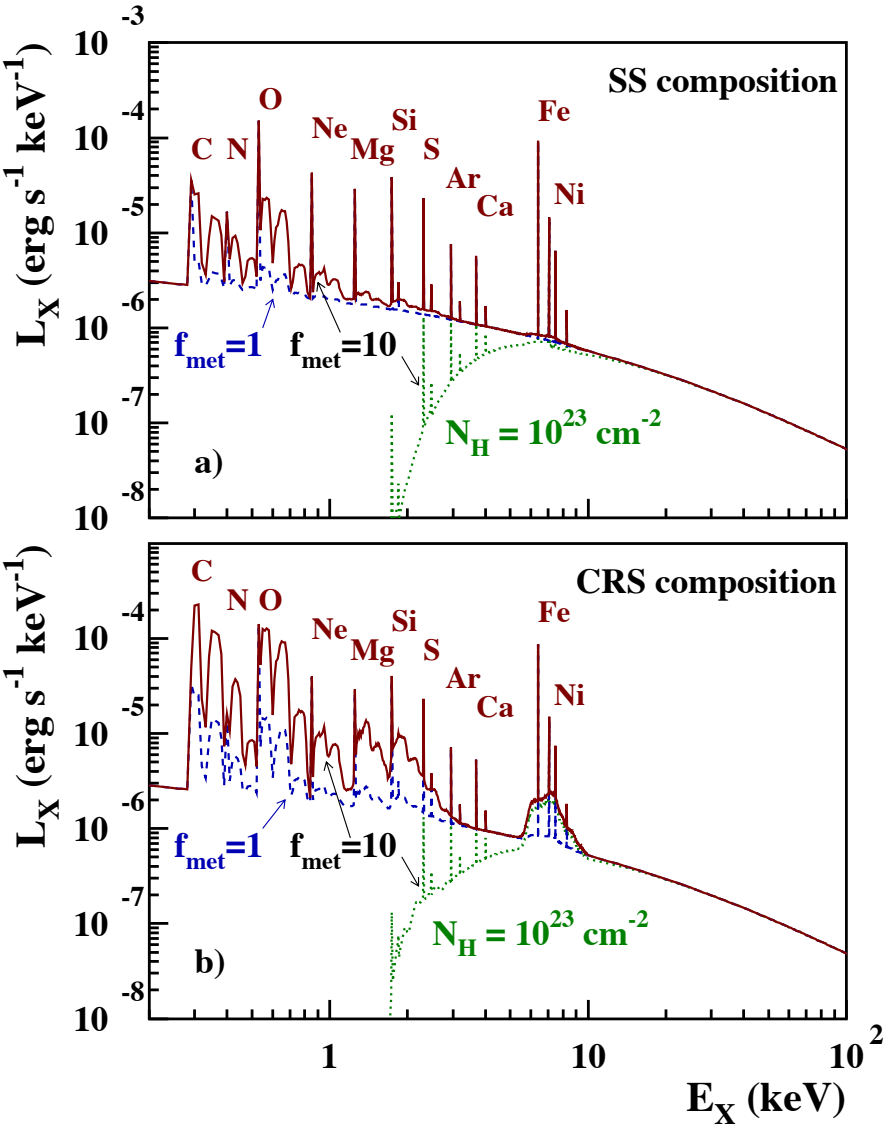

Figure 6.5: (a) Calculated X-ray emission produced by sub-relativistic particles interacting with a dense cloud. The dashed and solid curves represent the models by the particles with the solar system composition, and with 10 times metallicity relative to the solar composition. (b) Same as the above figure but for the cosmic ray source composition from Engelmann et al. (1990) and Meyer et al. (1997) (taken from Tatischeff et al., 2012).

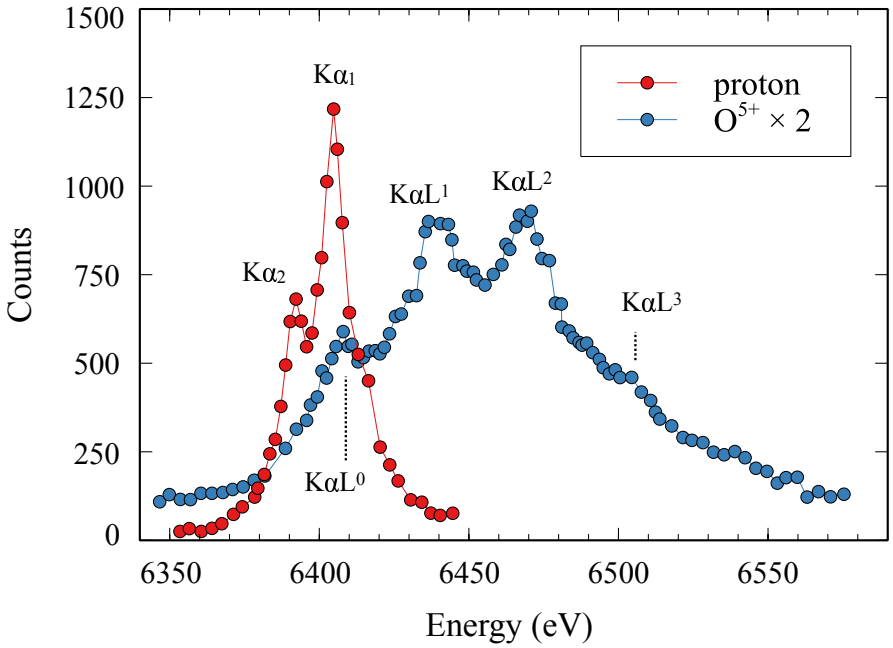

Figure 6.6: Fe Kα spectra produced by impacts of protons (red), and O^{5+} ions (blue) (data from Burch et al., 1971). For a display purpose, the O^{5+} spectrum is scaled by a factor of two.

In this thesis, we qualitatively estimate the effect of the multiple ionization process on the Fe Kα line emission. We calculate a model to predict line structures due to multiple ionization by using the knowledge from beam experiments. Based on our model, we show Fe Kα line structures expected to be detected in SNRs by high resolution X-ray spectroscopy with future X-ray satellites such as *XRISM* and *Athena*.

6.2 Multiple Ionization Processes in Collisions of Ion-Atom

Ionization of target atoms by projectile ions have been widely studied through both experimental and theoretical approaches. With studies by high-resolution crystal spectrometers, authors such as Burch et al. (1971) and Kauffman et al. (1973) found differences of line structures between proton- and ion-produced Kα spectra. Figure 6.6 shows spectra of Fe Kα line structures originally presented by Burch et al. (1971). The proton-produced spectrum has only the neutral Fe Kα_1 and Fe Kα_2 lines due to the K-L_3 and K-L_2 transitions, respectively. The O^{5+}-produced spectrum, on the other hand, has broad line-like structures in the 6350–6550 eV band. When projectile particles are heavy ions, their strong Coulomb field can easily cause simultaneous ejection of multiple inner-shell electrons of the targets, resulting in the significant characteristic structures.

The multiple ionization structures consist of peaks called KαL^i (i = 0–7), each of which is superposition of the K-L_3 and the K-L_2 transition lines from ionized Fe atoms with i L-shell vacancies as shown in Figure 6.7. The center energies of the KαL^i peaks are higher by $\sim i \times$ 20–30 eV than those of the Fe Kα_1 and Kα_2 lines. This is because the K-L_3 (K-L_2) transition lines shift upwards by $\sim$ 20–30 eV per L-shell electron ionization ($= \Delta E_{\rm L}$) (e.g., Wang et al., 2012). The outer shell (M, N, ...) ionization is mainly manifested in broadenings of the KαL^i peaks because the energy shift $\Delta E_{\rm M}$ (and $\Delta E_{\rm N}$, ...) of the transition lines due to additional M-shell

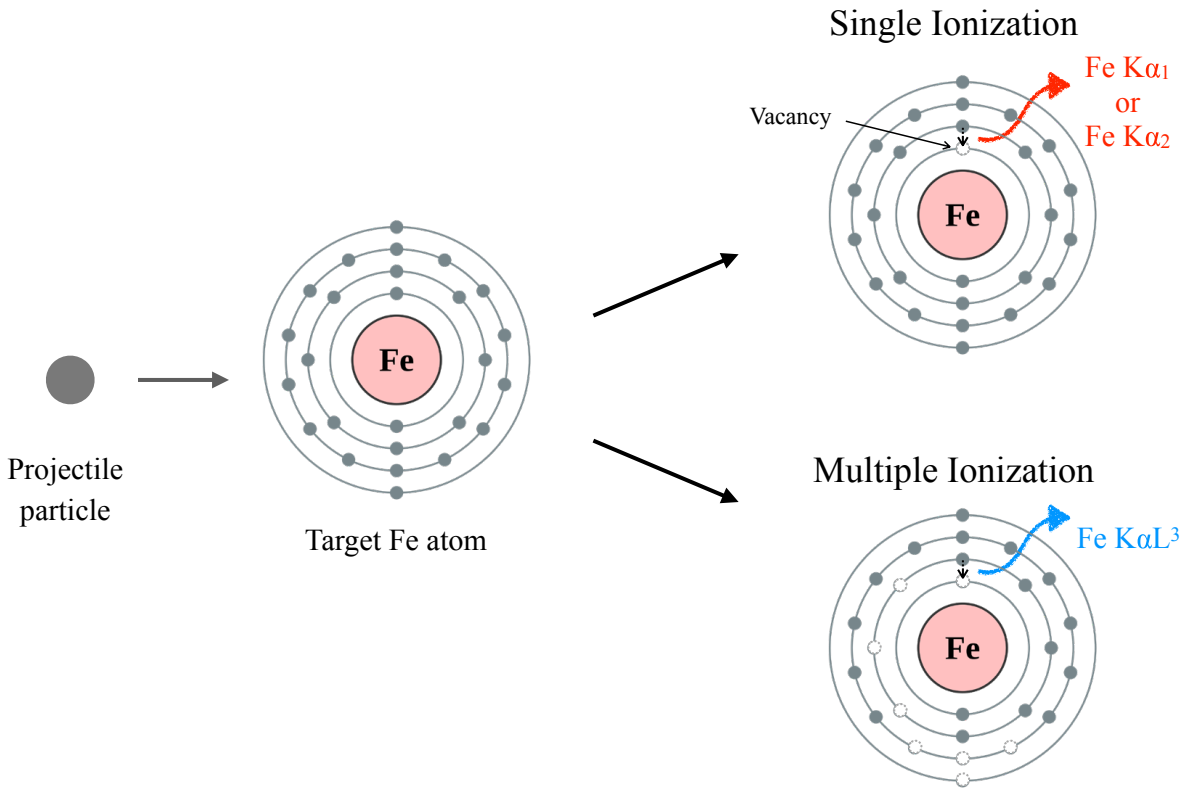

Figure 6.7: Schematic view of ionization process in collisions of ion-atom.

and outer shell vacancies are sufficiently smaller than ΔE_{L}, and is equal to or smaller than the natural widths of the transition lines.

6.3 Modeling of Kα Lline Structures by Impacts of Mono-energetic Ions

6.3.1 Kα Line Structures

The KαL^i peaks are the sums of the Kα_1L^i and Kα_2L^i sub-peaks, which are superpositions of the K-L$_3$ and K-L$_2$ transition lines, respectively. The Kα_1L^i (Kα_2L^i) sub-peaks are expressed as superpositions of Lorentzians corresponding to transition lines. According to Horvat et al. (2006) and Horvat et al. (2009), KαL^i spectra obtained in ion beam experiments can phenomenologically be reproduced by the sums of the Kα_1L^i and Kα_2L^i peaks described by Voigt functions, or a convolution of a Lorentzian and a Gaussian. Figure 6.8 shows one example from Horvat et al. (2006). Here, the Gaussian reflects broadening of the sub-peaks due to simultaneous ionization of electrons in outer shells. Taking the same approach, we modeled the Kα_1L^i and Kα_2L^i sub-peaks with the Voigt function.

We calculate the center energy of the sub-peaks with the scaling law given by Horvat et al. (2006). They expressed the energy shift ΔE^i(eV) of each Kα_1L^i (Kα_2L^i) sub-peak with respect to the neutral Kα_1 (Kα_2) line emission based on various data obtained by ion beam experiments.

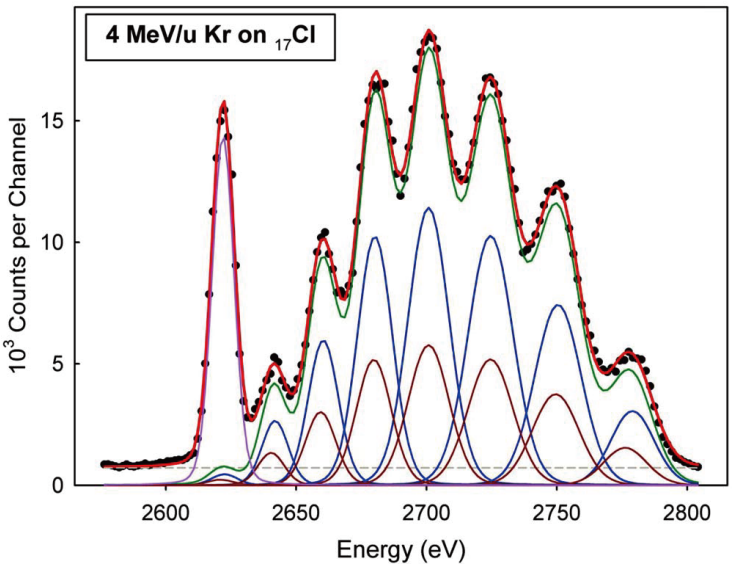

Figure 6.8: Spectrum of Cl Kα line emitted from thick KCl targets bombarded by 4 MeV/amu Kr ions obtained by a crystal spectrometer. The green, blue and brown curves represents the best-fit fit model for each Kα_1L^i line, and the contributions from Kα_1 and Kα_2 lines, respectively. The gray and magenta lines indicate instrumental background and the Kα line generated by secondary electrons. The red line shows the sum of all components. (taken from Horvat et al., 2006)

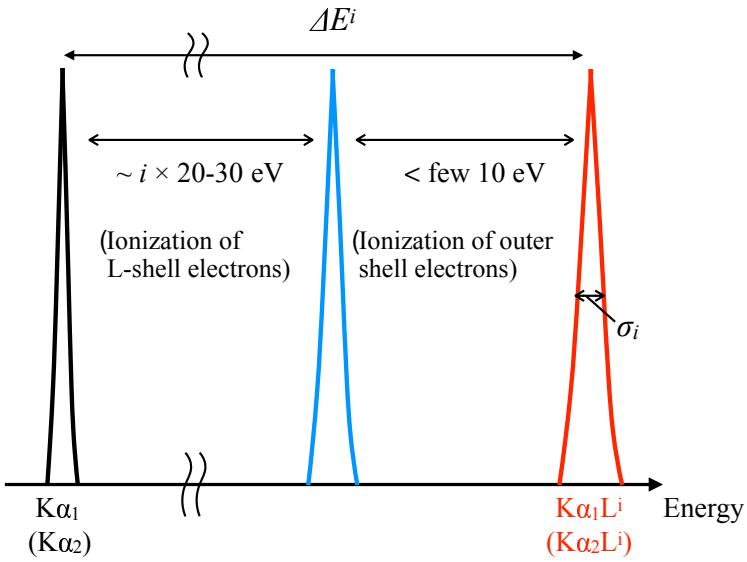

Figure 6.9: Energy shift of Kα line due to multiple ionization. The black and red curves represent Kα_1 (Kα_2) line, and Kα_1L$_0^i$ (Kα_2L$_0^i$) line from ions with single K-shell and i L-shell vacancies, respectively. The blue and red lines indicates Kα_1L^i (Fe Kα_2L^i) sub-peaks.

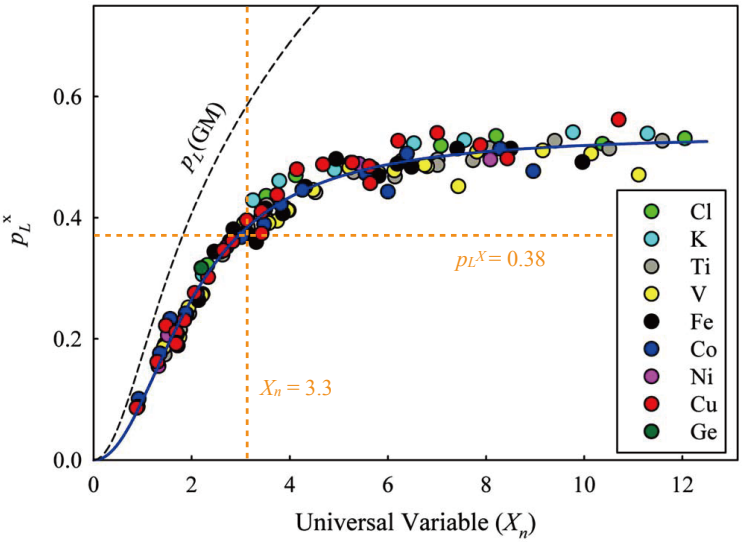

Figure 6.10: Ionization parameter p_L^X as a function of the universal variable X_n determined using Equation 6.3 for $n = 2$ (Horvat et al., 2006). The data points represent measurements with solid targets with $Z_2 = 17$–32 and projectile ions with $Z_1 = 6$–83 at 2.5–25 MeV/amu. The solid and dashed curves show the best-fit logistic model and a curve predicted by the Geometrical Model (e.g., Sulik et al., 1987), respectively. The orange dash lines denote the values of p_L^X and X_2 in the impacts of Fe^{26+} ions (10 MeV/amu) on Fe targets calculated with Equations 6.2 and 6.3.

The energy shift ΔE^i can be described as

$$\Delta E^i = i(a + bZ_2 + ci + diZ_2) + p_L^X[(i-1)(Z_2 - e) + f] \text{ eV}, \tag{6.1}$$

where $a = -11.64$, $b = 1.493$, $c = 0.755$, $d = -0.0112$, $e = 9.11$, $f = 14.3$, and Z_2 is the atomic number of the target. The first and second terms in Equation 6.1 correspond to the energy shifts due to ionization of L-shell and outer shell electrons, respectively, as shown in Figure 6.9. The parameter p_L^X is the ionization probability per L-shell electron in K-shell ionization. We calculate the p_L^X with the model by Horvat et al. (2006),

$$p_L^X = a'/[1 + (b'/X_2)^{c'}], \tag{6.2}$$

where $a' = 0.537$, $b' = 2.11$, and $c' = 2.02$. The parameter X_2 is a universal function derived by Sulik et al. (1987), and is described as

$$X_2 = 4V[G(V)]^{1/2} Z_1/(2v_1), \tag{6.3}$$

where v_1, Z_1, V, and $G(V)$ are the projectile velocity in atomic units, where is normalized to the Bohr velocity 2.18×10^6 m/s, the atomic number of the projectile, the ratio of v_1 to the average velocity of electrons in target atoms, and the Gryzinski Geometrical factor, respectively. We employ an analytical formula in McGuire & Richard (1973) for $G(V)$.

We then calculate the widths of the sub-peaks, which correspond to the parameter σ^i in Figure 6.9. The scaling law by Horvat et al. (2006) approximates the widths of the Gaussian of the Voigt function as

$$\sigma^i = a\,i(b - i)(Z_2 - c) \text{ eV}, \tag{6.4}$$

where $a = 0.0246$, $b = 9.86$, and $c = 10.40$. Following Horvat et al. (2006), we fix the line width of the Lorentzian component to the natural widths of the transition lines obtained by Campbell & Papp (2001).

The above scaling laws by Horvat et al. (2006) are derived from experimental data using a variety of solid targets with $Z_2 = 17$–32 and projectile ions with $Z_1 = 6$–83 at 2.5–25 MeV/amu. In Figure 6.10, we show the plot of the values of X_2 and p_L^X of the used data (Horvat et al., 2006), and overlay the values in the impacts of Fe^{26+} ions on Fe targets. The X_2 of each data is calculated with Equation 6.3, and the p_L^X is calculated with the intensity I_i of $K\alpha_1 L^i$ ($K\alpha_2 L^i$) sub-peak obtained by the data and $p_L^X = \sum_i i I_i / I_{tot}$ derived from Equation 6.5, respectively. The values of the Fe^{26+} impacts are calculated with Equations 6.3 and 6.2. The data cover impacts by various ions with ~ 10 MeV/amu, where the cross sections for K-shell ionization of Fe atoms (Z_2) peak. We applied the scaling laws to the calculation of the Fe line structures generated by impacts of various ions in 0.5–1000 MeV/amu region, where collision nature is well described by the perturbation theory and the scaling laws by Horvat et al. (2006) can be considered valid.

6.3.2 Intensity of $K\alpha L^i$ Line

The intensity of each $K\alpha_1 L^i$ ($K\alpha_2 L^i$) sub-peak can be expressed as a function of p_L^X. Under an assumption of independent L-shell electron ionization, a binomial distribution of

$$I_i = I_{tot} \binom{8}{i} p_L^{X\,i} (1 - p_L^X)^{8-i}, \tag{6.5}$$

where

$$I_{tot} = \sum_i^8 I_i, \tag{6.6}$$

gives a good description of the relative intensities of the $K\alpha L^i$ peaks (Kauffman et al., 1973).

According to Horvat et al. (2009), intensities of the $K\alpha L^i$ peaks depend on the phase of the target, whether it is gas or solid. Compared to the solid target case, the Fe $K\alpha L^i$ peaks become dominant with gaseous targets. Horvat et al. (2009) derived the scaling law of p_L^X similar to the equation (6.2) from atomic data of collisions between various ions at ~ 10 MeV/amu and monoatomic Ar gas. The scaling law for gas is the same as equation (6.2), but with $a' = 0.856$, $b' = 2.94$, and $c' = 1.71$.

6.3.3 Comparison between Our Model and Experimental Data.

In Figure 6.11, we plot the models for the $K\alpha$ line emitted by solid Fe bombarded by protons and fully ionized O and Fe ions. Figure 6.12 is the same but for gaseous Fe. The results clearly indicate that the intensities of the $K\alpha L^i$ peaks depend on the charge state and kinetic energy of the projectiles. The larger charge the projectile has, the more significant the $K\alpha L^i$ peaks become. This is naturally explained by a stronger Coulomb field of heavy ions. Regardless of the projectile species, the Fe $K\alpha L^i$ peaks are the most significant when the projectile kinetic energy is ~ 1.6 MeV/amu. Electrons generally are ejected most efficiently when the projectile ion velocity matches the average velocity of the electrons in orbit of an atom (Bohr, 1948). Since the kinetic energy of ~ 1.6 MeV/amu is translated into a projectile velocity close to that of Fe-L electrons, L-shell electrons are efficiently ionized around this energy.

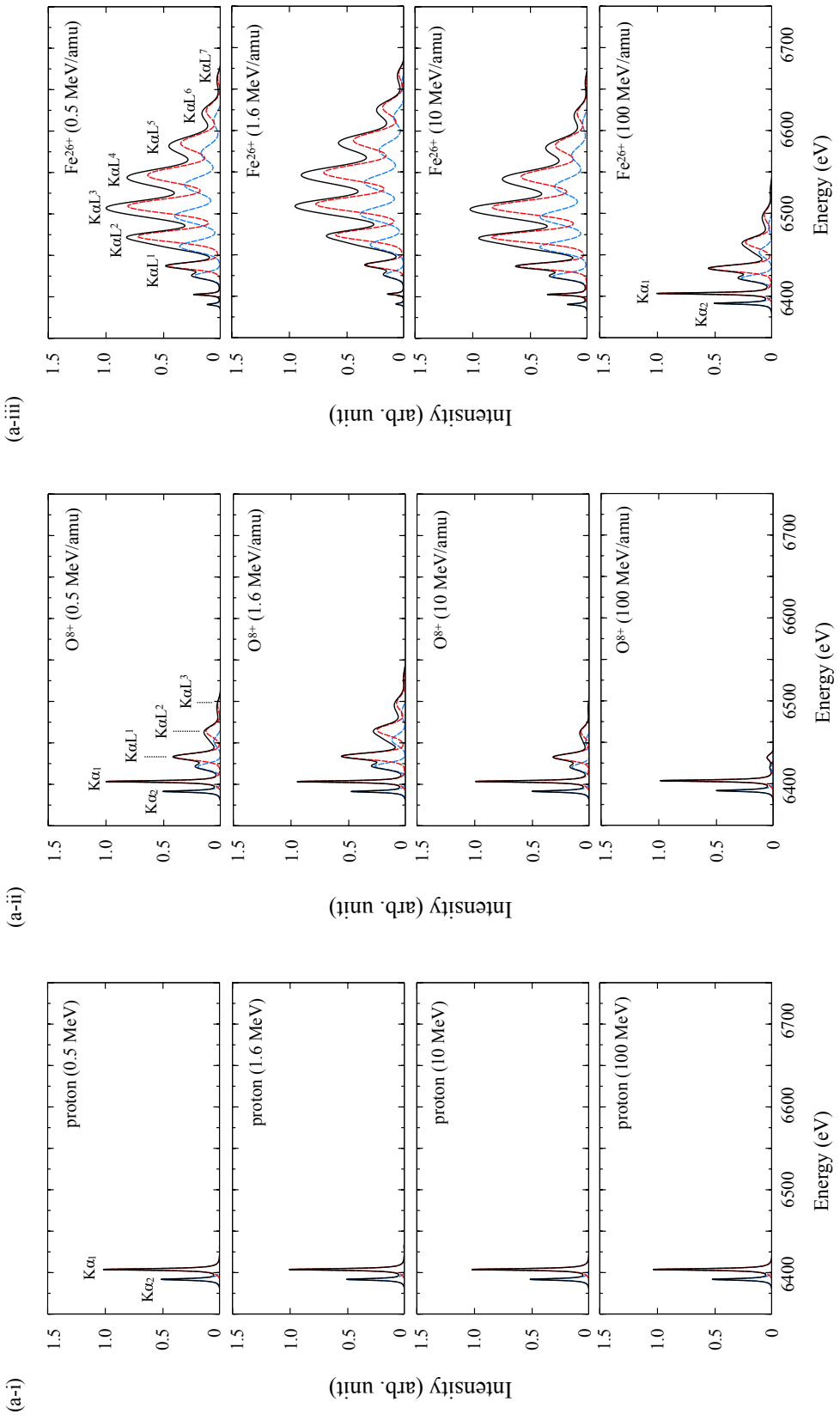

Figure 6.11: Fe Kα structures emitted from (a) solid and (b) gaseous Fe targets under bombardment by (i) protons, (ii) O^{8+}, and (iii) Fe^{26+} ions. The red and blue dashed curves denote the Fe Kα_1 and Fe Kα_2 structures, respectively.

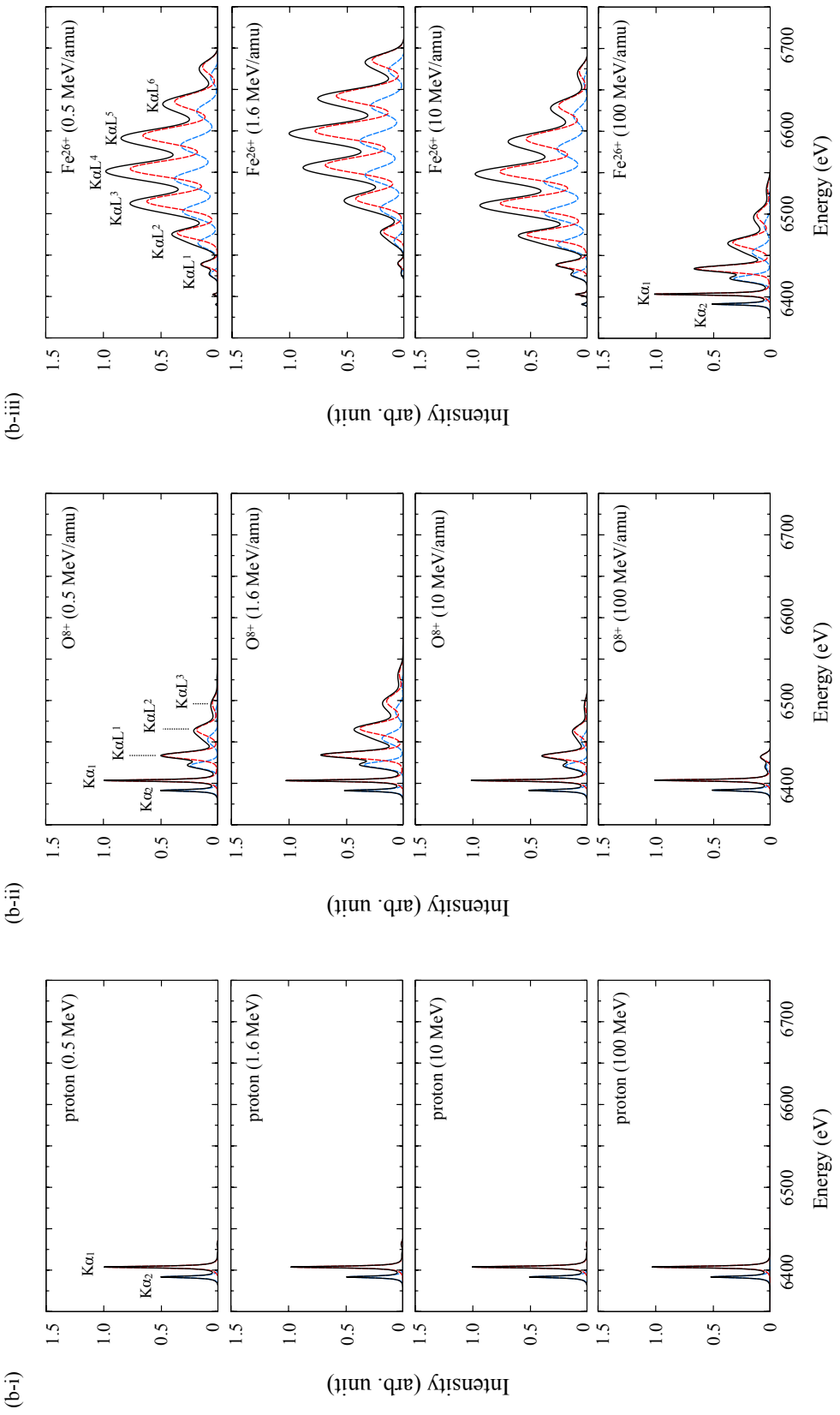

Figure 6.12: Same as Figure 6.11 but for gas Fe targets.

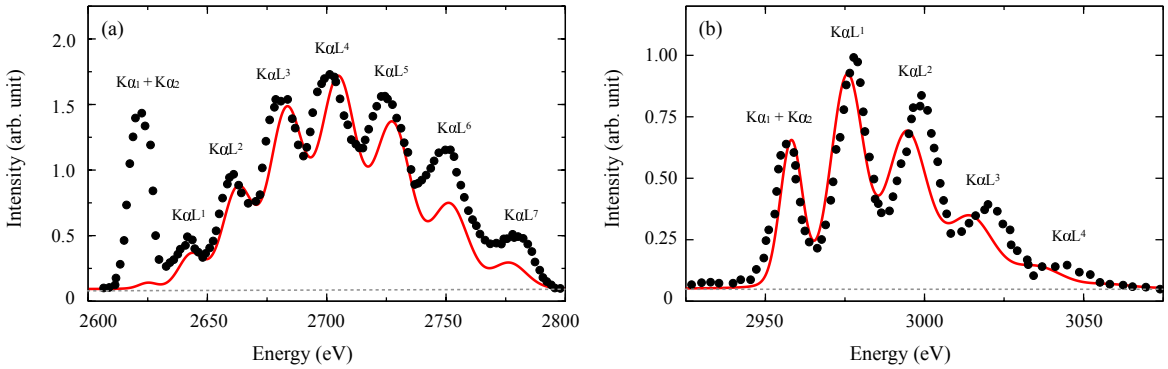

Figure 6.13: (a) Cl Kα spectrum from solid KCl targets under bombardment by 4 MeV/amu Kr^{36+} ions (Horvat et al., 2006) and (b) Ar Kα spectrum from a gaseous Ar target under bombardment by 9.4 MeV/amu Ne^{10+} ions (Horvat et al., 2009) from experiments (the black dots), compared with our model (the red curves). The gray dashed curves represent the background.

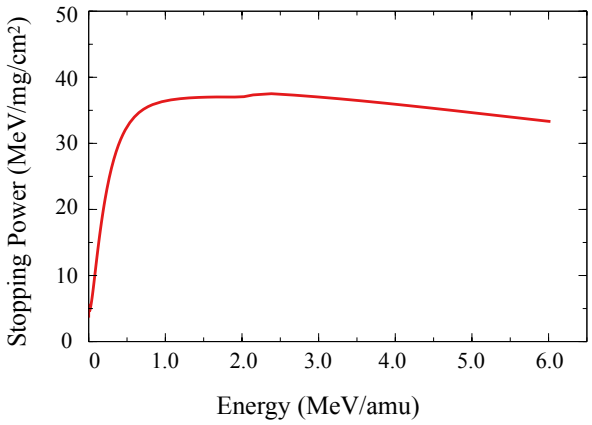

Figure 6.14: Stopping power for projectile Kr ion in solid KCl targets. Electronic and nuclear stoppings are considered (data from Dr. M. Imai).

Figure 6.13 shows a comparison between the computed models and experimental data by Horvat et al. (2006) and Horvat et al. (2009). In the experimental data, the $K\alpha L^i$ peaks (i = 0–7) are generated by impacts of projectile ions, while the $K\alpha_1$ and $K\alpha_2$ lines in Figure 6.13(a) are mainly induced by secondary electrons and X-rays not included in our model. Our model reproduces the overall $K\alpha L^i$ peaks structures. However, we found some discrepancies of the line center energies and intensities. The contradiction about the center energy could be explained by the inaccuracy of Equations 6.1, 6.2, and 6.4, which is estimated to be at a few % level by Horvat et al. (2006). The discrepancy of the intensities could be brought by continuous changes of energy and charge state of projectile ions in thick ($\sim$ mg cm^{-2}) targets, which change the value of p_L^X. In Figure 6.14, we show the stopping power for Kr ions in KCl targets. The combination of projectile ions and targets is the same as the case in Figure 6.13(a). Another possibility would be contribution of electron captures from the L-shell of the target atoms in L-shell vacancy production as Rymuza et al. (1989) and Kavčič et al. (2000) pointed out. Those effects are not included in the present model.

6.4 Fe Kα Structures Produced by Cosmic Rays

6.4.1 Assumptions

Using our model, we compute Fe Kα line spectra expected to be observed in SNRs. In SNR shocks, various ions would be accelerated at the same time, and thus the spectra would be superpositions of contributions from each ion species. Since the composition of cosmic rays at acceleration sites is unknown, we assume here that it is the same as that observed in the solar system by referring to Mewaldt (1994). We also assume that ions are fully ionized and that all ions follow a common spectrum. We take into account contributions from H, He, ..., Fe, Co, and Ni ions in an energy range of 0.5–1000 MeV/amu.

The flux of the Fe KαL^i peak F_i by each ion species can be described as

$$F_i \propto n_{\rm gas} \int \sigma_{\mathrm{KL}^i} v_{\rm ion} \frac{dN_{\rm ion}}{dE} dE, \tag{6.7}$$

where $n_{\rm gas}$, σ_{KL^i}, $v_{\rm ion}$, and $dN_{\rm ion}/dE$ are the number density of Fe atoms in the dense gas, the production cross section of the Fe KαL^i peak, the velocity of the ions, and the differential spectra of the ions, respectively. We applied the scaling laws for solid targets assuming that Fe is mainly in dust grains. Based on Equations 6.5 and 6.6, the production cross section σ_{KL^i} can be calculated as

$$\sigma_{\mathrm{KL}^i} = \sigma_{\rm p} \binom{8}{i} p_L^{X\,i} (1 - p_L^X)^{8-i}, \;\; \sigma_{\rm p} = \omega_{\rm K} \times \sigma_{\rm ion}, \tag{6.8}$$

where $\sigma_{\rm p}$, $\sigma_{\rm ion}$, and $\omega_{\rm K}$ are the production cross section of the Fe Kα (=$\sum_i$ Fe KαL^i peaks) line, the K-shell ionization cross section, and the florescence yield (= 0.34) (Krause, 1979), respectively. We computed $\sigma_{\rm ion}$ with the program by Batič et al. (2013) based on the ECPSSR (Energy-Loss Coulomb-Repulsion Perturbed-Stationary-State Relativistic) theory (Brandt & Lapicki, 1981).

6.4.2 Results

Figure 6.15 presents the result, where the models are folded with the response of the X-ray micro-calorimeter Resolve (Ishisaki et al., 2018) aboard XRISM (Tashiro et al., 2018). Accelerated ions have a power-law spectrum $dN/dE \propto E^{-s}$ with $s = 1$ and $s = 2$ in the panels (a) and (b), respectively. The former is chosen, referring to the measurement of non-thermal bremsstrahlung in W49B by Tanaka et al. (2018). The latter is the index expected in diffusive shock acceleration at a strong shock. In both cases, the KαL^i (i = 1–7) peaks appear in the 6420–6700 eV band. The intensities of each KαL^i peak strongly reflect the composition of the emitting particles. If particles accelerated in SNRs have a similar ion composition to CRs arriving at the solar system, the most significant peak is the KαL^1 peak, which can be resolved into Kα$_1\mathrm{L}^1$ and Kα$_2\mathrm{L}^1$ with the Resolve. The intensities of the two sub-peaks are $\sim 1/10$ of those of Kα$_1$ and Kα$_2$. The Fe Kα$_1\mathrm{L}^1$ and Kα$_2\mathrm{L}^1$ sub-peaks are shifted by ~ 30 eV with respect to the Fe Kα$_1$ and Kα$_2$.

An $\sim$ eV energy resolution by X-ray micro-calorimeters would be necessary to resolve the structures. In addition to *XRISM*, future missions such as Athena (Barcons et al., 2017) and Super DIOS (Ohashi et al., 2018) with X-ray micro-calorimeters will able to detect the line structures. Such studies will play a complimentary role to CR-ionization rate estimates based

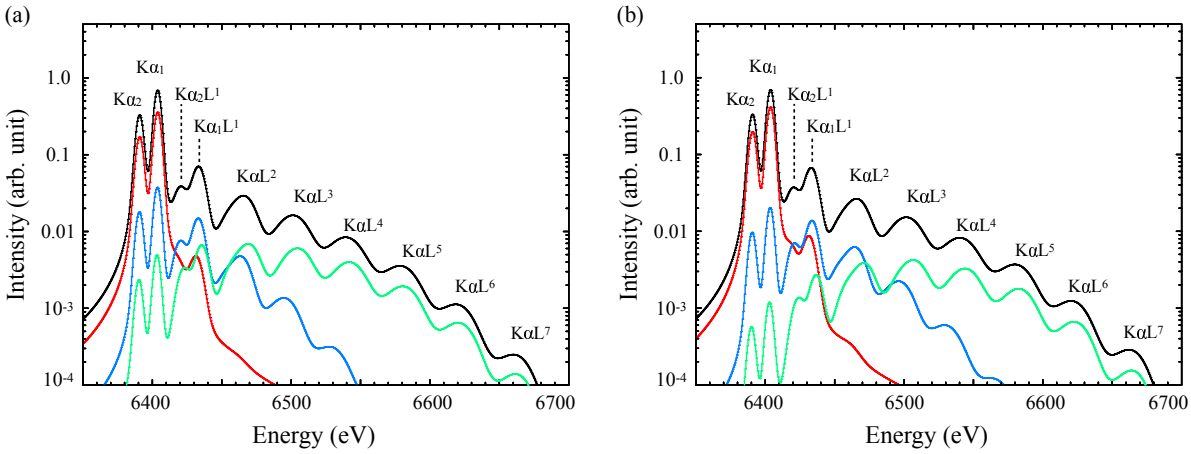

Figure 6.15: Fe Kα structures expected from Fe atoms bombarded by accelerated particles with spectral indices of (a) $s = 1$ and (b) $s = 2$ (black). The red, blue, and green curves represent contributions from protons, O ions, and Fe ions, respectively.

on absorption lines of H_3^+ generated by collisions of the CRs and H_2 molecules in a dense cloud (e.g., Indriolo et al., 2010). We finally note that potential targets would not be limited to SNRs, considering the recent claims of contribution of CR-ionization to the neutral Fe K line in the Arches cluster region (Tatischeff et al., 2012; Krivonos et al., 2017) and in the Galactic ridge (Nobukawa et al., 2015).

Chapter 7

Conclusions

We performed spectroscopic analysis of thermal X-rays from SNRs, W44 and IC 443, aiming to understand the physical origin of RPs, and constructed a model to predict X-ray line emission from dense clouds bombarded by sub-relativistic particles accelerated in SNRs for probing sub-relativistic particles with the future X-ray satellites. The important results are summarized as follows:

1. We have performed spatially resolved spectroscopy of X-ray emission of W44 with *XMM-Newton*. All spectra extracted from each region are well fitted with an RP model. The X-ray absorption column densities well correlate with the distribution of foreground gas in the line-of-sight toward W44 as traced by radio line emissions. The obtained electron temperature kT_e and the recombination timescale $n_e t$ of RPs range from 0.18 keV to 0.60 keV and from 3×10^{11} cm^{-3} s to 9×10^{11} cm^{-3} s, respectively. We have discovered that kT_e is lower in the region where the shock is interacting with molecular clouds and that kT_e and $n_e t$ are negatively correlated. These findings indicate thermal conduction between X-ray emitting and the cold dense gas as the origin of the over-ionization. We have also found that $n_e t$ is especially smaller in the regions with spatially extended moderately broad emissions of the ^{12}CO($J = 1$–0) line, which are considered to be emitted by clumpy gas shocked and disturbed by the SNR shock (Seta et al., 2004; Sashida et al., 2013). This result indicates a rapid cooling of the plasma through evaporation of the clumpy gas.

2. We analyzed *XMM-Newton* data of IC 443 with the same method applied to the W44 case. The spectra extracted from each region of the remnant are all fitted well with a single RP model or a model consisting of RP and CIE components. The obtained electron temperature kT_e and the recombining timescale $n_e t$ in the RP component range from 0.15 keV to 0.65 keV and from 4×10^{11} cm^{-3} s to 14×10^{11} cm^{-3} s, respectively. We found a good spatial correlation between the X-ray absorption column and the distribution of foreground gas traced by ^{12}CO lines, in the line-of-sight toward IC 443. Our analysis revealed that kT_e and $n_e t$ decrease in the region where IC 443 is interacting with dense clouds traced by the ^{12}CO and H_2 observations, and the values show roughly negatively correlated. These results are very similar to those from W44, and suggest thermal conduction between SNR plasma and the clouds is responsible for the RPs in IC 443. Aiming to directly evaluate an ionization degree of RP in each region, we calculated average charges of ions in the RP with obtained kT_e and $n_e t$. We found RPs in the shock-cloud interaction regions tend to have larger ΔC for Ne-Si ions, supporting the thermal conduction scenario.

3. Our analysis of the *XMM-Newton* data of W44 and IC 443 indicate that thermal conduction between SNR plasma and ambient clouds is the most plausible formation process of the over-ionization. On the other hand, Yamaguchi et al. (2018) found clear evidence for adiabatic cooling as the formation process of RPs in W49B. A comparison of results on these SNRs suggests that both thermal conduction and adiabatic cooling are possible channels of over-ionization in SNRs and that the dominant channel may change as SNRs evolve. Recent hydrodynamical simulations by Zhang et al. (2019) support this idea as well. Systematic observational studies as well as their comparison with theoretical and numerical studies are helpful to further clarify the over-ionization process in SNRs and will lead us to comprehensive understanding of the injection mechanism of energy in SNRs into interstellar space. In particular, investigations of charge fractions as demonstrated in the analysis of IC 443 would work as a powerful tool.

4. We constructed a model for the Fe Kα line structures by various projectile ions utilizing atomic-collision data. When energetic heavy ions collide with target atoms, their strong Coulomb field can easily cause simultaneous ejection of multiple electrons of the target. This results in shifts ($\sim$ a few 10 eV) in characteristic X-ray line energies, forming distinctive spectral structures. Detection of such structures in the neutral Fe Kα line strongly supports that the Fe Kα line detected in some SNRs are from the dense clouds bombarded by sub-relativistic particles accelerated in SNRs. An $\sim$ eV energy resolution by X-ray micro-calorimeters onboard *XRISM* and future satellites such as *Athena*, would be necessary to resolve the structures.

5. We found that the line structures strongly depend on the composition of sub-relativistic particles. In particular, as the projectile ion is heavier, the shifts of the line structure become larger. Detection of such structures would allow us to prove the presence of heavy ions in particles accelerated in SNRs and to constrain their composition.

Acknowledgments

First of all, I would like to express my best gratitude to Prof. Takeshi Tsuru, Ass. Prof. Takaaki Tanaka, and Ass. Prof. Hiroyuki Uchida, for guiding me throughout the five years at Kyoto university. Without their advices, this thesis could not reach the present level. I am very grateful to my collaborators, Hiroya Yamaguchi, Masumichi Seta, Randall K. Smith, Satoshi Yoshiike, Salvatore Orlando, Fabrizio Bocchino, Marco Miceli, and Makoto Imai, for their advices and helpful comments. Many insightful comments were given by H. Sano, T. Mukoyama, M. Pajek, B. Sulik, V. Tatischeff, and D. Banas. I appreciate the supports and encouragements of all the people in the Cosmic ray group and *XRISM* team. Finally, I thank my family for their support and understanding.

References

Abdo, A. A., Ackermann, et al. 2010, ApJ, 718, 348

Adelberger, E. G., García, A., Robertson, R. G. H., et al. 2011, Reviews of Modern Physics, 83, 195. doi:10.1103/RevModPhys.83.195

Acero, F., Aharonian, F., Akhperjanian, A. G., et al. 2010, A&A, 516, A62

Ackermann, M., et al. 2013, Science, 339, 807

Aharonian, F. A. & Atoyan, A. M. 1996, A&A, 309, 917

Aharonian, F., et al. 2007, A&A, 464, 235

Aharonian, F., et al. 2008, A&A, 481, 401

Arnaud, K. A. 1996, Astronomical Data Analysis Software and Systems V, 101, 17

Arnett, W. D. 1969, Ap&SS, 5, 180

Barbon, R., Ciatti, F., & Rosino, L. 1973, A&A, 29, 57

Baring, M. G., Jones, F. C., & Ellison, D. C. 2000, ApJ, 528, 776

Barcons, X., et al. 2017, Astronomische Nachrichten, 338, 153

Batič, M., Pia, M. G., & Cipolla, S. J. 2013, Computer Physics Communications, 184, 2232

Bell, A. R. 1978, MNRAS, 182, 147

Bethe, H. A. & Wilson, J. R. 1985, ApJ, 295, 14

Blandford, R. D. & Ostriker, J. P. 1978, ApJ, 221, L29

Blumenthal, G. R. & Gould, R. J. 1970, Reviews of Modern Physics, 42, 237. doi:10.1103/RevModPhys.42.237

Bocchino, F. & Bykov, A. M. 2003, A&A, 400, 203

Bohr, N., 1948, Det Kgl. Danske Videnskabernes Selskab. Math.-fys. Medd. XVIII, No.8.

Borkowski, K. J., Reynolds, S. P., & Roberts, M. S. E. 2016, ApJ, 819, 160

Brandt, W., & Lapicki, G. 1981, Phys. Rev. A, 23, 1717

Burch, D., Richard, P., & Blake, R. L. 1971, Phys. Rev. Lett., 26, 1355

Burginyon, G. A., Hill, R. W., & Seward, F. D. 1975, ApJ, 200, 163. doi:10.1086/153773

Campbell, J. L., & Papp, T. 2001, Atomic Data and Nuclear Data Tables, 77, 1

Cao, Y., Kulkarni, S. R., Howell, D. A., et al. 2015, Nature, 521, 328

Castelletti, G., Dubner, G., Brogan, C., et al. 2007, A&A, 471, 537

Chevalier, R. A. 1974, ApJ, 188, 501

Claussen, M. J., Frail, D. A., Goss, W. M., & Gaume, R. A. 1997, ApJ, 489, 143

Claussen, M. J., Goss, W. M., Frail, D. A., & Desai, K. 1999, ApJ, 522, 349

Colgate, S. A. & White, R. H. 1966, ApJ, 143, 626

Cox, D. P., Shelton, R. L., Maciejewski, W., et al. 1999, ApJ, 524, 179

den Herder, J. W., Brinkman, A. C., Kahn, S. M., et al. 2001, A&A, 365, L7

Denoyer, L. K. 1979, ApJ, 232, L165. doi:10.1086/183057

Dogiel, V., Chernyshov, D., Koyama, K., Nobukawa, M., & Cheng, K.-S. 2011, PASJ, 63, 535

Doggett, J. B., & Branch, D. 1985, AJ, 90, 2303

Dubner, G. M., Velázquez, P. F., Goss, W. M., et al. 2000, AJ, 120, 1933. doi:10.1086/301583

Engelmann, J. J., Ferrando, P., Soutoul, A., et al. 1990, A&A, 233, 96

Elias, J. H., Matthews, K., Neugebauer, G., et al. 1985, ApJ, 296, 379

Filippenko, A. V. 1997, ARA&A, 35, 309. doi:10.1146/annurev.astro.35.1.309

Fermi, E. 1949, Physical Review, 75, 1169

Foster, A. R., Smith, R. K., & Brickhouse, N. S. 2017, Atomic Processes in Plasmas (apip 2016), 190005.

Frail, D. A., & Mitchell, G. F. 1998, ApJ, 508, 690

Gaensler, B. M., Chatterjee, S., Slane, P. O., et al. 2006, ApJ, 648, 1037. doi:10.1086/506246

George, J. S., Lave, K. A., Wiedenbeck, M. E., et al. 2009, ApJ, 698, 1666. doi:10.1088/0004-637X/698/2/1666

Giacconi, R., Gursky, H., Paolini, F. R., et al. 1962, Phys. Rev. Lett., 9, 439. doi:10.1103/PhysRevLett.9.439

Ginzburg, V. L. & Syrovatskii, S. I. 1964, The Origin of Cosmic Rays, New York: Macmillan, 1964

Gorenstein, P., Kellogg, E. M., & Gursky, H. 1970, ApJ, 160, 199. doi:10.1086/150417

Greco, E., Miceli, M., Orlando, S., et al. 2018, A&A, 615, A157

Green, D. A. 1986, MNRAS, 218, 533. doi:10.1093/mnras/218.3.533

Green, D. A. 2019, Journal of Astrophysics and Astronomy, 40, 36

Hamuy, M., Phillips, M. M., Suntzeff, N. B., et al. 2003, Nature, 424, 651

Harrus, I. M., Hughes, J. P., Singh, K. P., Koyama, K., & Asaoka, I. 1997, ApJ, 488, 781

H. E. S. S. Collaboration, Abdalla, H., Abramowski, A., et al. 2018, A&A, 612, A1. doi:10.1051/0004-6361/201732098

Hitomi Collaboration, Aharonian, F., Akamatsu, H., et al. 2016, Nature, 535, 117. doi:10.1038/nature18627

Hitomi Collaboration, Aharonian, F., Akamatsu, H., et al. 2017, Nature, 551, 478. doi:10.1038/nature24301

Hirayama, A., Yamauchi, S., Nobukawa, K. K., et al. 2019, PASJ, 71, 37. doi:10.1093/pasj/psy153

Hayashida, K., Tomida, H., Mori, K., et al. 2018, Proc. SPIE, 10699, 1069923. doi:10.1117/12.2311446

Horvat, V., Watson, R. L., & Peng, Y. 2006, Phys. Rev. A, 74, 022718

Horvat, V., Watson, R. L., & Peng, Y. 2009, Phys. Rev. A, 79, 012708

Hoyle, F., & Fowler, W. A. 1960, ApJ, 132, 565

Indriolo, N., et al. 2010, ApJ, 724, 1357

Ishisaki, Y., et al. 2018, Journal of Low Temperature Physics, 193, 991

Itoh, H., & Masai, K. 1989, MNRAS, 236, 885

Iwamoto, K., Brachwitz, F., Nomoto, K., et al. 1999, ApJS, 125, 439. doi:10.1086/313278

Jones, F. C. 1968, Physical Review, 167, 1159. doi:10.1103/PhysRev.167.1159

Jones, L. R., Smith, A., & Angelini, L. 1993, MNRAS, 265, 631

Kafexhiu, E., Aharonian, F., Taylor, A. M., et al. 2014, Phys. Rev. D, 90, 123014. doi:10.1103/PhysRevD.90.123014

Kanemaru, Y., Sato, J., Takaki, T., et al. 2020, Nuclear Instruments and Methods in Physics Research A, 984, 164646. doi:10.1016/j.nima.2020.164646

Katsuda, S., Mori, K., Maeda, K., et al. 2015, ApJ, 808, 49

Katsuragawa, M., Nakashima, S., Matsumura, H., et al. 2018, PASJ, 70, 110.

Kauffman, R. L., McGuire, J. H., Richard, P., Moore, C. F. 1973, Phys. Rev. A, 8, 1233

Kavčič, M., et al. 2000, Phys. Rev. A, 61, 052711

Kawasaki, M. T., Ozaki, M., Nagase, F., et al. 2002, ApJ, 572, 897

Kawasaki, M., Ozaki, M., Nagase, F., Inoue, H., & Petre, R. 2005, ApJ, 631, 935

Krivonos, R., et al. 2017, MNRAS, 468, 2822

Kokusho, T., Torii, H., Nagayama, T., et al. 2020, ApJ, 899, 49

Koyama, K., Petre, R., Gotthelf, E. V., Hwang, U., Matsuura, M., Ozaki, M., & Holt, S. S. 1995, Nature, 378, 255

Koyama, K., Kinugasa, K., Matsuzaki, K., et al. 1997, PASJ, 49, L7

Krause, M. O. 1979, Journal of Physical and Chemical Reference Data, 8, 307

Kuntz, K. D., & Snowden, S. L. 2008, A&A, 478, 575

Kushino, A., Ishisaki, Y., Morita, U., et al. 2002, PASJ, 54, 327

Landau, L. D. & Lifshitz, E. M. 1959, Course of theoretical physics, Oxford: Pergamon Press, 1959

Lazendic, J. S. & Slane, P. O. 2006, ApJ, 647, 350

Leahy, D. A., & Tian, W. W. 2007, A&A, 461, 1013

Lee, J.-J., Koo, B.-C., Yun, M. S., et al. 2008, AJ, 135, 796

Lee, J.-J., Koo, B.-C., Snell, R. L., et al. 2012, ApJ, 749, 34

Leonard, D. C. 2007, ApJ, 670, 1275

Li, W., Bloom, J. S., Podsiadlowski, P., et al. 2011, Nature, 480, 348

Lopez, L. A., Pearson, S., Ramirez-Ruiz, E., et al. 2013, ApJ, 777, 145

Lumb, D. H., Warwick, R. S., Page, M., & De Luca, A. 2002, A&A, 389, 93

McKee, C. F. 1974, ApJ, 188, 335. doi:10.1086/152721

Meidinger, N., Dennerl, K., Hartner, G. D., et al. 2004, Mem. Soc. Astron. Italiana, 75, 551

Mewaldt, R. A. 1994, Advances in Space Research, 14, 737. doi:10.1016/0273-1177(94)90536-3

Meyer, J.-P., Drury, L. O., & Ellison, D. C. 1997, ApJ, 487, 182. doi:10.1086/304599

Nobukawa, K. K., et al. 2015, ApJ, 807, L10

Nobukawa, K. K., et al. 2018, ApJ, 854, 87

Nobukawa, K. K., Hirayama, A., Shimaguchi, A., Fujita, Y., Nobukawa, M., & Yamauchi, S. 2019, PASJ, 71, 115

Nomoto, K., Sugimoto, D., & Neo, S. 1976, Ap&SS, 39, L37

Nomoto, K., Thielemann, F.-K., & Yokoi, K. 1984, ApJ, 286, 644

Makino, K., Fujita, Y., Nobukawa, K. K., Matsumoto, H., & Ohira, Y. 2019, PASJ, 71, 78

Marion, G. H., Brown, P. J., Vinkó, J., et al. 2016, ApJ, 820, 92

Masai, K. 1984, Ap&SS, 98, 367

Masai, K. 1994, ApJ, 437, 770

Mason, K. O., Breeveld, A., Much, R., et al. 2001, A&A, 365, L36

Masui, K., Mitsuda, K., Yamasaki, N. Y., et al. 2009, PASJ, 61, S115

Matsumura, H., Uchida, H., Tanaka, T., et al. 2017, PASJ, 69, 30

Matsumura, H., Tanaka, T., Uchida, H., Okon, H., & Tsuru, T. G. 2017, ApJ, 851, 73

Matsumura, H. 2018, PhD thesis, Kyoto Univ.

McGuire, J. H., & Richard, P. 1973, Phys. Rev. A, 8, 1374

Mewaldt, R. A. 1994, Advances in Space Research, 14, 737

Miceli, M., Decourchelle, A., Ballet, J., et al. 2006, A&A, 453, 567. doi:10.1051/0004-6361:20054290

Miceli, M., Bocchino, F., Decourchelle, A., et al. 2010, A&A, 514, L2

Miceli, M., Orlando, S., Burrows, D. N., et al. 2019, Nature Astronomy, 3, 236. doi:10.1038/s41550-018-0677-8

Minkowski, R. 1941, PASP, 53, 224

Moffett, D. A. & Reynolds, S. P. 1994, ApJ, 437, 705. doi:10.1086/175033

Nobukawa, K. K., Nobukawa, M., Koyama, K., et al. 2018, ApJ, 854, 87

Ohashi, T., et al. 2018, SPIE Proc., 10699, 1069928

Ohnishi, T., Uchida, H., Tsuru, T. G., et al. 2014, ApJ, 784, 74. doi:10.1088/0004-637X/784/1/74

Okon, H., Uchida, H., Tanaka, T., Matsumura, H., & Tsuru, T. G. 2018, PASJ, 70, 35

Okon, H., Tanaka, T., Uchida, H., et al. 2020, ApJ, 890, 62. doi:10.3847/1538-4357/ab6987

Olbert, C. M., Clearfield, C. R., Williams, N. E., et al. 2001, ApJ, 554, L205. doi:10.1086/321708

Orlando, S., Peres, G., Reale, F., et al. 2005, A&A, 444, 505

Orlando, S., Bocchino, F., Reale, F., Peres, G., & Pagano, P. 2008, ApJ, 678, 274

Ozawa, M., Koyama, K., Yamaguchi, H., Masai, K., & Tamagawa, T. 2009, ApJ, 706, L71

Petre, R., Szymkowiak, A. E., Seward, F. D., et al. 1988, ApJ, 335, 215. doi:10.1086/166922

Petre, R., Kuntz, K. D., & Shelton, R. L. 2002, ApJ, 579, 404

Pye, J. P., Becker, R. H., Seward, F. D., & Thomas, N. 1984, MNRAS, 207, 649

Ramaty, R., Kozlovsky, B., & Lingenfelter, R. E. 1979, ApJS, 40, 487. doi:10.1086/190596

Ranasinghe, S., & Leahy, D. A. 2018, AJ, 155, 204

Rho, J., Petre, R., Schlegel, E. M., et al. 1994, ApJ, 430, 757. doi:10.1086/174446

Rho, J., & Petre, R. 1998, ApJ, 503, L167

Rho, J., Jarrett, T. H., Cutri, R. M., et al. 2001, ApJ, 547, 885. doi:10.1086/318398

Rho, J. & Borkowski, K. J. 2002, ApJ, 575, 201. doi:10.1086/341192

Rybicki, G. B. & Lightman, A. P. 1979, A Wiley-Interscience Publication, New York: Wiley, 1979

Rymuza, P., Sujkowski, Z., Carlen, M., Dousse, J.-C., Gasser, M., Kern, J., Perny, B., & Rhéme, C. 1989, Zeitschrift fur Physik D Atoms Molecules Clusters, 14, 37

Saji, S., Matsumoto, H., Nobukawa, M., Nobukawa, K. K., Uchiyama, H., Yamauchi, S., & Koyama, K. 2018, PASJ, 70, 23

Sanders, J. S. 2006, MNRAS, 371, 829

Sashida, T., Oka, T., Tanaka, K., et al. 2013, ApJ, 774, 10

Schönfelder, V., Bennett, K., Blom, J. J., et al. 2000, A&AS, 143, 145. doi:10.1051/aas:2000101

Sedov, L. I. 1959, Similarity and Dimensional Methods in Mechanics

Seta, M., Hasegawa, T., Dame, T. M., et al. 1998, ApJ, 505, 286

Seta, M., Hasegawa, T., Sakamoto, S., et al. 2004, AJ, 127, 1098

Sezer, A., Ergin, T., Yamazaki, R., et al. 2019, arXiv e-prints, arXiv:1907.01017

Shelton, R. L., Kuntz, K. D., & Petre, R. 2004, ApJ, 611, 906

Shimizu, T., Masai, K., & Koyama, K. 2012, PASJ, 64, 24

Slane, P., Hughes, J. P., Edgar, R. J., et al. 2001, ApJ, 548, 814

Smith, A., Jones, L. R., Peacock, A., & Pye, J. P. 1985, ApJ, 296, 469

Smith, A., Jones, L. R., Watson, M. G., et al. 1985, MNRAS, 217, 99

Smith, R. K. & Hughes, J. P. 2010, ApJ, 718, 583

Smith, R. K., Odaka, H., Audard, M., et al. 2014, arXiv:1412.1172

Stecker, F. W. 1971, Baltimore: Mono Book Corp., 1971

Strüder, L., Briel, U., Dennerl, K., et al. 2001, A&A, 365, L18

Sulik, B., Kádár, I., Ricz, S., Varga, D., Végh, J., Hock, G., & Berényi, D. 1987, Nuclear Instruments and Methods in Physics Research B, 28, 509

Sutherland, R. S. & Dopita, M. A. 1993, ApJS, 88, 253

Takei, Y., Yasuda, S., Ishimura, K., et al. 2018, Journal of Astronomical Telescopes, Instruments, and Systems, 4, 011216. doi:10.1117/1.JATIS.4.1.011216

Tanaka, T., et al. 2018, ApJ, 866, L26

Tashiro, M., et al. 2018, SPIE Proc., 10699, 1069922

Tatischeff, V., Decourchelle, A., & Maurin, G. 2012, A&A, 546, A88

Thielemann, F.-K., Nomoto, K., & Hashimoto, M.-A. 1996, ApJ, 460, 408. doi:10.1086/176980

Troja, E., Bocchino, F., Miceli, M., et al. 2008, A&A, 485, 777. doi:10.1051/0004-6361:20079123

Tsunemi, H., Yamashita, K., Masai, K., et al. 1986, ApJ, 306, 248. doi:10.1086/164337

Tsuji, N. & Uchiyama, Y. 2016, PASJ, 68, 108. doi:10.1093/pasj/psw102

Turatto, M. 2003, Supernovae and Gamma-ray Bursters, 21

Turner, M. J. L., Abbey, A., Arnaud, M., et al. 2001, A&A, 365, L27

Uchida, H., Koyama, K., Yamaguchi, H., et al. 2012, PASJ, 64, 141

Uchida, H., Koyama, K., & Yamaguchi, H. 2015, ApJ, 808, 77

Uchida, H., Tanaka, T., Amano, Y., et al. 2020, Nuclear Instruments and Methods in Physics Research A, 978, 164374. doi:10.1016/j.nima.2020.164374

Uchiyama, Y., Aharonian, F. A., Tanaka, T., et al. 2007, Nature, 449, 576. doi:10.1038/nature06210

Uchiyama, H., Nobukawa, M., Tsuru, T. G., & Koyama, K. 2013, PASJ, 65, 19

Umemoto, T., Minamidani, T., Kuno, N., et al. 2017, PASJ, 69, 78

Ustamujic, S., Orlando, S., Greco, E., et al. 2020, arXiv:2012.08017

van den Bergh, S., & Tammann, G. A. 1991, ARA&A, 29, 363

Wang, X.-L., Dong, C.-Z., & Su, M.-G. 2012, Nuclear Instruments and Methods in Physics Research B, 280, 93

Webbink, R. F. 1984, ApJ, 277, 355

Welsh, B. Y. & Sallmen, S. 2003, A&A, 408, 545

Wheeler, J. C., Piran, T., & Weinberg, S. 1990, Supernovae, Jerusalem Winter School for Theoretical Physics, 6

Whelan, J., & Iben, I. 1973, ApJ, 186, 1007

White, R. L. & Long, K. S. 1991, ApJ, 373, 543

Wilms, J., Allen, A., & McCray, R. 2000, ApJ, 542, 914

Wolszczan, A., Cordes, J. M., & Dewey, R. J. 1991, ApJ, 372, L99

Xu, J.-L., Wang, J.-J., & Miller, M. 2011, ApJ, 727, 81

Yamaguchi, H., Ozawa, M., Koyama, K., et al. 2009, ApJ, 705, L6

Yamaguchi, H., Eriksen, K. A., Badenes, C., et al. 2014, ApJ, 780, 136

Yamaguchi, H., Badenes, C., Foster, A. R., et al. 2015, ApJ, 801, L31

Yamaguchi, H., Tanaka, T., Wik, D. R., et al. 2018, ApJ, 868, L35

Yamauchi, S., Nobukawa, K. K., Nobukawa, M., Uchiyama, H., & Koyama, K. 2016, PASJ, 68, 59

Yoshiike, S., Fukuda, T., Sano, H., et al. 2013, ApJ, 768, 179

Yoshiike, S. 2017, AJ, PhD thesis, Nagoya Univ.
<https://nagoya.repo.nii.ac.jp/?action=pages_view_main&active_action=repository_view_main_item_detail&item_id=23792&item_no=1&page_id=28&block_id=27>

Zhang, G.-Y., Slavin, J. D., Foster, A., et al. 2019, ApJ, 875, 2

Zhou, X., Miceli, M., Bocchino, F., Orlando, S., & Chen, Y. 2011, MNRAS, 415, 244